JOHANNES KEPLER
UNIVERSITY LINZ

Submitted by
Franziska Maria Maier

Submitted at
Institut für Angewandte Physik

First Supervisor
Univ. Prof. Dr. Thomas Klar

Second Supervisor
Univ. Prof. Dr. Lutz Schweikhard

Co-Supervisor
Dr. Stephan Malbrunot-Ettenauer

March 2019

Laser Spectroscopy of Short-Lived-Radionuclides in an Ion Trap:
MIRACLS' proof-of-principle experiment and the simulation of the future 30-keV MR-ToF device

Master Thesis
to obtain the academic degree of
Diplom-Ingenieurin
in the Master's Program
Technische Physik

CERN-THESIS-2019-450
//2019

JOHANNES KEPLER UNIVERSITY LINZ
Altenbergerstraße 69
4040 Linz, Österreich
www.jku.at
DVR 0093696

Eidesstattliche Erklärung

Ich erkläre an Eides statt, dass ich die vorliegende Masterarbeit selbstständig und ohne fremde Hilfe verfasst, andere als die angegebenen Quellen und Hilfsmittel nicht benutzt bzw. die wörtlich oder sinngemäß entnommenen Stellen als solche kenntlich gemacht habe. Die vorliegende Masterarbeit ist mit dem elektronisch übermittelten Textdokument identisch.

Franziska Maria Maier

Acknowledgement

First of all, I would like to thank my supervisor Stephan Malbrunot-Ettenauer for offering me the possibility to work at MIRACLS and for his constant support during that time. Thanks, that you always had time for explaining and showing new things to me. I was able to learn a lot of new things during my stay at ISOLDE. Secondly, I want to say a big thank you to the whole team of MIRACLS for their support, the interesting and inspiring discussions as well as for their help in getting along in a foreign country. Special thanks to Simon Lechner, for helping me with all the laser related things, Varvara Lagaki for ordering the equipment I needed, talking to the technicians and making most of the mechanical drawings for the proof-of-principle experiment, Frank Wienholtz for not only handing his simulation files for ISOLTRAP over to me but also for answering my questions concerning SimIon and Simon Sels and Peter Plattner for showing me how to write time efficient Python files. Moreover, I would like to thank Prof. Lutz Schweikhard and Prof. Thomas Klar for making it possible that I could go to CERN for writing my master thesis there. Finally I would like to thank my parents for all their support during my studies.

Abstract

For nearly four decades Collinear Laser Spectroscopy (CLS) has been employed to determine ground-state properties of short-lived radionuclides. To extend its reach to the most exotic radionuclides with very low production yields at radioactive ion beam facilities, the novel Multi Ion Reflection Apparatus for CLS (MIRACLS) is currently under development at ISOLDE/CERN. In this setup, 30-keV ion bunches will be trapped between two electrostatic mirrors of a multi-reflection time-of-flight (MR-ToF) device such that the laser beam will probe the ions during each revolution. Thus, the observation time will be extended and the experimental sensitivity will be increased significantly while maintaining the high resolution of conventional CLS. A proof-of-principle experiment is performed to demonstrate the potential of CLS within an existing, low-energy MR-ToF device. Its first experimental results benchmark the validity of ion-optical simulations in the MR-ToF device, that are applied to the future 30-keV MIRACLS' apparatus. The proof-of-principle setup, its successful realisation of CLS in a MR-ToF device as well as the simulation of a 30-keV MR-ToF apparatus will be presented in the following.

Zusammenfassung

Seit fast vier Jahrzehnten werden Grundzustandseigenschaften von kurzlebigen radioaktiven Nukliden erfolgreich mit der Technik der Kollinearen Laserspektroskopie (CLS) bestimmt. Zur Messung von sehr exotischen Radionukliden, die nur in geringen Mengen in modernen Kernforschungsanlagen erzeugt werden können, sind neue innovative Versuchsaufbauten erforderlich, wie z.B. der Multi Ion Reflection Apparatus for CLS (MIRACLS), der zurzeit an der ISOLDE am CERN entwickelt wird. Ionen mit einer kinetischen Energie von 30 keV sollen zwischen zwei elektrostatischen Spiegeln eines Multi-Reflection Time-of-Flight (MR-ToF) Geräts eingefangen werden, sodass der Laserstrahl die Ionen bei jeder Umdrehung anregen kann. Dadurch wird die Beobachtungszeit verlängert und somit die experimentelle Sensitivität signifikant erhöht, während die hohe Auflösung von konventioneller CLS erhalten bleibt. Ein Pilotexperiment wurde aufgebaut, um zu zeigen, dass CLS in einem bereits existierenden, niederenergetischen MR-ToF Gerät grundsätzlich möglich ist. Die experimentellen Ergebnisse sind in guter Übereinstimmung mit Ionen-optischen Simulationen, die in weiterer Folge auf das 30-keV MR-ToF Gerät angewandt werden. In dieser Arbeit wird der Aufbau des Pilotexperiments, dessen experimentelle Ergebnisse, sowie Ionen-optische Simulationen des 30-keV MR-ToF Geräts beschrieben.

Contents

Abbreviations and Acronyms

CERN European Organization for Nuclear Research

CDT central drift tube

CLS Collinear Laser Spectroscopy

COLLAPS Collinear Laser Spectroscopy beam line at ISOLDE

CRIS Collinear Resonance Ionization Spectroscopy experiment at ISOLDE/CERN

cw continuous-wave

FWHM full width at half maximum

GPS General Purpose Separator at ISOLDE/CERN

HFS Hyperfine Structure

HRS High Resolution Separator at ISOLDE/CERN

HV High Voltage

ISCOOL Cooler and Buncher at ISOLDE/CERN

ISOLDE On-Line Isotope Mass Separator dedicated to produce many different radioactive ion beams at CERN

ISOLTRAP a Penning trap and a MR-ToF mass spectrometer for high-precision mass measurements at ISOLDE/CERN

laser device used for light amplification by stimulated emission of radiation

MCP multi-channel-plate

MIRACLS Multi Ion Reflection Apparatus for Collinear Laser Spectroscopy at ISOLDE/CERN

MR-ToF Multi-Reflection Time-of-Flight

ODR optical detection region

PMT photomultiplier tube

QPB quadrupole bender

RFQ Radio Frequency Quadrupole

RILIS Resonance Ionization Laser Ion Source at ISOLDE/CERN

UHV Ultra High Vacuum

Chapter 1

Introduction

Just a little bit more than a century ago Ernest Rutherford discovered the atomic nucleus by observing a deflection of most of the alpha particles when bombarding a gold foil with alpha particles emitted from the radioactive Radium. From this observation, he concluded that an atom consists of a tiny, dense and positively charged nucleus that is surrounded by the lighter, negatively charged electrons. Since then physicists all around the world have tried to understand the structure of the nucleus, that is now known to consist of protons and neutrons that are bound together via the strong force. In 1963 Maria Goeppert Mayer and J. Hans O. Jensen received the Nobel prize for their work concerning the nuclear shell structure. Similar to the electrons in an atom, protons and neutrons (i.e. the nucleons) in an atomic nuclei occupy quantum levels that are separated by energy gaps [74]. When adding nucleons to a nucleus, there exist certain proton and neutron numbers where the binding energy with the added nucleon is significantly less than the one without this nucleon. Moreover, normally the radii of nuclei increase with raising proton and neutron number. However, isotope chains show a decrease in the nuclear charge radius towards a neutron shell closure. This illustrates the fact, that nuclides with completely filled shells are more bound. The number of nucleons (either protons or neutrons separately) that completely fill each shell define the magic numbers that are 2, 8, 20, 28, 50, 82, and 126.

Modern radioactive ion beam facilities have opened a path for the investigation of short-lived, exotic nuclides. Surprisingly, far from stability established shell closures at the magic numbers are disappearing and new (sub)shell closures are emerging at unexpected proton or neutron numbers (see e.g. [41, 83]). It is the goal of modern nuclear physics to explain those discontinuities, to pin down the exact mechanism of this so-called shell evolution, and to predict new shell closures. With the help of radioactive ion beam facilities, such as ISOLDE at CERN, more and more exotic nuclides can be produced and their properties can be studied at dedicated experimental setups such as COLLAPS, the Collinear Laser Spectroscopy (CLS) beam line at ISOLDE.
Due to its high accuracy and resolution, CLS is a powerful experimental technique to access nuclear ground-state properties such as nuclear spins, electromagnetic moments, and mean-square charge radii of short-lived radionuclides [11, 14, 60]. For CLS, a narrow-band laser beam is overlapped with a singly- or doubly-charged ion or neutralized atom beam. When the wavelength of the laser matches the energy difference of the selected electronic transition, ions or atoms are excited. Fluorescence photons emitted by the excited ions or atoms can be detected in an optical detection region (ODR) by photomultiplier tubes (PMTs). By counting the number of photons as a function of the scanned laser frequency, the hyperfine structure HFS of the optical transition is obtained. For high-resolution CLS, fast ion beams with a kinetic energy E of tens of kiloelectronvolts are employed to minimize the Doppler broadening σ_f according to $\sigma_f \propto \sigma_E/\sqrt{E}$ [42], where σ_E is the energy spread of the ions. CLS provides model-independent information on nuclear ground-state properties. It is therefore an important experimental tool to benchmark modern nuclear theory and provides insight into nuclear structure phenomena.
However, to experimentally probe the most exotic nuclides, which can only be produced with low production yields at today's radioactive ion beam facilities, new laser spectroscopy techniques have

to be envisioned to increase the sensitivity of conventional CLS. In traditional CLS, the radioactive ions only interact with the laser beam in the time scale of some microseconds when passing the ODR, whereas the half-life of the studied radionuclides is between tens of milliseconds to seconds and longer. To take advantage of the rare isotopes over their entire lifetime, the concept of a Multi Ion Reflection Apparatus for CLS of radionuclides (MIRACLS) was introduced at CERN. At MIRACLS, a bunched ion beam is trapped between two electrostatic mirrors of an electrostatic ion beam trap [2, 7, 45, 96] or also often called Multi-Reflection Time-of-Flight (MR-ToF) device [65, 66, 77, 88, 90, 93]. Hence, the laser interacts with the ion bunch during each revolution. Therefore the observation time is extended and the experimental sensitivity will be increased by a factor of 40-700 (see chapter 3.4.2) compared to traditional CLS while maintaining its high resolution.

In the realm of rare-isotope science, MR-ToF instruments have recently gained remarkable attention, in particular for precision mass spectrometry or mass separation of short lived nuclides [65, 66, 77, 88, 90]. For high mass resolving powers, MR-ToF devices are operated with a focus in the time domain resulting in an increased energy spread of a few tens of electronvolt for kinetic beam energies E of typically a few kiloelectronvolts [91]. However, for performing high-resolution CLS, E is $\geq 30\,\mathrm{keV}$ and the energy spread should be below 1 eV in order to minimize the Doppler broadening to obtain a spectral resolution which approaches the natural linewidth of the optical transitions. Moreover, CLS relies on a large ion-laser overlap with parallel ion and laser beam axes. Whereas in conventional CLS with a single ion passage through the ODR this can be readily achieved, an ion's trajectory in a MR-ToF device may vary from one revolution to the next (see chapter 4.4). Hence, MR-ToF operation modes have to be identified, which best fulfil the stringent CLS requirements to avoid broadening or distortions in the spectral line shape. For this reason, simulations of the ion trajectories in the envisioned 30-keV MR-ToF apparatus are performed to investigate whether the requirements of CLS in a MR-ToF device can indeed be met. In order to validate these simulations and to demonstrate the functionality of the novel MIRACLS' approach a proof-of-principle (PoP) experiment is currently carried out with a low-energy MR-ToF device [44, 71, 72], which has been modified for the purpose of CLS. Although the spectral resolution of CLS in the PoP experiment is due to the reduced beam energy of about 1.5 keV about 4.5 times lower than the one of 30-keV CLS, the comparison of the experimental data with the simulations help to understand the observed line shapes under varying MR-ToF operation modes and will thus guide the design of MIRACLS' future MR-ToF apparatus. Moreover, experimental results of the PoP experiment benchmark the validity of the simulation approach and provide confidence in its application to the 30-keV MR-ToF device. In the present work, the MIRACLS' PoP experiment and its simulation from the CLS perspective is introduced and the first design of the 30-keV MR-ToF device will be shown.

Chapter 2 provides an overview over the technique of CLS and the nuclear ground state properties that are accessible from the observed hyperfine structure. Chapter 3 introduces the central concepts and experimental techniques such as emittance of an ion beam, Paul traps and electrostatic ion beam traps which subsequent chapters are based on. A more detailed overview over the concept of MIRACLS will be given, especially in terms of the improvement factor in sensitivity of MIRACLS in comparison with traditional CLS techniques. Chapter 4 describes the PoP setup, shows the first experimental results for CLS in a MR-ToF device and compares those results with the simulations. In chapter 5 the 30-keV MR-ToF device is presented together with simulations of its ion trajectories.

Chapter 2

Collinear Laser Spectroscopy (CLS) of Short-Lived Radionuclides

2.1 Fine- and Hyperfine Structure

A fine structure splitting of the atomic energy level arises, when the total orbital momentum $\mathbf{L}$ and the spin angular momentum $\mathbf{S}$ of all the electrons moving in the Coulomb field of a point-like nucleus couple to a new angular momentum $\mathbf{J} = \mathbf{S} + \mathbf{L}$ (spin-orbit coupling).
Taking the internal structure of the nucleus into account an additional splitting (hyperfine splitting) of the fine structure levels arises due to the electromagnetic interaction between the atomic nucleus and the surrounding electron cloud [29]. The electrons induce an electromagnetic field at the position of the nucleus that interacts with the electromagnetic nuclear moments and the nuclear spin.

The nuclear spin $\mathbf{I}$ is the sum of all orbital and spin angular momenta of the nucleons. It is associated with the nuclear magnetic dipole moment

$$\boldsymbol{\mu}_I = \frac{g_I \mu_N \mathbf{I}}{\hbar}, \tag{2.1}$$

where $\hbar$ is the Planck constant, g_I the nuclear g-factor, and μ_N is the nuclear magnetron given by

$$\mu_N = \frac{e\hbar}{2m_p} = \frac{m_e}{m_p}\mu_B. \tag{2.2}$$

Here, e is the elementary charge, m_e and m_p the electron and proton mass, respectively, and μ_B is the Bohr magnetron. The electron cloud induces a magnetic field $\mathbf{B}_J$ at the place of the nucleus which interacts with the nuclear magnetic dipole moment $\boldsymbol{\mu}_I$. A coupling of the angular momenta of the electrons $\mathbf{J}$ and of the nucleus $\mathbf{I}$ to a new angular momentum $\mathbf{F} = \mathbf{J} + \mathbf{I}$ is the result and a splitting of the fine structure levels into hyperfine levels occurs.

The electric quadrupole moment in Cartesian coordinates is defined as

$$Q = \sum_i^A e_i(3z_i^2 - x_i^2 - y_i^2 - z_i^2), \tag{2.3}$$

where e_i are effective charges taking into account core-polarization effects [61] and i runs over all the nucleons building up the respective nucleus with mass number A. The electric quadrupole moment gives insight into the (non-)sphericity of the nuclear charge distribution. If the nucleus exhibits an electric quadrupole moment the energy of the hyperfine levels are additionally shifted because the electrons induce an electric field at the place of the nucleus that interacts with the electric quadrupole moment [11].

Combining both effects, a fine structure level is shifted by the additional energy ΔE_{HFS} due to the hyperfine splitting [14]

$$\Delta E_{\mathrm{HFS}} = \Delta E_{\text{magnetic dipole}} + \Delta E_{\text{electric quadrupole}} + ..., \tag{2.4}$$

where $\Delta E_{\text{magnetic dipole}}$ is the energy splitting due to the interaction of the electrons with the nuclide's magnetic dipole moment and $\Delta E_{\text{electric quadrupole}}$ is the energy splitting due to the interaction of the electrons with the nuclide's electric quadrupole moment. The contribution of higher order electromagnetic moments to the hyperfine structure HFS is very small and is therefore often neglected. The magnetic dipole interaction leads to an energy shift of the atomic levels of [11]

$$\Delta E_{\text{magnetic dipole}} = \frac{A_J}{2}\left[(F(F+1) - I(I+1) - J(J+1)\right], \tag{2.5}$$

where F, I, J are the quantum numbers of the appropriate operators $\mathbf{F}, \mathbf{I}, \mathbf{J}$ and $A_J = \frac{\mu_I B_J}{\hbar I J}$ is the hyperfine coupling constant. The hyperfine states are labelled with the quantum number F of the combined angular momentum $\mathbf{F}$. According to angular momentum couple rules F can take the values $J+I, J+I-1, ..., |J-I|$.

The (hyper)fine structure of an atom can be studied via laser spectroscopy [60]. Therefore, an atom or ion is optically excited from a lower level $|IJF\rangle$ to an upper level $|IJ'F'\rangle$ when absorbing a laser photon of appropriate wavelength. When the excited atoms or ions decay fluorescence photons are spontaneously emitted that can be detected. By counting the number of photons as a function of the scanned laser frequency the HFS of the selected optical transition is obtained. According to the dipole selection rules only specific transitions between the hyperfine states are allowed. For an allowed transition the difference of the quantum numbers F and F' has to be 0 or ± 1, but the transition from $F = 0$ to $F' = 0$ is forbidden.

In the following the HFS structure of $^{24-26}Mg^+$ ions is explained, since these ion species will be used as test cases in MIRACLS' proof-of-principle experiment. The ionic structure of the lowest fine structure levels in Mg^+ ions can be seen in figure 2.1. The transition from the ionic ground state $3s\ ^2S_{1/2}$ to the excited fine structure state $3p\ ^2P_{1/2}$ with the angular momentum $J = 1/2$ is called D1 line and the transition to the excited fine structure state $3p^2P_{3/2}$ with the angular momentum $J = 3/2$ is called D2 line [6]. Ground and excited state can split up according to the hyperfine splitting. For $^{25}Mg^+$ the nuclear spin is $I = 5/2$ and ground and excited state show a hyperfine splitting that can be seen in figure 2.2 for the D1 and the D2 line together with the corresponding hyperfine spectra.
For $^{24}Mg^+$ and for $^{26}Mg^+$ the nuclear spin I is 0 and therefore no hyperfine splitting arises. The spectra for $^{24}Mg^+$ and for $^{26}Mg^+$ just consist of one peak at the resonance wavelength of the D1 or D2 line around 280 nm. Hence, both the D1 and D2 transitions in the even-even $^{24,26}Mg$ isotopes form a closed two level system, in which laser-excited ions decay back to the ionic ground state such that they can in principle be probed indefinitely by the laser beam. Hence, without pumping to other HFS states, these isotopes are ideal test cases for CLS in a MR-ToF device.

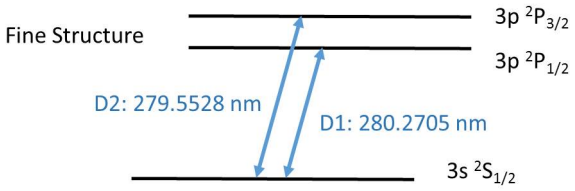

Figure 2.1: Lowest lying fine structure states in Mg^+. The D1 and D2 transition frequencies are taken from [70].

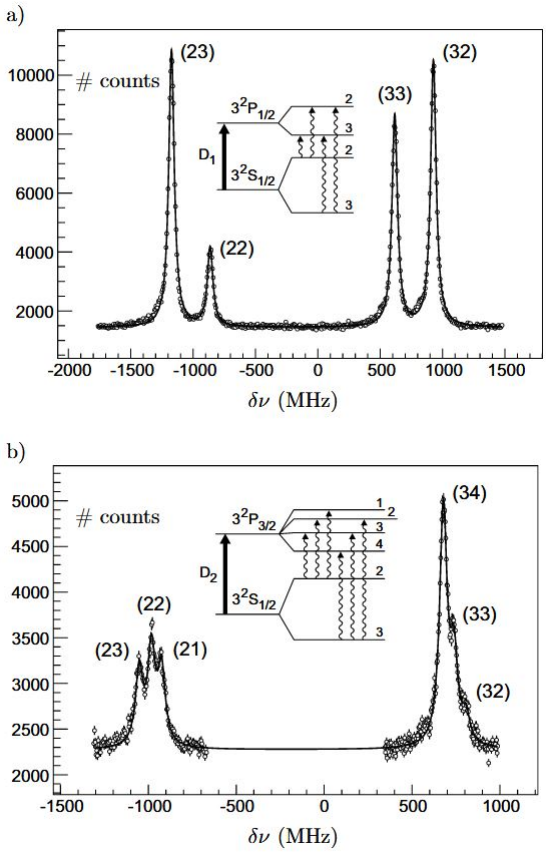

Figure 2.2: Hyperfine spectra of $^{25}Mg^+$ ($I = 5/2$) in the D1 and D2 lines (a) and (b), respectively. The fitted curves consist of Lorentzian profiles (see chapter 2.4). The inserts show the splitting of the energy states, where the allowed transitions from the lower hyperfine level F to the upper hyperfine level F' (FF') are marked with arrows. Figure taken from [95].

2.2 Nuclear Ground State Observables Inferred from the (Hyper)fine Structure

From the observed hyperfine spectrum the nuclear spin, the nuclear magnetic dipole moment and the nuclear electric quadrupole moment can be extracted. These ground state properties of the nucleus are vital for the understanding of nuclear structure phenomena and benchmark modern nuclear theories.
Moreover, the size of a nucleus has a measurable effect on the spectral lines and is therefore accessible by laser spectroscopy. A change in the neutron number leads to a different nuclear charge density distribution which results in a shift in the energy of the fine structure state (field or volume shift $\delta\nu_{\mathrm{FS}}^{A,A'}$ [11]) of two isotopes of the same element with mass numbers A and A'. Moreover, when adding or removing a neutron the mass of the nuclide changes and the energy of the fine structure state changes due to the different motion of the nucleus in the center-of-mass system (mass shift $\delta\nu_{\mathrm{MS}}^{A,A'}$ [11]). The difference in fine structure splitting of the two different isotopes constitutes the optical isotope shift [14] following

$$\delta\nu^{A,A'} = \nu_0^A - \nu_0^{A'} = \delta\nu_{\mathrm{FS}}^{A,A'} + \delta\nu_{\mathrm{MS}}^{A,A'}, \tag{2.6}$$

where ν_0^A is the centroid frequency of the HFS for the isotope A. The field shift is proportional to the change in mean square charge radii between two isotopes, which can hence be extracted from the measured isotope shift. The mean square charge radius of a nucleus describes the size of the contribution from the charged protons [14]. However, with CLS it is only possible to refer relative changes of the mean square charge radius between two different isotopes. The mean square charge radius is generally increasing with the number of nucleons building up the respective nucleus, however there exist some deviations of this trend around the magic numbers, where the nucleons are extraordinary well bound and a kink in mean square charge radius occurs. Therefore, the mean square charge radius gives insight into the nuclear shell structure.

2.3 Collinear Laser Spectroscopy (CLS)

Due to its high accuracy and resolution, CLS is an important experimental technique to access nuclear spins, electromagnetic moments, and mean square charge radii of short-lived radionuclides and hence provides insight into the nuclear shell structures [11, 14, 60]. Model-independent information on nuclear ground-state properties can be extracted from the observed hyperfine spectra.
For CLS a narrow-band continuous-wave (cw) laser beam is overlapped with a fast ion or atom beam. When the wavelength of the laser matches the energy difference of the selected electronic transition, the laser excites the ions or atoms. Fluorescence photons emitted by the excited atoms or ions can be detected in an ODR by PMTs. By counting the number of photons as a function of the scanned laser frequency a hyperfine spectrum of the selected optical transition is obtained.
In most CLS experiments it is not the laser frequency that is scanned but the velocity of the atoms or ions because it is easier to lock the laser frequency to a fixed reference frequency than to vary the laser frequency [11]. In the reference frame of the atoms or ions the laser frequency f_L is Doppler shifted according to the **relativistic Doppler effect** [11],

$$f = f_L \frac{1 - \cos(\alpha)\beta}{\sqrt{1-\beta^2}}, \tag{2.7}$$

where α is the angle between ion and laser beam. For collinear laser spectroscopy $\alpha \approx 0$ and for anticollinear laser spectroscopy $\alpha \approx 180$ degree. The relativistic Lorentz factor β is

$$\beta = \frac{v}{c} = \sqrt{1 - \frac{M_0^2 c^4}{(Uq + M_0 c^2)^2}}, \tag{2.8}$$

where c is the speed of light, v the velocity of the atoms or ions, U the total acceleration voltage and q and M_0 are the electric charge and rest mass of the accelerated ions. By changing the acceleration voltage and consequently the velocity of the atoms or ions the Doppler shifted frequency f that is seen by the atoms or ions can be scanned across the HFS while the laser frequency in the lab frame is locked to an accurate reference frequency f_L.

The **Doppler broadening** σ_f of the line shape due to the kinetic energy spread of the atoms or ions σ_E can be calculated by multiplying the first derivative of equation 2.7 with σ_E. In first approximation it holds for $\alpha = 0$ or $\alpha = 180$ degree that

$$\sigma_f \propto \frac{\sigma_E}{\sqrt{E}}, \tag{2.9}$$

where E is the kinetic energy of the atoms or ions. For the present discussion, higher order terms are negligible. The Doppler broadening versus the kinetic energy of the atoms or ions is shown in figure 2.3 for a mass of 24 u, a transition frequency f of 1,072,082,934.33 MHz corresponding to the D2 line of $^{24}Mg^+$ ions [6], and a typical experimental energy spread of 1 eV. The Doppler broadening is determining the spectral resolution. If high acceleration voltages are used the spectral resolution can be narrowed down to the natural linewidth **(Doppler compression)**. For $^{24}Mg^+$ ions the Doppler broadening at 30 keV is just ≈ 30 MHz for an energy spread of 1 eV whereas the natural linewidth is 42 MHz [4]. The hyperfine splittings for most of the isotopes are in the order of 10-1000 MHz [60] and can therefore be resolved by CLS using fast beams with a kinetic energy of >30 keV.

The **sensitivity** or signal-to-noise ratio of CLS is given by the number of atoms or ions, the probability of a laser induced transition from the ground to the excited state, the efficiency of the detection of the emitted fluorescence photons and the background rate due to scattered laser light, photomultiplier dark counts and light from ion collisions with residual-gas molecules [14]. By accommodating the ions in an ion cooler and buncher (see chapter 3.2) and releasing them as ion bunches with a well-defined time structure it is possible to reduce the background from scattered laser light. The photon signals are only accepted when the ion bunch is within the ODR such that a time-gated spectrum is obtained. By using bunched beams with a temporal bunch length of a few μs every 100 ms it is possible to improve the signal to background ratio by a factor of 10,000 compared to continuous ion beams [53]. For example, with the technique of using bunched ion beams the charge radii of $^{49,51,52}Ca$, that can only be produced with a production rate of a few hundred ions per second at ISOLDE/CERN, could be measured for the first time [32].

The **systematic error** on the measurement of the isotope shifts is mostly arising from the fact that the acceleration voltage U is typically known to about 10^{-4} relative uncertainty [11]. If necessary, this can be improved by performing collinear and anticollinear laser spectroscopy (quasi-)simultaneously. The

product of the resonance frequencies in the lab frame f_{L-} for anticollinear and f_{L+} for collinear laser spectroscopy as given in equation 2.7 is independent from the ion velocity or acceleration voltage,

$$f_{L+}f_{L-} = f^2\frac{1}{1-\beta^2}(1-\beta)(1+\beta) = f^2. \tag{2.10}$$

The square of the transition frequency in the rest frame of the atoms or ions can therefore be calculated from the product of the absolute resonance frequencies of the laser in the lab frame, which can be locked to well defined transition frequencies [14]. By making use of collinear and anticollinear laser spectroscopy simulataneously the charge radii of ^{7,9,10,11}Be could be determined with an accuracy in the isotope-shift measurements better than 1 MHz [63].

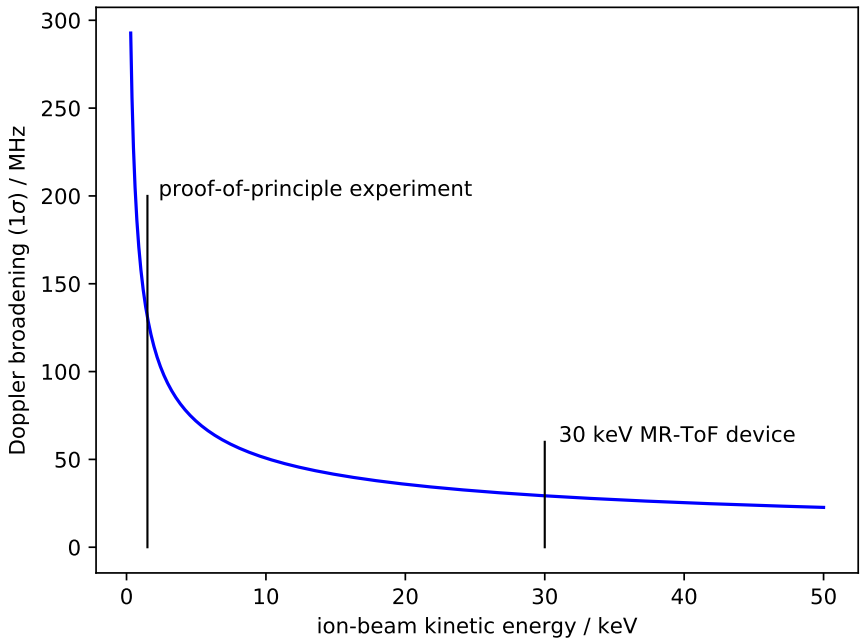

Figure 2.3: Doppler broadening σ_f versus the kinetic energy of the ions for an ion mass of 24 u, a transition frequency f of 1,072,08,934.33 MHz, and an energy spread of 1 eV. It is assumed that all the ions fly parallel to the laser beam axis. The ion-beam kinetic energies, where the MIRACLS' proof-of-principle experiment and the future MIRACLS' 30-keV MR-ToF device will be performed at, are marked with lines.

2.4 Line Shapes Obtained with CLS

The shape and linewidth of a transition in the hyperfine spectrum is given by several broadening mechanisms. The major influence of the line shape obtained with high-resolution CLS is the **natural linewidth**, that is represented by a Lorentz profile (see equation 2.12). The natural linewidth Γ arises due to the finite life time of the excited state τ and is given by $\Gamma = \frac{1}{2\pi\tau}$. For Mg^+, the natural linewidth is 42 MHz in the $3p\ ^2P_{3/2}$ and $3p\ ^2P_{1/2}$ states [4].

The **Doppler broadening** as described before has a Gaussian profile. For low ion-beam energies the

Doppler broadening is the most significant contribution to the linewidth, whereas for high ion beam energies (> 30 keV) it is in the order of the natural linewidth. For the derivation of the Doppler broadening above it is assumed that ion and laser beam are perfectly parallel. However, if some ion trajectories are not parallel to the laser beam an additional broadening arises depending on the angles between the ion paths and the laser beam. For this thesis, we define the Doppler limit as the Doppler induced linewidth broadening exclusively due to the ions' velocity (hence energy) spread, that is in the limit of perfectly parallel ion trajectories with respect to the laser beam. This is to distinguish it from the more general Doppler width which reflects the entire linewidth broadening due to equation 2.7, so the spread in the angles α between ions' trajectories and the laser beam as well as in energy.
Another broadening mechanism is the **power broadening** [8]. The laser photons do not only lead to an excitation from the lower to the upper level but also induce a stimulated emission which decreases the natural life time of an excited state. The linewidth increases with increasing laser power. Power broadening can be described by a Lorentz function.
If the interaction time of the atom or ion with the laser is small compared to the life time of the excited level a **transit time broadening** can occur, that is negligable for the present application of CLS [8].
Due to interactions with other particles a **pressure broadening** might occur [8]. The ion can be excited through collisions with other atoms or ions and when decaying back to the ground state the ion emits a fluorescence photon. This collisional excitation can not be distinguished from the laser induced excitation. A collision of the excited particle with another particle can also interrupt the emission process and lead to the so called collisional broadening. Moreover, the energy difference of the lower and upper level of the particle emitting a fluorescence photon might be changed due to the presence of other particles (Stark broadening). Pressure broadening effects are normally described by a Lorentz function. Due to the ultra-high vacuum in the ODR pressure broadening effects are normally negligible for CLS.

Taking into account all the broadening mechanism the resulting line shape is described by a Voigt profile that is a convolution of a Gauss and a Lorentz line shape. The Gauss profile is described by the function

$$G(x;\sigma) = \frac{1}{\sigma\sqrt{2\pi}} \exp\left(-\frac{x^2}{2\sigma^2}\right), \tag{2.11}$$

where σ is the standard deviation and the full width at half maximum (FWHM) is given by $\Gamma_G = 2\sigma\sqrt{2\ln 2} \approx 2.35\sigma$. The Lorentz profile is given by

$$L(x;\Gamma_L) = \frac{1}{\pi}\frac{\Gamma_L/2}{x^2 + (\Gamma_L/2)^2}, \tag{2.12}$$

where Γ_L is the FWHM. The Voigt profile is the convolution of a Gauss and a Lorentz profile

$$V(x;\sigma,\Gamma_L) = \int G(\tau;\sigma)L(x-\tau;\Gamma_L)d\tau. \tag{2.13}$$

A comparison of a Gaussian, a Lorentzian and a Voigt lineshape can be seen in figure 2.4. For a numerical approximation of the Voigt profile, the pseudo-Voigt profile is often employed, which uses a linear combination of the Gaussian and the Lorentz profile instead of their convolution.

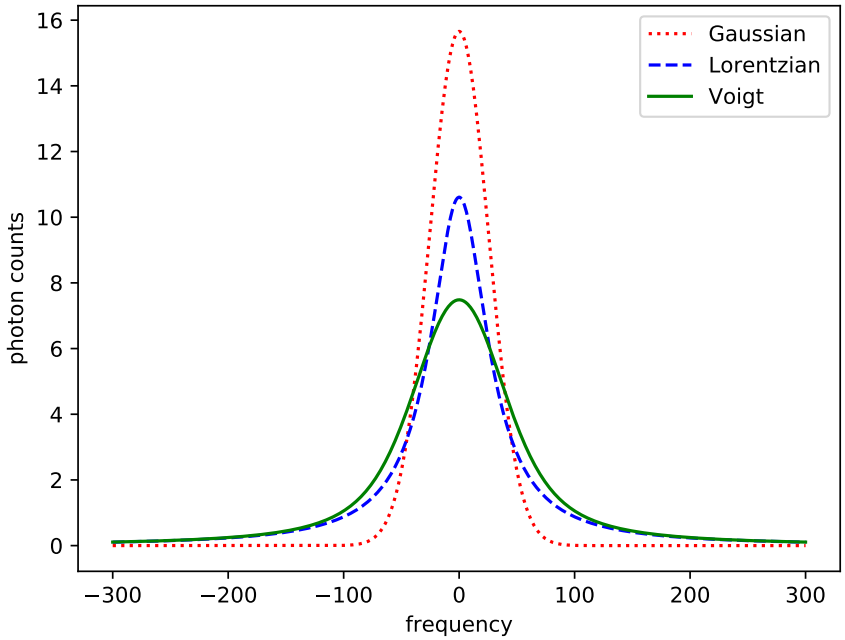

Figure 2.4: Comparison of a Gaussian, a Lorentzian and a Voigt line shape. The FWHMs of Gaussian and Lorentzian curve are the same. All curves are normalized to the same integral area.

2.5 COLLAPS: The Experimental Setup for CLS at ISOLDE

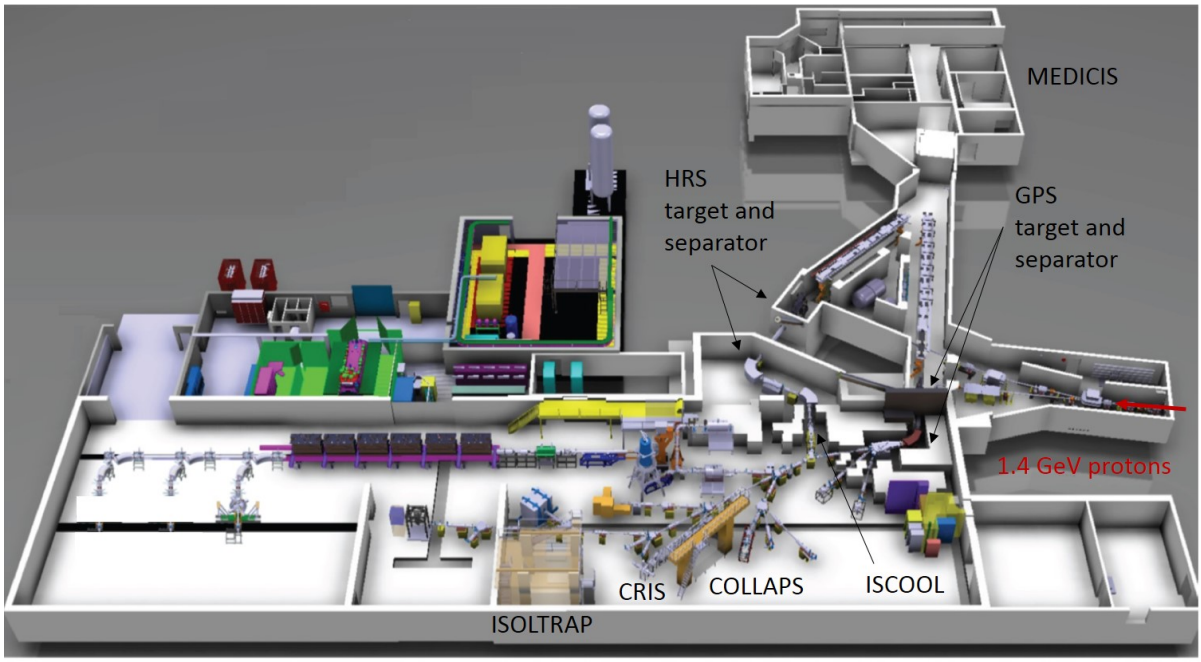

Figure 2.5: Overview over the ISOLDE experimental hall. Radionuclides are produced by bombarding a thick target with up to 1.4 GeV protons from the CERN proton synchrotron and ionised via surface, plasma or laser ionisation. After being mass separated at HRS or GPS the ions are transported to the respective experiments, such as ISOLTRAP [57] for high-precision mass measurements or CRIS [15] and COLLAPS [60] for high-precision laser spectroscopy. The linear Paul trap ISCOOL [3, 67] is used to obtain a bunched ion beam with low energy spread. See text for more details. Figure modified from [1].

CLS is performed at the on-line isotope separator ISOLDE at CERN, the European Organization for Nuclear Research, since 1978. A general overview over the ISOLDE experimental hall can be seen in figure 2.5. Proton pulses from the CERN proton synchrotron booster with intensities of around 10^{13} protons/pulse at 1.4 GeV are impinging on a thick target for the production of radionuclides. The proton synchrotron booster is one of the preaccelerators of the Large Hadron Collider. However, a large amount of the protons (typically $\sim$ 50% of all accelerated protons at CERN) are dedicated to ISOLDE, where they impinge on a thick target (e.g. uranium carbide) to create radioactive species through fission, spallation, and fragmentation. Presently close to 1100 radionuclides of more than 70 elements are available [57]. The produced radionuclides defuse out of the target and are ionized by surface, plasma or laser ionization. Among the ion sources, the Resonance Ionization Laser Ion Source (RILIS) [54] is of particular importance. With the help of RILIS the isotopes of one specific chemical element can be ionized since the unique, element specific 'fingerprint' in atomic energy level structure in each atom makes it possible to select one element out of many elements present in the atomic vapour by a multi-step resonance photo-ionization process. The ions are then accelerated up to 60 keV and the isotope of interest is mass-separated by dipole magnets of the High-Resolution Mass Separator (HRS) or the General Purpose Separator (GPS). Mass Resolving Powers $R = M/\Delta M$, where M is the mass of the ion of interest and ΔM is the mass difference to a beam contaminant, of up to 5000 can be reached at HRS [34]. Even when RILIS and one of the mass separators is used, the ion beam may still

be contaminated with isobars of other (surface) ionized elements. If the ions are mass separated by the HRS they are injected into a gas-filled Paul trap called ISCOOL [3, 67], to obtain an ion bunch (see chapter 3.2.3). Via transfer beam lines the ions are delivered to the different experimental stations at ISOLDE such as COLLAPS [53, 60], the experimental setup for CLS. A schematic overview of the COLLAPS setup is shown in figure 2.6.

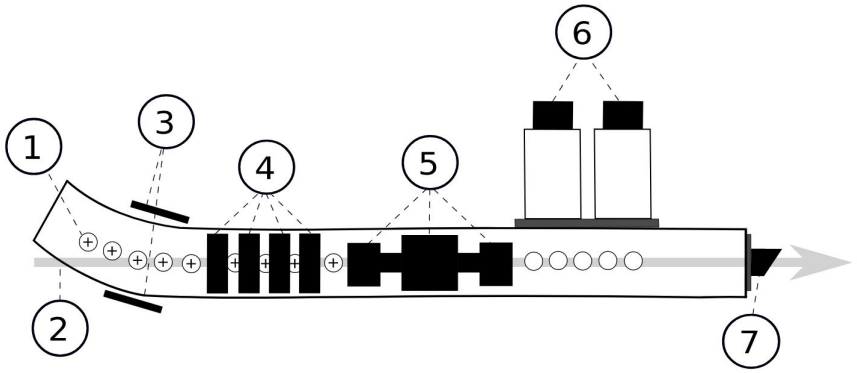

Figure 2.6: Setup of COLLAPS: 1, singly-charged ions; 2, laser beam; 3, electrostatic deflection plates; 4, post-acceleration electrodes; 5, charge exchange cell or tube; 6, PMTs; 7, Brewster window. Figure taken from [53].

At COLLAPS, the ion beam is bent by 10 degrees by electrostatic deflector plates and overlapped with the co- or anticollinear-propagating narrowband cw laser. In the post acceleration region the ions are accelerated or deaccelerated to change the laser frequency of the ions in their rest frame (see section 2.3). If the laser spectroscopy is performed on an atomic system, the ion beam is neutralized in a charge exchange cell. Otherwise the charge exchange cell is replaced by a drift tube. In the ODR, the ions or atoms are excited by the laser beam if the wavelength of the laser matches the energy difference of the selected electronic transition. Subsequently emitted fluorescence photons are counted by PMTs.

Chapter 3

Concepts and Fundamentals for CLS in a MR-ToF Device

In this chapter, the central concepts and experimental techniques such as emittance of an ion beam, Paul traps, and electrostatic ion beam traps will be introduced which subsequent chapters are based on. At the end, a more detailed overview over the concept of MIRACLS will be given together with the calculation of the improvement factor in sensitivity of MIRACLS in comparison with traditional CLS techniques.

3.1 Emittance

A particle beam can be described as an ensemble of point-like particles, where the motion for each single particle at any given point of time t is described in a 6-dimensional phase space consisting of three space coordinates (x,y,z) and three momentum coordinates (p_x, p_y, p_z). If the momentum components of the particles in longitudinal direction p_x are much larger than the momentum components in transversal directions p_y and p_z the particles form a beam. The momentum coordinates in transversal direction p_y and p_z can be replaced according to [68]

$$\begin{aligned} y' = dy/dx = \frac{dy/dt}{dx/dt} = \frac{p_y}{p_x} = \tan(\theta_y) \approx \theta_y \\ z' = dz/dx = \frac{dz/dt}{dx/dt} = \frac{p_z}{p_x} = \tan(\theta_z) \approx \theta_z, \end{aligned} \tag{3.1}$$

where $\theta_{y,z}$ is the angle between the longitudinal and the respective transversal direction. Due to $p_x >> p_{y,z}$ the approximation $\tan(\theta_{y,z}) \approx \theta_{y,z}$ holds. Therefore y' and z' can be seen as angles with units in radians. Every particle represents a point in the (y, z, y', z')-space also called trace space [68] at any given distance x along the beam propagation direction. Due to the fact that the 6-dimensional phase space or the 4-dimensional trace space are difficult to visualize in all the full dimensions, projections into two dimensional action planes are carried out [55]. The four dimensional trace space is projected into the (y, y') and (z, z')-plane and the six dimension phase space into the $(x, p_x), (y, p_y)$ and (z, p_z)-plane or into the $(x, p_x), (y, y')$ and (z, z')-plane.
Provided that just conservative forces are applied to the particles, the volume of the particle beam in the six dimensional phase space will remain constant over time according to the Lioville theorem. If the forces acting in the $x-, y-, z-$directions are decoupled then the areas of the three individual sub spaces $(x, p_x), (y, p_y), (z, p_z)$ or $(x, p_x), (y, y'), (z, z')$ are conserved as well.
The area occupied by the particles in the sub spaces $(x, p_x), (y, y'), (z, z')$

$$A_u = \int\int du\ du' \text{ with } u = x, y, z \text{ and } u' = p_x, y', z' \tag{3.2}$$

is related to the transversal or longitudinal emittance of the beam [55].
Throughout literature there exist many different methods for the calculation of emittance ϵ. One way is to calculate the whole area occupied by the particles as done in equation 3.2. This emittance will be called ϵ_{100} because the area contains 100% of the particle beam. Similar a p% emittance ϵ_p can be defined by calculating the area enclosing a specific percentage p of the particle beam.
The area occupied by the beam in the (u, u') trace space with $u = y, z$ has an elliptical shape if all the forces acting on the particles are directly proportional to the particle's displacement u from the beam axis [68]. If the ellipse enclosing p% of particle beam has an upright position with major axes u_m and u'_m then the trace space area is the same as the area of the ellipse and the p%-transversal emittance follows as

$$\epsilon_p = \pi u_m u'_m. \tag{3.3}$$

In this case the transversal emittance can be defined as the product of the spatial width u_m and the angular divergence u'_m of the particle beam. The measurement units for transversal emittances are mm mrad. As follows from equation 3.1 the transversal emittance as defined above depends on the momentum coordinate p_x of the particle beam in longitudinal direction. For the emittance comparison of beams with different kinetic energies one therefore has to normalize the transversal beam emittance according to [28], $\epsilon_{\text{normalized}} = \epsilon\langle p_x\rangle$, where $\langle p_x\rangle$ is the average momentum in longitudinal direction.

In the case of bunched beams the sub space (x, p_x) has to be included to be able to describe the beam in the whole six dimensional phase space. The longitudinal emittance is related to the area occupied by the particles in the sub space (x, p_x) [55], see equation 3.2. The measurement unit of the longitudinal emittance is eV μs.

Alternatively, there exists a statistical definition of emittance that uses the moments of the particle distribution (the mean value of u is $\langle u\rangle$ and the mean value of u' is $\langle u'\rangle$),

$$\begin{aligned}
\langle u^2\rangle &= \int\int du du' f(u,u')(u - \langle u\rangle)^2 \\
\langle u'^2\rangle &= \int\int du du' f(u,u')(u' - \langle u'\rangle)^2 \\
\langle uu'\rangle &= \int\int du du' f(u,u')(u - \langle u\rangle)(u' - \langle u'\rangle),
\end{aligned} \tag{3.4}$$

where $f(u, u')$ is the phase space density function of the particle beam and $u = y, z, E$ and $u' = y', z', t$ with E as the kinetic energy and t as the time-of-flight of the particles. The second central moment $\langle u^2\rangle$ is often called variance and is related to the standard deviation σ_u via $\langle u^2\rangle = \sigma_u^2$. The moment $\langle uu'\rangle$ is called covariance and reflects a linear correlation between u and u'. The statistical transversal rms emittance is given by [68, 28]

$$\epsilon_{\text{rms},u} = \pi\sqrt{\langle u^2\rangle\langle u'^2\rangle - \langle uu'\rangle^2} \tag{3.5}$$

with $u = y, z$ and $u' = y', z'$. If there is no correlation between u and u' the statistical rms emittance simplifies to

$$\epsilon_{\text{rms},u} = \pi\sigma_u\sigma'_u. \tag{3.6}$$

The statistical longitudinal rms emittance can in analogy to the statistical transversal rms emittance calculated by

$$\epsilon_{\mathrm{rms,long}} = \sqrt{\langle E^2\rangle\langle t^2\rangle - \langle Et\rangle^2}. \tag{3.7}$$

If there is no correlation between E and t the statistical rms emittance simplifies to [55]

$$\epsilon_{\mathrm{rms,long}} = \sigma_E \sigma_t, \tag{3.8}$$

and the bunch is focused into a time focus, where σ_E is the energy spread of the beam pulse and σ_t is the time duration of the pulse at the time focus. After electrostatic acceleration, the particles at the end of the pulse often have a higher energy than the particles at the beginning of the pulse and therefore the higher energetically particles will 'overtake' the slower ones at the time focus.

If a few particles are in the outer region of the phase space the statistical rms emittance can get very large even though the quality of the beam enclosing most of the particles is excellent. Therefore a p%-emittance is often preferred over the rms emittance to describe the beam quality of a particle beam. If a Gaussian beam is assumed the statistical rms emittance can be converted to the p%-emittance by a multiplication with a specific scaling factor that can be found in table 3.1 [40, 23].

Table 3.1: scaling factor to convert the rms emittance ϵ_{rms} into the p%-emittance ϵ_p

scaling factor ($= \epsilon_p/\epsilon_{\mathrm{rms}}$)	1	4	6	9
percentage p of the enclosed particle beam	39	87	95	99

3.2 Paul Traps

3.2.1 Working Principle

The trapping of a particle with charge e in a small volume requires a potential energy minimum at some point in space. However, the Earnshaw Theorem states that it is not possible to hold particles in a stable equilibrium by applying electro- or magnetostatic forces alone. However, by using time dependent electric fields charged particles can be confined in a small volume. The first rf-based ion trap was described by Wolfgang Paul in the 1950s [64]. Since then ion traps gained in importance for mass spectrometry, cluster physics, atomic and nuclear physics, biophysics and many other physical fields. In the following section the working principle of a Paul trap is explained. We assume a harmonic binding force $\mathbf{F}$ that increases linearly with the distance $\mathbf{r} = (x, y, z)$ of the elastically bound particles from the centre of the trap, $\mathbf{F} \propto -\mathbf{r}$. From $\mathbf{F} = -e\nabla\Phi$ a parabolic potential,

$$\Phi = \frac{\Phi_0}{2r_0^2}\left(\alpha x^2 + \beta y^2 + \gamma z^2\right), \tag{3.9}$$

follows, where α, β, γ are some constants, r_0 is a normalization factor and Φ_0 can be a time dependent function. The constants α, β, γ must fulfil the Laplace condition $\Delta\Phi = 0$ that leads to $\alpha + \beta + \gamma = 0$. For the case of a rotational symmetry around the z axis it follows that $\alpha = \beta = 1$ and $\gamma = -2$. This solution corresponds to the standard Paul trap that is for example explained in [10, 49]. Due to the

fact that nowadays many experiments use linear Paul traps because they are easier to manufacture and to align the present discussion is restricted to linear Paul traps. A linear Paul trap is quite similar to the historical quadrupole mass filter, that was first described in [64]. For a quadrupole mass filter the solution $\alpha = 1 = -\beta$ and $\gamma = 0$ is used, that leads to a two dimensional quadrupole potential field

$$\Phi = \frac{\Phi_0}{2r_0^2}\left(x^2 - y^2\right). \tag{3.10}$$

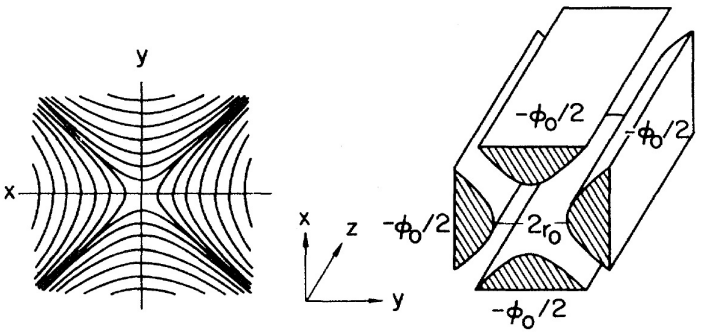

Figure 3.1: Quadrupole mass filter: Left: Equipotential lines for a plane quadrupolar field, Right: The electrode structure for the mass filter. Figure slightly modified from [64].

The potential field can be generated by four hyperbolically shaped electrodes, where a harmonically oscillating potential is applied between adjacent electrodes (see figure 3.1). The applied voltage Φ_0 is a superposition of a DC voltage U and a RF voltage V with a driving frequency ω,

$$\Phi_0(t) = U + V\cos(\omega t). \tag{3.11}$$

Instead of hyperbolically shaped electrodes often four cylindrical rods (see e.g. [10]) are used due to the fact that they can be easier produced and aligned. In good approximation, the field remains quadrupolar in the middle of those cylindrical rods.
The equations of motions of a particle inside a quadrupolar mass filter result from the Lorentz force of a charged particle in an electrostatic field $\mathbf{F} = -e\nabla\Phi$,

$$\begin{aligned} m\ddot{x} &= -e\frac{\Phi_0}{r_0^2}x \\ m\ddot{y} &= e\frac{\Phi_0}{r_0^2}y \\ m\ddot{z} &= 0. \end{aligned} \tag{3.12}$$

The first two equations of motion can be rewritten to

$$\begin{aligned} \ddot{x} + \frac{e}{mr_0^2}(U + V\cos(\omega t)) = 0 \\ \ddot{y} - \frac{e}{mr_0^2}(U + V\cos(\omega t)) = 0 \end{aligned} \tag{3.13}$$

or in dimensionless parameters a, q and τ to [64]

$$\begin{aligned} \frac{d^2x}{d^2\tau} + (a + q\cos(2\tau))x = 0 \\ \frac{d^2y}{d^2\tau} - (a + q\cos(2\tau))y = 0. \end{aligned} \tag{3.14}$$

The dimensionless parameters a, q and τ are given by

$$a = \frac{4eU}{mr_0^2\omega^2},\ q = \frac{4eV}{mr_0^2\omega^2},\ \tau = \frac{\omega t}{2}. \tag{3.15}$$

These differential equations are called Mathieu equations [75], that have two types of solutions. One type is stable, where the motion of the particle around the z axis is stable with limited amplitudes in x and y directions. The other solution type leads to an unstable motion and the particles will be radially lost. The parameters a and q define whether stability is achieved or not. A stability diagram is depicted in figure 3.2. Only a and q values within the overlapping area for x and y stability (marked in red) lead to a radial confinement of the ions [64]. Since there is no confining force in all three directions, in a quadrupolar mass filter it is not possible to trap the ions in a small volume.

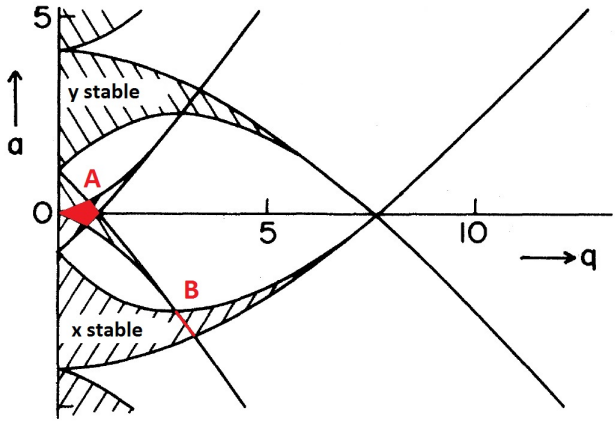

Figure 3.2: Stability diagram for the dimensionless parameters a and q for a quadrupolar mass filter. The regions for stable motions of the quadrupolar mass filter are marked with A and B. See text for details. Figure modified from [64].

A linear Paul trap is in principle just a quadrupolar mass filter, where a DC voltage confinement along the longitudinal z axis is added such that the particles are confined in all three dimensions [53]. The longitudinal confinement is achieved by segmenting the rods of the quadrupolar mass filter and applying a static DC voltage to the rods in the outer segments, such that a potential minimum is created along the z axis. A schematic drawing of a linear Paul trap together with the longitudinal trapping potential is depicted in figure 3.3. The particle performs a harmonic oscillation along the longitudinal axis z, while its transversal motion is still - approximatively - described by equations 3.13. However, the axial DC potential has a defocusing effect in the radial plane that leads to different radial motions of the particles. Therefore, the stability diagram for a linear Paul trap is different to that for a quadrupolar mass filter [21] and depends on the applied axial DC potential. In a linear Paul trap the ions can be

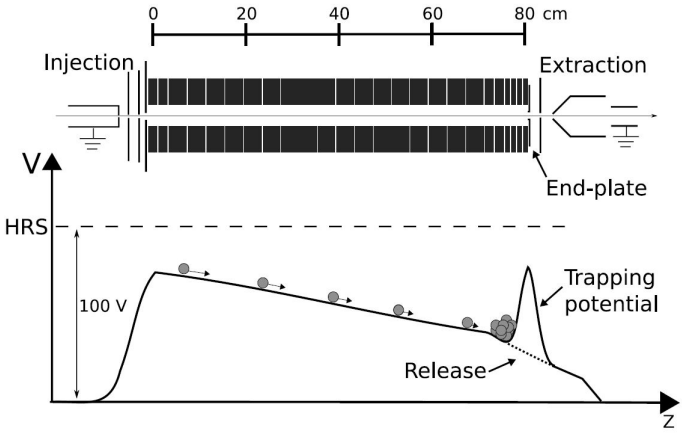

Figure 3.3: The upper half of the picture shows a schematic side view of a linear Paul trap. By applying different potentials to the segments of the rods a DC potential along the longitudinal axis z is created (lower half of the picture). The ions are longitudinally trapped at the potential minimum. Figure taken from [53].

trapped in all three dimensions. Storage times of many hours are reached when the pressure inside the Paul trap is 10^{-10} mbar to avoid collisions with neutral background atoms or molecules [10].

3.2.2 Paul Traps used as Ion Coolers and Bunchers

Linear Paul traps can be used for cooling and bunching of ion beams. When ions enter a linear Paul trap which is filled with buffer gas they interact with the buffer gas atoms [20]. Provided that the ion energy is less than a few electronvolts and the ion masses are much larger than the masses of the buffer gas atoms, the interaction of the ions with the buffer gas atoms can be described by an average damping force [35, 49]

$$\mathbf{F} = -\delta m \mathbf{v}, \tag{3.16}$$

where m is the mass and $\mathbf{v}$ the velocity of the ions. The damping coefficient δ is proportional to the gas pressure and inversely proportional to the temperature. The cooling and accumulation process in a linear Paul trap is shown in figure 3.4. The longitudinal and transversal oscillation amplitudes of the ions are damped very quickly until an equilibrium with the driving electric field and the buffer gas temperature is reached. Thereby the ions lose transverse and longitudinal energy due to elastic collisions with the buffer gas atoms and move closer to the centre of the potential minimum as shown in figure 3.4(b). If the masses of the buffer gas atoms are equal or even larger than the ion masses the viscous damping approach as described above is no longer valid [35]. When an ion is colliding with a heavier buffer gas atom a phase jump of the motion in respect to the radio frequency can take place which leads to an increase of the kinetic energy of the ions. This RF heating is the main reason for ion losses in linear Paul traps if light ions and heavy buffer gas atoms are present. When heavy ions such as Ba^+ or Pb^+ are trapped in a Paul trap filled with He, N_2 or Ne buffer gas at pressures of 10^{-4} mbar, storage times of many days could be reached [10].

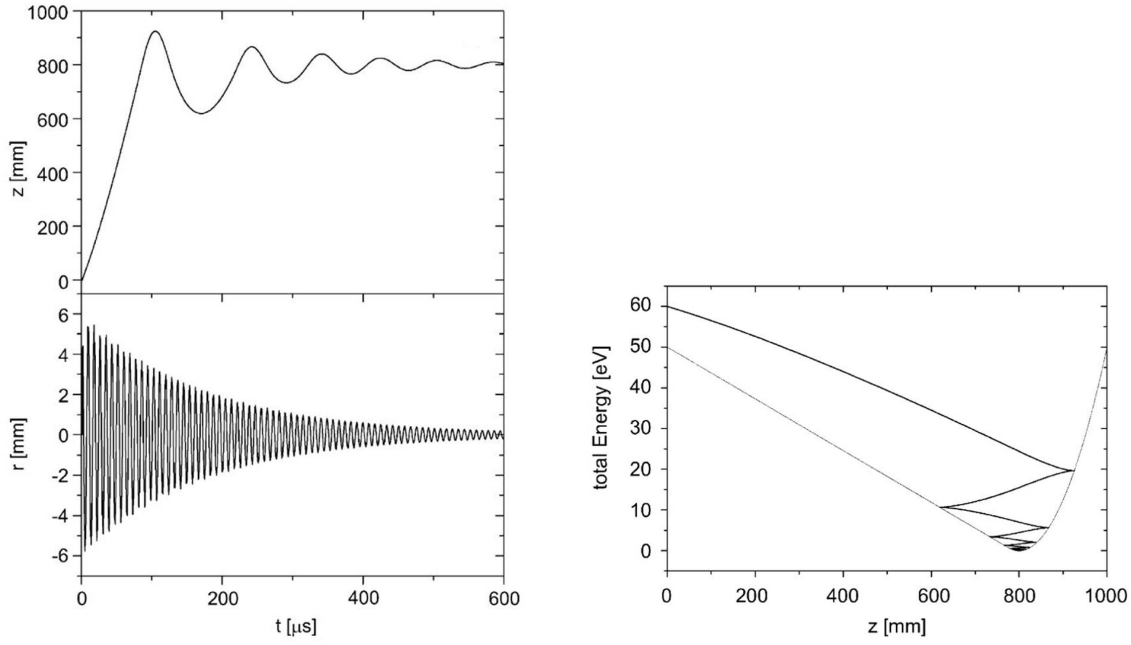

(a) (b)

Figure 3.4: Simulations of the accumulation and cooling process of $^{39}K^{+}$ ions in a linear Paul trap with the assumption of a viscous damping force: (a) longitudinal (top) and transversal oscillation (bottom) as a function of time, (b) the total energy as a function of the longitudinal position z. Figure taken from [35].

3.2.3 ISCOOL - The Radio-Frequency-Quadrupole (RFQ) Cooler and Buncher at ISOLDE

AT ISOLDE, the linear Paul trap ISCOOL is installed after the High Resolution Separator (HRS) and it provides cooled and bunched beams for laser spectroscopy experiments. ISCOOL was put into operation in 2008. The technical design of the electrodes of ISCOOL can be found in [3, 67]. ISCOOL consists of four rods, that are coupled pairwise. Between the adjacent electrodes an oscillating potential is applied, that leads to a radial confinement of the ions. The four rods are surrounded by 25 segmented DC electrodes, that cause an axial trapping potential as shown in figure 3.3. Separating the RF and DC potentials allows a simplified electronics system. The trap is filled with the noble gas helium to cool the incoming ion beam through collisions with the helium buffer gas.
An incoming beam from the HRS has a kinetic energy of typically 30-60 keV and the beam is therefore decelerated down to a few tens of electronvolts before the beam is injected into the Paul trap. For this purpose, the whole Paul trap is floated to a potential slightly below the corresponding ion beam energy and the kinetic energy of the ions is reduced when the ions „climb“ the potential hill. Proper deceleration is achieved by dedicated deceleration optics [39]. The first segments of the linear Paul trap produce a drag field, that guides the ions along the longitudinal axis to the potential minimum, where the actual trapping takes place (see figure 3.3) [53]. After passing the trap once in axial direction the kinetic energy of the ions is reduced due to buffer-gas collisions such that it is lower than the axial potential barrier and the ions 'thermalize' into the potential minimum.
The number of trapped ions is given by the incoming ion current, capture and trapping efficiency, as well as by the loading time, e.g. the time when the ions are injected into the Paul trap. However if

the space charge limit of a Paul trap is reached, it is not possible to trap more ions by increasing the loading time [78]. Repulsing Coulomb forces between the ions can not be neglected if a certain number of trapped particles is reached and the spatial distribution of the ions increases and some of the ions are therefore lost in the Paul trap. Moreover, large concentrations of charged particles can distort DC and RF fields as observed from the ions.

For ejection of the ion bunch out of the trap the last DC segments are switched to a lower potential as indicated in figure 3.3. This creates a potential ramp and the ions are extracted as an ion bunch. Therefore ISCOOL creates a bunched ion beam with a low energy spread. To our knowledge, the longitudinal emittance of ISCOOL was never directly measured. Laser Spectroscopy measurements of COLLAPS show that the energy spread is less than 1 eV (1 standard deviation σ) and the time spread (95%, therefore 2σ) is around 5 μs [52]. The longitudinal rms emittance is therefore around 2.5 eV μs. Note that this value is just an estimation out of the data obtained from laser spectroscopy measurements and the longitudinal rms emittance can actually be smaller, especially for smaller ion intensities in which space-charge effects are less important. After the ejection of the ions from ISCOOL the ions are re-accelerated back to 30-60 keV. The transversal emittance enclosing 95% of the beam (ϵ_{95}) is reported to be less than 3π mm mrad at 30 keV and the statistical rms emittance is reported to be 2π mm mrad [30, 22]. Note, that the conversion factor between the 95%-emittance and the rms emittance is not 6 because the beam ejected from ISCOOL is not Gaussian.

3.2.4 Transversal and Longitudinal Emittance of Paul traps

If in an ion cooler and buncher filled with buffer gas at temperature T the ions are cooled until thermal equilibrium is reached, the thermal limit of the longitudinal 95%-emittance of a beam extracted from the trap in the phase space (z, p_z) is [79, 55]

$$\epsilon_{95,\mathrm{long}} = 2\pi \ln(20) \frac{k_B T}{\omega_z}, \tag{3.17}$$

where k_B is the Boltzmann constant. Stored ions with charge e and mass m move in the longitudinal trapping potential with an oscillation frequency of [79, 55]

$$\omega_z = \sqrt{\frac{2C_2 e}{m}}. \tag{3.18}$$

The axial potential $U(z)$ is in the region of the potential minimum in good approximation a parabolic function,

$$U(z) = U_0 + C_2(z - z_0)^2, \tag{3.19}$$

where U_0 is the minimum potential at $z = z_0$ and C_2 is a constant describing the potential well.

The transversal 95%-emittance can be calculated according to formula 3.17 where the axial frequency ω_z is replaced by the macro-motion frequency ω_{macro} [79, 55],

$$\omega_{\mathrm{macro}} = \frac{q\omega}{\sqrt{8}}, \tag{3.20}$$

with ω as the circular RF frequency and q as the Mathieu parameter given in equation 3.15. Moreover, equation 3.17 is divided by the momentum coordinate in longitudinal direction p_z [79, 55],

$$\epsilon_{95,\text{trans}} = \frac{2\pi \ln(20) \frac{k_B T}{\omega_{\text{macro}}}}{p_z}, \tag{3.21}$$

where $p_z = m\sqrt{\frac{2E}{m}}$, and E is the mean kinetic energy of the ions.

3.3 Multi-Reflection Time-of-Flight Devices

3.3.1 General Overview

An electrostatic ion beam trap [2, 7, 45, 96], also called MR-ToF (Multi-Reflection Time-of-Flight) device [65, 66, 77, 88, 90, 93], is a storage device for ions that is based purely on electrostatic fields. Most MR-ToF devices consist of two electrostatic coaxial ion mirrors, that are separated by a drift space as can bee seen in figure 3.5. The ion bunch is bouncing back and forth between the two electrostatic mirrors, where the ion bunch is reflected. On first sight, a MR-ToF device seems to violate the Earnshaw theorem. However, in the case of a MR-ToF device the kinetic energy of the ions is not 0 and the field in a MR-ToF device is changing in the rest frame of the ions, so there is no contradiction to the Earnshaw theorem. The first predecessor of an electrostatic ion beam trap dates back to the early 1960s [87]. The ions were forced to perform a few oscillations between two plain electrodes. 30 years later the electrostatic ion beam trap was invented where the ion trajectories are folded into a table top device and an extended flight path was achieved [7, 93, 96] by trapping the ions for more than 1000 revolutions. The first electrostatic ion beam traps were used to study the interaction between molecular ions with electrons, photons, atomic or molecular ion beams and the resulting molecular fragments were measured by a detector located in the trap [96]. Later on, MR-ToF devices gained in importance for precision mass measurements and mass separation of short-lived radionuclides throughout the world (see e.g. [65, 66, 77, 88, 90]).

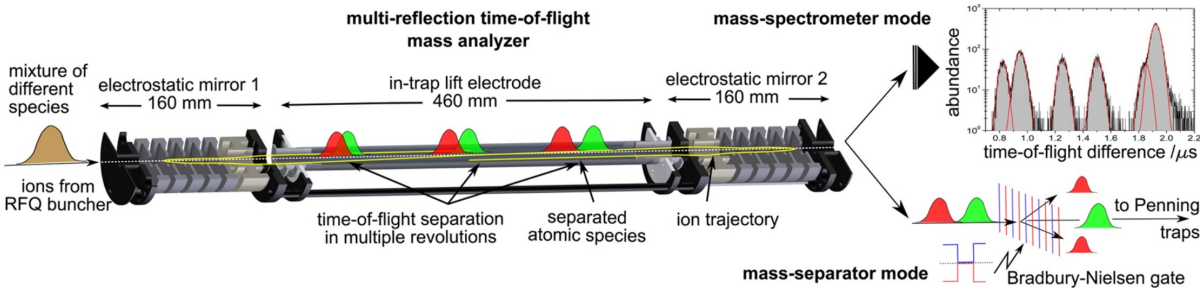

Figure 3.5: ISOLTRAP's MR-ToF device as a mass spectrometer (upper right) or as a mass separator (lower right). One ion trajectory is drawn in yellow and the mass-over-charge separation of different ion species during the ions' revolutions in the device is illustrated. See text for more details. Figure taken from [91].

Since 2010 ISOLTRAP [57], an experimental setup at ISOLDE/CERN for high-precision mass measurements on short-lived radionuclides, has used a MR-ToF device [91], that opened the path for measuring the masses of exotic radionuclides, see e.g. [88]. A schematic overview of the ISOLTRAP's MRToF

device is depicted in figure 3.5. A mixture of ion species with different masses m_i and charge states z_i is ejected out of ISOLTRAP's RFQ Cooler and Buncher [35] such that the ions gain by acceleration via an electrostatic potential difference U a kinetic energy of

$$E_{\text{kin}} = z_i e U = \frac{1}{2} m_i v_i^2, \tag{3.22}$$

where e is the elementary charge and v_i is the velocity of an ion. After ejection from the RFQ cooler and buncher the ions are injected into the MR-ToF device, where they are separated according to their mass-over-charge ratio m_i/z_i since the time-of-flight t_i for one ion species follows

$$t_i = \frac{s_i}{v_i} = s_i \sqrt{\frac{m_i}{2 z_i e U}}. \tag{3.23}$$

Here, s_i is the length of an ion trajectory in the MR-ToF device. After a specific number of revolutions r with a revolution period of t_1, the ions are ejected from the MR-ToF device and can be resolved on an ion detector for mass measurements (mass-spectrometer mode). The mass resolving power R of the ions at the ion detector plane follows as [91]

$$R \equiv \frac{m}{\Delta m} = \frac{t}{2\Delta t} = \frac{t_0 + r t_1 + t_d}{2\sqrt{\Delta t_0^2 + (r \Delta t_1)^2}}, \tag{3.24}$$

where t is the total flight time and Δt is the time-of-flight width at the detector plane. The total flight time is a sum of the time the ions need from the RFQ cooler and buncher into the middle of the MR-ToF device t_0 and of the time that the ions are trapped in the MR-ToF device $r t_1$ as well as the time the ions travel from the ejection of the MR-ToF device to the ion detector t_d. The signal width at the detector plane is given by the initial bunch width provided by the RFQ cooler and buncher Δt_0 and by contributions from the dispersion per turn of the MR-ToF device $r \Delta t_1$. For a large revolution number the mass resolving power is eventually limited by the dispersion of the MR-ToF device,

$$\lim_{r \to \infty} R = \frac{t_1}{2\Delta t_1}. \tag{3.25}$$

The initial bunch width Δt_0 determines the number of revolutions that are necessary to approach the maximum of $t_1/(2\Delta t_1)$. In figure 3.6 the mass resolving power for an ion of a mass-over-charge state of $A/z = 90$ of the ISOLTRAP's MR-ToF Mass Spectrometer can be seen in comparison to ISOLTRAP's precision Penning trap [57]. If the half-life of the nuclides is below 100 ms the mass resolving power of the MR-ToF device is up to an order of magnitude higher than that for the Penning trap. Moreover, nuclides with very low production yields, that were not accessible for Penning traps, could be measured in the MR-ToF mass spectrometer due to its higher sensitivity. As an additional benefit, for the reduction of systematic errors, well-known species can be used in a MR-ToF device as simultaneous mass markers, that would be considered as unwanted contaminants in the case of mass measurements with Penning traps.

Alternatively to the use of the MR-ToF device as a mass spectrometer it can also be used as a mass separator [90]. Therefore, after the MR-ToF device a Bradbury-Nielsen Gate [94] is installed that separates the ions of interest from unwanted contaminants. All the unwanted species are deflected while the ions of interest are transmitted by switching off the deflection fields of the Bradbury-Nielsen Gate for a short time interval. At ISOLTRAP the MR-ToF device is installed between the RFQ cooler and

buncher and the two Penning traps and has significantly increased ISOLTRAP's capability of purification of contaminated ion beams [90].

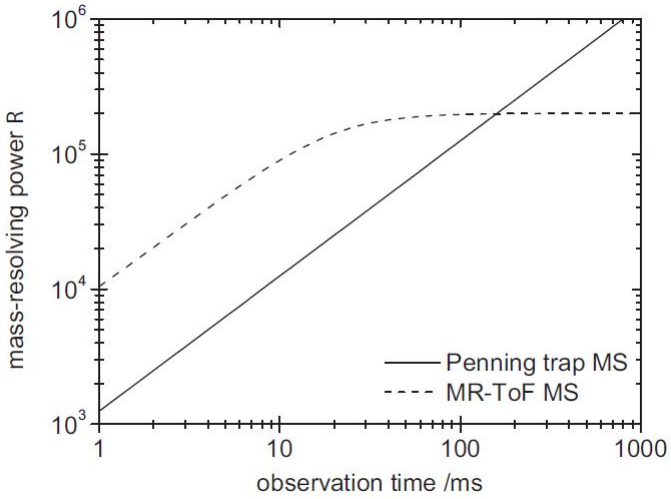

Figure 3.6: Mass resolving power as a function of the observation time for the ISOLTRAP's MR-ToF mass spectrometer and the Penning trap mass spectrometer. The mass-over-charge ratio A/z is 90. Figure taken from [91].

3.3.2 Working Principle of MR-ToF Devices

3.3.2.1 Confinement of Ions

For the axial confinement in the MR-ToF device the ion kinetic energy E_{kin} in the drift tube, located between the two electrostatic mirrors, has to be lower than the potential maxima of the two mirrors,

$$E_{\text{kin}} < ezU(x), \tag{3.26}$$

where ez is the ion charge and $U(x)$ is the electric potential along the MR-ToF axis x. The axial confinement is done by the outermost mirror electrodes, to which in the case of cations a positive potential $U(x)$ or in the case of anions a negative potential $U(x)$ is applied. The innermost mirror electrodes are used as lenses that ensure radial ion refocusing during each revolution. Typical MR-ToF devices consists of 1-2 electrodes constituting the lens potential and 3-4 electrodes forming the trapping potential. All 4-6 electrodes are normally referred to as mirror electrodes.

3.3.2.2 Injection and Ejection

For injection and ejection of the ions one can either switch one mirror to another potential such that the ions can pass the mirror (mirror switching [18]) or change the kinetic energy of the ions in the MR-ToF device (in-trap lift switching [92]). A schematic comparison between in-trap lift switching and mirror switching is shown in figure 3.7. For both cases it is assumed that the ion bunch is coming from the left and should be ejected to the right after being trapped in the MR-ToF device. For mirror switching the entrance mirror (left) is switched to ground potential and the ions can enter the drift region. Once the ions are in the middle of the drift region the mirror is switched back to its trapping value and the ion

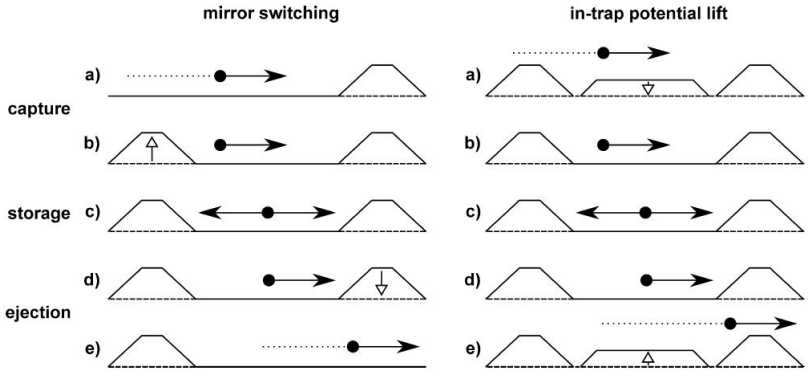

Figure 3.7: Schematic comparison of ion capture, storage and ejection between the techniques of mirror switching (left) and in-trap lift switching (right). Figure taken from [92].

kinetic energy does not exceed the mirror potential anymore. After storing the ions for some revolutions in the MR-ToF device the exit mirror (right) is switched to ground and the ions are ejected from the MR-ToF device.
In the case of in-trap lift switching a potential U_{lift} is applied to the drift tube, that is also often called lift tube. The incoming ions have a kinetic energy ezU_{transfer} that is larger than the potentials applied to the mirrors. The ions can therefore pass the first mirror. Once the ions are in the middle of the central drift tube its potential is switched to ground potential. Thus, the ions are trapped between the two mirrors as their resulting energy $E = ezU_{\text{transfer}} - ezU_{\text{lift}}$ is no longer high enough to pass the mirrors. After a certain number of revolutions the potential of the drift tube is switched to U_{lift} again when the ions are in its center and the ions can leave the MR-ToF device. The in-trap lift switching technique avoids switching the sensitive mirror potentials and therefore electric noise and fluctuations of the mirror potentials can be held at a minimum. Moreover, the kinetic energy in the MR-ToF device can be easily adjusted when the in-trap lift switching technique is applied without changing any potential outside the MR-ToF device.

3.3.2.3 Extra Features

Electric fields from lenses or other electrooptical elements close to the MR-ToF region can distort the mirror potentials and should therefore be shielded. Thus, many recently built MR-ToF instruments use grounded **shielding electrodes** [25, 37] to minimize these fringe-field effects. Those electrodes can be located before and after the MR-ToF device or between the mirrors and the drift tube. Often the inner diameter of the outer most mirror electrode is smaller than the inner diameter of the other mirror electrodes to prevent fields from outside reaching into the MR-ToF device.
One can add a further azimuthally segmented tube between the mirror electrodes and the in-trap lift which can be used as **deflector electrodes** [25]. Due to the mass-over-charge separation in a MR-ToF device different ion species will pass the deflector electrodes at different times. If all deflector electrodes are grounded there is no resulting electric field and the ions of interest can transverse undisturbed. If a potential difference is applied between the deflector electrodes the unwanted ions are deflected and no longer stored in the MR-ToF device. This ion separation is performed in the MR-ToF device simultaneously with the mass resolving process and no additional external devices are needed. Morover, space-charge effects due to too high amounts of non-isobaric contaminant ions are suppressed because the contaminants can quickly be ejected without disturbing the ions of interest.

Pick-up electrodes [12] located between the mirror electrodes and the lift tube can be used for measuring the mirror charges that the electrodes pick up every time when the ion bunch passes them. Hence, those electrodes represent an interesting non-destructive diagnostic tool for the ion motion in a MR-ToF device.

3.4 The Multi Ion Reflection Apparatus for CLS - MIRACLS

3.4.1 General Concept of MIRACLS

Conventional CLS, like COLLAPS at ISOLDE, is limited to nuclides with production yields of typically more than a few 1000 - 10,000 ions/s delivered from an ion source, depending on the specific case and optical transition. To measure the most exotic nuclides far from stability, that can already be produced with low production yields at today's radioactive ion beam facilities like ISOLDE, novel experimental techniques have to be envisioned. In conventional CLS, the radioactive ions interact with the laser beam in the time scale of some microseconds, whereas the half-life of the ions is between tens of milliseconds to seconds or even larger. In principle one can increase the interaction time of the ions with the laser beam by increasing the length of the optical detection region (ODR) by adding more PMTs, but this would be relatively expensive without a significant gain in sensitivity.

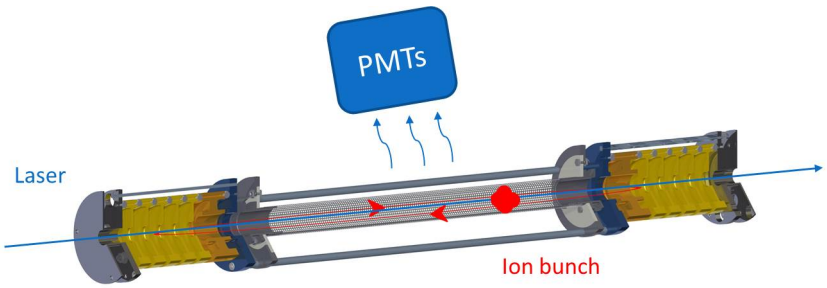

Figure 3.8: Schematics of the concept of MIRACLS: A bunched ion beam is trapped in a MR-ToF device in which the ion bunch and the laser beam can interact during each revolution.

To make use of the rare isotopes over their entire lifetime and therefore enhance the sensitivity of conventional CLS by a factor of 40-700 (see chapter 3.4.2), the concept of a Multi Ion Reflection Apparatus for Collinear Laser Spectroscopy of radionuclides (MIRACLS) has been introduced and is pursued since January 2017. A schematic overview of the concept of MIRACLS can be seen in figure 3.8. A bunched ion beam will be trapped in a MR-ToF device in which the ion bunch and the laser can interact during each revolution. The emitted fluorescence photons will be detected in the ODR by PMTs positioned in the middle of the drift tube of the MR-ToF device. At MIRACLS the observation time will thus be extended and only limited by the half-life of the ions or by the maximal trapping time while maintaining the high resolution of traditional CLS. Hence, the novel MIRACLS' approach will allow to access nuclides with low production yields for the very first time with CLS. It is particularly well suited for closed two-level systems, where the ions directly decay back from the excited to the initial ionic state without populating any other metastable fine structure states or hyperfine structure states. The first science cases of MIRACLS can be found in table 3.2 together with their production yields at ISOLDE.

Table 3.2: production yields at ISOLDE for the first science cases of MIRACLS

isotope	production yield at ISOLDE
^{20}Mg	50 ions/s (at TRIUMF/Canada [31])
$^{21-33}$Mg	>1000 ions/μC [38] (already measured at COLLAPS)
^{34}Mg	140 ions/μC [38]
$^{>34}$Mg	(*)
$^{96-97}$Cd	(*)
^{98}Cd	10 ions/μC [38]
^{99}Cd	450 ions/μC [38]
$^{100-130}$Cd	>1000 ions/μC [38] (already measured at COLLAPS)
^{131}Cd	(*)
^{132}Cd	(*)
(*)	A planned upgrade of the ISOLDE proton driver will lead to higher production yields and more exotic radionuclides will become accessible [84].

Like conventional CLS, MIRACLS aims to work with ion beam kinetic energies of more than 30 keV to minimize the Doppler broadening such that the spectral resolution approaches the natural linewidth. However, all MR-ToF devices that exist so far have typical ion beam kinetic energies of a few keV and mirror potentials of less than 8 kV [2, 45, 65, 66, 77, 88, 90, 93]. Therefore a completely new MR-ToF device with mirror potentials of up to 60 kV has to be built. The 30-keV MR-ToF device will be discussed in chapter 5 in more detail.

In addition to the 30-keV MR-ToF device, also a new Paul trap has to be envisioned. CLS requires to have an energy spread lower than 1 eV (1 standard deviation σ) such that the Doppler broadening approaches the natural linewidth. Moreover, for the background reduction of stray light in the PMTs (see chapter 2.3) also a small time duration of the ion bunch at the time focus is important. For MIRACLS the ion bunch has at least to fit into one half of the central drift tube (with a length of 69 cm). Assuming a kinetic energy of the ions of 30 keV, the velocity of the ^{24}Mg ions is 491 mm/μs and the time duration of the pulse at the time focus therefore has to be smaller than 0.7 μs. Assuming a Gaussian distribution the rms time duration of the pulse at the time focus is hence smaller than 0.23 μs. It follows that the longitudinal rms emittance $\epsilon_{\mathrm{rms,long}}$ has to be smaller than 0.23 μs eV. This requirement on the longitudinal emittance needed for MIRACLS is hence lower than the emittance of ISCOOL, which rms emittance is estimated to be around 2.5 μs eV (see chapter 3.2.3). Therefore a completely new Paul trap operating at cryogenic temperatures will be built for MIRACLS to obtain an excellent time focus and low energy spread (compare equation 3.17).

3.4.2 Improvement Factor in the Sensitivity at MIRACLS in Comparison to COLLAPS

In the following discussion, the CLS signal height (i.e. the number of detected fluorescence photons) for one single revolution in the MR-ToF device is expressed by s and the background by b. The signal-over-noise ratio s/n for one single revolution is hence $s/\sqrt{b}$ if Poisson statistics is assumed. Due to the fact that the ion bunch is passing the laser beam multiple times in a MR-ToF device, the signal for all revolutions S and background for all revolutions B increase both linearly with the number of

revolutions r in the MR-ToF device. Therefore the signal-over-noise ratio for all the revolutions in the MR-ToF device S/N is given by

$$\frac{S}{N} = \frac{S}{\sqrt{B}} = \frac{rs}{\sqrt{rb}} = \sqrt{r}\frac{s}{\sqrt{b}} = \sqrt{r}\frac{s}{n}. \tag{3.27}$$

For traditional CLS as done for instance at COLLAPS the signal-over-noise ratio s/n is the same as for one revolution in the MR-ToF device. Therefore the improvement factor in the sensitivity at MIRACLS in comparison to COLLAPS is given by $\sqrt{r}$. The number of revolutions in the MR-ToF device can be calculated by the ratio of the trapping time t_{trap} and the time for one revolution t_1, such that $r = t_{\mathrm{trap}}/t_1$.

However, the ions undergo a radioactive decay with a half-life of $T_{1/2}$ in the MR-ToF device, which leads to a reduction of the improvement factor. The signal for all the revolutions S can be calculated by

$$S \approx \sum_{i=0}^{r} \epsilon N_0 R \exp\left(-i\frac{\ln 2}{T_{1/2}}t_1\right)\Delta t_0, \tag{3.28}$$

where ϵ is the detection efficiency of the ODR, N_0 the number of all initially trapped ions of interest, R the fluorescence photon emission rate, and Δt_0 the time interval where the ions are in the ODR. For the deviation of this equation it is assumed that $\Delta t_0 \ll T_{1/2}$. This assumption is reasonable because the half-life of the ions is at least in the order of some milliseconds whereas Δt_0 is in the order of some microseconds. For simplicity, we assume idealised square-well-like electrostatic mirrors on which the ions are reflected without change in their absolute velocity ($v \to -v$) and hence $\Delta t_0 = t_1$ can be considered. Note that the laser beam is actually only in resonance for one direction of the ions. Following those assumptions, the signal for all revolutions S follows,

$$\begin{aligned} S &\approx \int_0^{t_{\mathrm{trap}}} \epsilon N_0 R \exp\left(-\frac{\ln 2}{T_{1/2}}t'\right)dt' = \\ &= \epsilon N_0 R \frac{T_{1/2}}{ln2}\left[1 - \exp\left(-\frac{\ln 2}{T_{1/2}}t_{\mathrm{trap}}\right)\right], \end{aligned} \tag{3.29}$$

where it holds that $r\Delta t_0 = t_{\mathrm{trap}}$.
The background for all the revolutions B follows as

$$B = \sum_{i=0}^{r} B_0 \Delta t_0 = r B_0 \Delta t_0 = B_0 t_{\mathrm{trap}}, \tag{3.30}$$

where B_0 is the background rate due to PMT dark counts and the detected stray light. Following the same assumption as above, the background for one single revolution is $b = B_0 t_1$. The signal-over-noise ratio for all revolutions therefore is

$$S/N \approx \frac{\epsilon N_0 R \frac{T_{1/2}}{ln2}\left[1 - \exp\left(-\frac{\ln 2}{T_{1/2}}t_{\mathrm{trap}}\right)\right]}{\sqrt{B_0\ t_{\mathrm{trap}}}} \tag{3.31}$$

and the signal-over-noise ratio for one revolution is

$$s/n \approx \frac{\epsilon N_0 R \Delta t_0}{\sqrt{B_0 t_1}} = \frac{\epsilon N_0 R \sqrt{t_1}}{\sqrt{B_0}}, \tag{3.32}$$

what leads to an improvement factor of

$$\frac{S/N}{s/n} \approx \frac{1}{\sqrt{t_1 t_{\mathrm{trap}}}} \frac{T_{1/2}}{ln2} \left[1 - \exp\left(-\frac{\ln 2}{T_{1/2}} t_{\mathrm{trap}}\right)\right]. \tag{3.33}$$

The Limes for $T_{1/2} \to \infty$ of the improvement factor is $\sqrt{r}$, what is indeed the improvement factor without taking radioactive decay into account.
The optimal trapping time t_{trap} can be calculated by solving

$$\frac{\partial S/N}{\partial t_{\mathrm{trap}}} = 0 \tag{3.34}$$

numerically which yields $t_{\mathrm{trap}} = 1.81265\ T_{1/2}$.

Approximate revolution times t_1 for ions in a realistic 30-keV MR-ToF device of $\sim$ 1.2 m length can be estimated in simulations (see more details in chapter 5). Figure 3.9 displays the results of such simulations of t_1 for different mass numbers.
The improvement factor in the sensitivity at MIRACLS in comparison to traditional CLS experiments calculated by using equation 3.33 with $t_{\mathrm{trap}} = 1.81265\ T_{1/2}$ as a function of the nuclides' half-life $T_{1/2}$ and the mass number A is shown in figure 3.10. The improvement factor ranges from 40 to 700 for the first science cases of MIRACLS. At ISOLDE, bunches of high-energy protons hit the production target typically every 1.2 s. Hence, in practice, the maximal trapping time in the MR-ToF device will typically be of similar order.
Additionally to the results presented above, the improvement factor will be increased by a factor of 1.5 because MIRACLS will use three rows of PMTs whereas COLLAPS uses two. Moreover, a shorter time spread of the ion bunch at MIRACLS compared to COLLAPS can increase the improvement factor by a factor of up to 5 [50]. However, the ion-laser overlap might be slightly worse at MIRACLS compared to COLLAPS or ions might get lost in the MR-ToF device after some revolutions, what can lead to a slight reduction of the improvement factor.

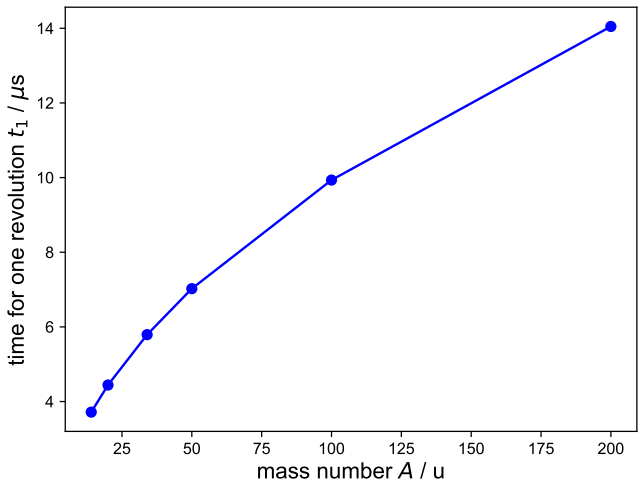

Figure 3.9: Simulated revolution times t_1 versus the mass number A of singly-positively-charged ions stored in the 30-keV MR-ToF device of $\sim$ 1.2 m length.

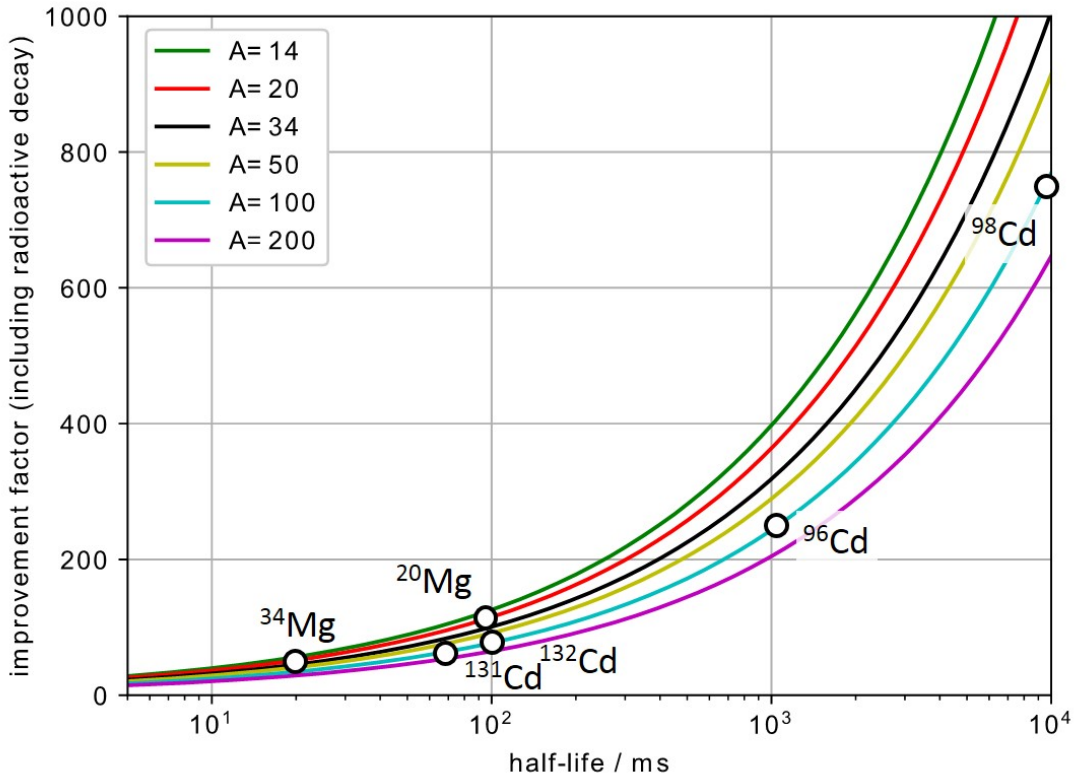

Figure 3.10: Improvement factor in experimental sensitivity at MIRACLS in comparison to traditional CLS experiments as a function of the nuclides' half-life $T_{1/2}$ and the mass number A. The first science cases for MIRACLS are marked with circles. The half-lives for the respective nuclides are taken from [13].

Chapter 4

MIRACLS' Proof-Of-Principle Experiment

4.1 Motivation

The goal of the proof-of-principle (PoP) experiment is to demonstrate the functionality of CLS within a low-energy MR-ToF device from the University of Greifswald [44, 71, 72], which has been modified for the purpose of CLS. Here, the experiment is performed with ion-beam kinetic energies of about 1.5 keV, whereas the future MIRACLS' MR-ToF apparatus will operate at 30 keV in order to minimise the Doppler broadening. Moreover, the PoP experiment uses a stable beam of Magnesium ions that is produced in an offline ion source.

The first part of this chapter deals with the modifications on the setup that are necessary to perform the PoP experiment. These include building up a laser system, minimization of the laser stray light into the PMT, increasing the Magnesium ion yield, and optimizing the performance of the MR-ToF device in CLS mode. A general overview over all the components of the PoP setup will be given.

The next part of this chapter describes the first experimental results for CLS within a MR-ToF device. The observed spectroscopic line shapes and the obtained isotope shift between $^{24}Mg^{+}$ and $^{26}Mg^{+}$ are discussed.

The last part describes the simulations of the ions' trajectories. Firstly all the potentials along the beam line are simulated to find suitable potentials for the transfer of the ions from the Paul trap into the MR-ToF device. Secondly, different mirror potentials are tested to find an optimal combination of mirror potentials for the MR-ToF device in CLS mode. Thirdly, the results of the simulations are compared to the experimental results to validate the chosen simulation approach, that will be applied to the 30-keV MR-ToF device in chapter 5.

Some parts of this chapter will be published in „F. M. Maier et al. Simulations of a Proof-of-Principle Experiment for Collinear Laser Spectroscopy with a Multi-Reflection Time-of-Flight Device. *Submitted to Hyperfine Interactions*, January 2019."

4.2 Proof-of-Principle Setup

4.2.1 General Overview

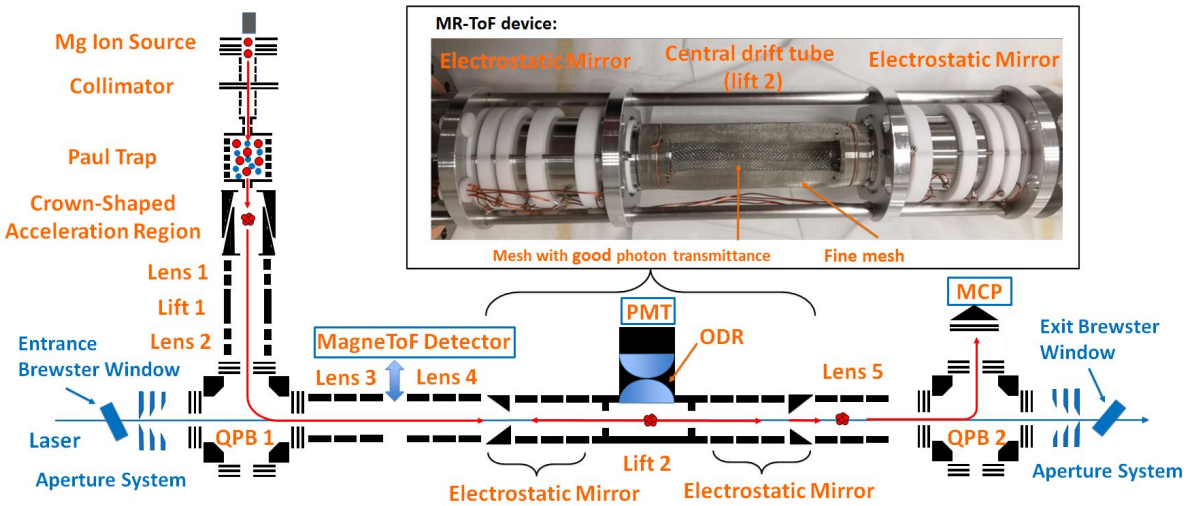

Figure 4.1: Schematic drawing of the modified MIRACLS' PoP setup. An offline ion source produces a continuous Mg^+ ion beam which is injected into a buffer-gas-filled Paul trap for cooling, accumulation and bunching. After acceleration the ions are stored in the MR-ToF device. During each revolution the laser beam can interact with the ion bunch. Fluorescence photons are detected by a PMT in the ODR. Insert: Photo of the MR-ToF device. See text for details.

The proof-of-principle (PoP) experiment is carried out in an existing, low-energy MR-ToF device from the University of Greifswald, that was designed for mass measurements of clusters as well as for the investigation of space-charge effects [44, 72, 71]. However, for performing CLS, optical access to the MR-ToF device is required to guide a laser beam into the apparatus, which can resonantly excite the stored ions. Moreover, an ODR has to be included above the central drift tube of the MR-ToF device for the detection of the fluorescence photons emitted by laser-excited ions (see below). For efficient CLS it is important to have a good signal-to-noise ratio in the detected photon counts. Hence, modifications on the entire beam line are necessitated to reduce the laser-stray light into the PMT and to increase the ion yield in the MR-ToF device. A detailed overview over all the modifications on the beam line that have been carried out during the work for this thesis is given in the appendix A.1.

A schematic drawing of the modified MIRACLS' PoP setup is shown in figure 4.1. In this section, a short explanation over the entire PoP setup will be given, whereas a more detailed explanation of the individual components will follow in the subsequent chapters. An offline electron-impact-ionization ion source as described in [59] is modified to produce a continuous beam of stable $^{24-26}Mg^+$ ions. After its formation, the continuous 250-eV ion beam is injected into a compact, linear Paul trap [71] floated to ∼224 V, where the ions are accumulated and cooled through collisions with helium buffer-gas atoms. The ions are ejected from the trap as well-defined ion bunches. A crown-shaped electrode accelerates these ion bunches towards a pulsed drift tube (lift 1), which is switched from ~ -2080 V to ground potential when the ions are in its center. Thus, the ions are lifted to a kinetic energy of ~ 2.3 keV with respect to the subsequent, grounded beam line. An electrostatic quadrupole bender (QPB 1) bends the ion beam onto the MR-ToF axis. A retractable MagneToF detector (14925, ETP Ion Detect, Ermington,

Australia) is installed in front of the MR-ToF device for beam diagnostics. For capture and ejection of the ions into and from the MR-ToF device, the technique of in-trap-lift switching is exploited [92], see chapter 3.3.2.2. Following its release from the trap, the ion bunch is bent by another QPB (QPB 2) and detected by a multi-channel-plate (MCP) detector. Both QPBs facilitate the overlap between the ion and laser beam. The laser beam enters and exits the setup through quartz windows installed at the Brewster angles to minimize reflections. Aperture systems installed next to the Brewster windows and a stray light shield around the ODR are used to minimize background photons (see chapter 4.2.7.3). Above the central drift tube (CDT) of the MR-ToF device, an optical lens system and a PMT (modified from [43]) is installed to focus and detect fluorescence photons emitted by laser-excited ions [76].

4.2.2 Production of Ions and Injection into the Paul Trap

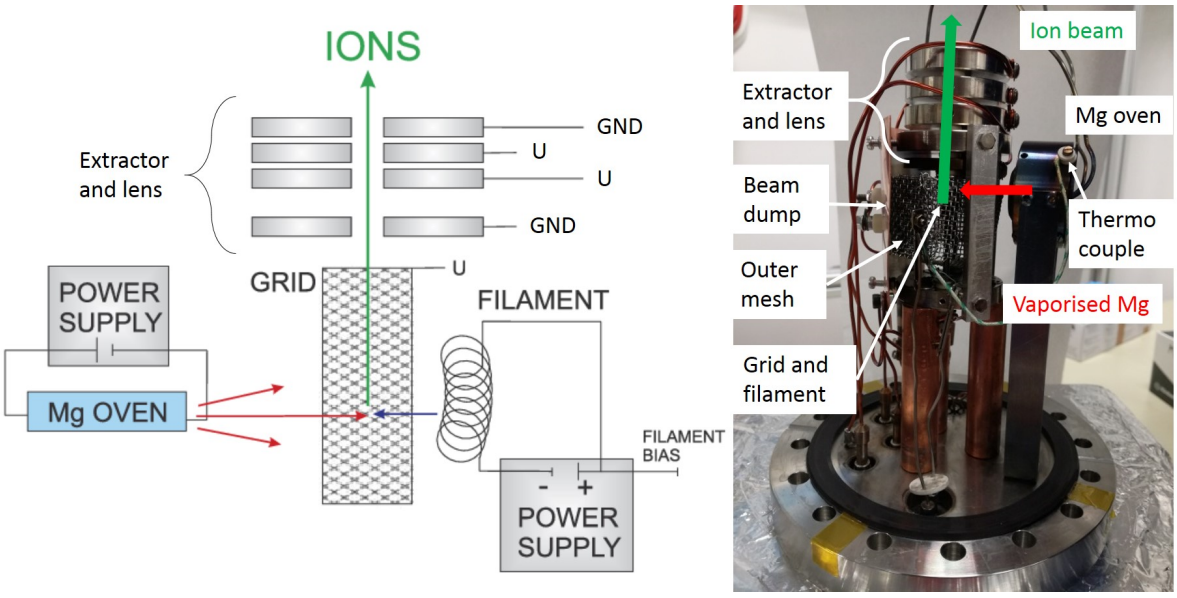

Figure 4.2: Schematics and photo of the MIRACLS' PoP ion source. Left figure modified from [59].

For the PoP experiment an offline ion source is used which produces a continuous beam of stable $^{24-26}Mg^{+}$ ions with the natural abundances of 78.99, 10.00, and 11.01% respectively [56]. The design of the compact ion source [59] is adapted and improved for the needs of the PoP setup [5]. A schematic and a photo of the ion source are shown in figure 4.2. Due to the fact that Magnesium is at room temperature not already in the gaseous state, it has to be vaporised by an oven that heats the Magnesium above its vaporisation temperature. The Magnesium atoms are ionized by the impact of electrons that are emitted from a hot filament. An extraction electrode is used to obtain a field gradient at the ionization region and a continuous beam of Magnesium ions is formed, that is focused and translated in horizontal and vertical direction by an einzel lens and steerer electrodes located between the ion source and a collimator (see figure 4.1). This collimator consists of two plates with a hole of a diameter of 10 mm. It is used to separate the vacuum volumes of the ion source and the MR-ToF device and hinders contaminating residual-gas particles produced in the hot environment of the ion source to enter the Paul trap region. A picture of the einzel lens and the collimator can be found in figure A.4. After its formation, the continuous ion beam is injected with the help of the injection optics consisting of a lens and a vertical steerer through the 4 mm hole of the Paul trap endcap (EI) into the linear Paul trap floated to ∼224 V.

The injection optics and the Paul trap are depicted on the left side of figure 4.3. The potential of the upper electrode of the steerer of the injection optics can be switched between the blocking voltage of ~ 400 V and ground potential by a fast high-voltage switch. If the blocking voltage is applied the ions are deflected and can not be injected into the Paul trap. The time interval where no blocking voltage is applied is called loading time. By changing this time interval one can control the number of ions injected into the Paul trap.

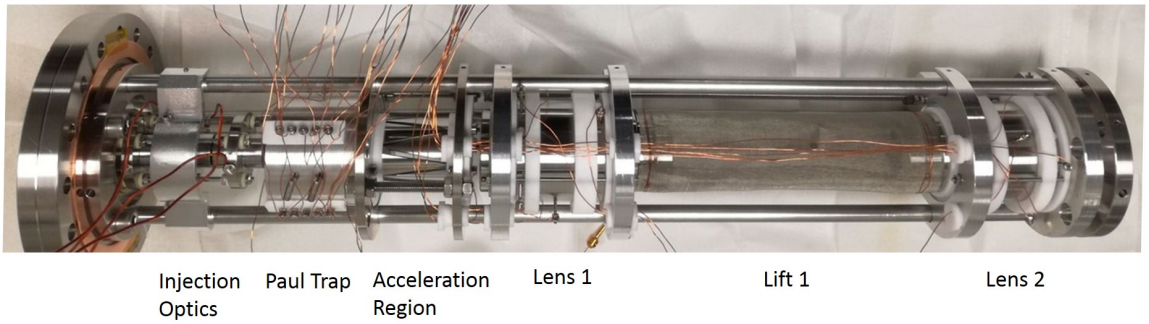

Figure 4.3: Paul Trap and acceleration region: The ions pass through this section from left to right: With the help of the injection optics the continuous ion beam is injected into the Paul trap, where the ions are accumulated and cooled through collisions with Helium buffer-gas atoms. The ion bunch then passes the acceleration and transport section, consisting of lens 1, lift 1 and lens 2, that will be explained in chapter 4.2.4.

4.2.3 Paul Trap

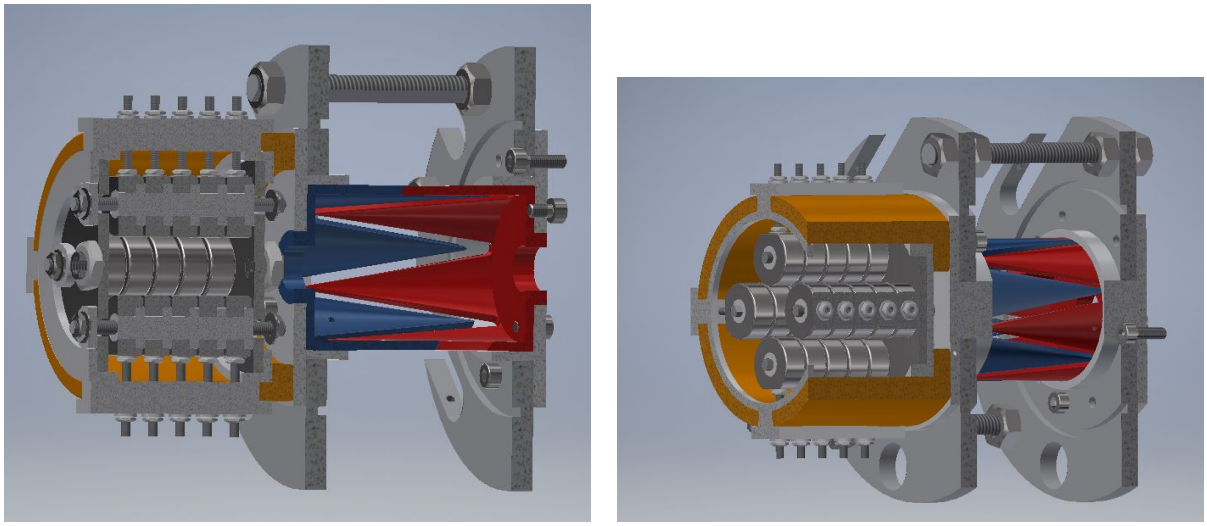

(a) (b)

Figure 4.4: 3D view of the Paul trap (orange and grey) and the acceleration zone (blue and red). Some parts are removed to show the interior. The design of the Paul trap in Autodesk Inventor was done by Robert Wolf [71].

A model of the linear Paul trap in the PoP setup is depicted in figure 4.4. The Paul trap consists of four segmented rods that are coupled pairwise. A radial confinement of the ions is achieved by applying an oscillating potential between the adjacent rods. Each rod consists of five segments to form the axial trapping potential. A schematic view of the electrical circuit is shown in figure A.7. Every segment has its own LC-resonance circuit to create the necessary RF amplitudes and every segment is biased to the corresponding DC voltage. A frequency generator produces a sinusoidal AC voltage with an amplitude of $\sim$ 10 V and a frequency of 1.997000(3) MHz. The sinusoidal signal is amplified by a frequency amplifier. Hence, the sinusoidal RF signal applied to the four rods has a measured amplitude V of 140(5) V. The Paul trap is enclosed in a cylinder with two endcap electrodes. This cylinder is filled with Helium atoms which are supplied through a small tube coupled to the middle of the cylinder. The ions are thermalized through collisions with the Helium atoms during the cooling time and trapped axially between segments 4 and 5 according to the simulations described in chapter 4.4. For ejection of the ions from the trap the endcap EA is switched from EApos ($\sim$ 265 V) to EAneg (normal operation: $\sim$ 169 V). This creates a potential ramp and the ions are extracted as an ion bunch with low energy spread. The bias voltages applied to the Paul trap and neighbouring electrodes can be found in table A.1. The resulting potential distribution along the axis of the Paul trap is shown in figure 4.26 once for trapping (blue curve) and once for ejection (red curve).

The loading time of the Paul trap is typically up to 10 ms for operation in CLS mode. A loading time longer than 10 ms is not leading to a higher signal amplitude on the ion detectors indicating that the space-charge limit of the Paul trap is reached. For cooling times higher than 15 ms notable ion losses in the Paul trap are observed which are likely due to charge exchange because of impurities in the Helium gas. The Helium pressure in the enclosed Paul trap cannot be measured directly. However, since the Helium atoms can leave the Paul trap through the holes of the endcaps relative changes in the Helium gas pressure can be estimated by a vacuum gauge outside the cylinder hosting the Paul trap. A pressure

of $\sim 2.5 \cdot 10^{-5}$ mbar measured of this gauge leads to the highest ion signal at the MCP. The pressure readings are normalized to N_2 as residual gas and the used vacuum gauges are not calibrated to Helium gas. Therefore the pressure values throughout this thesis are only given to illustrate the relative changes in the vacuum. It is assumed that the Helium pressure in the cylinder hosting the Paul trap is in the order of 10^{-3} mbar.

4.2.4 Acceleration and Transport Region

After the ejection of the ions from the Paul trap the ions pass the double crown shaped acceleration region, that can be seen in figures 4.3 and 4.4. This kind of acceleration region is used to obtain a linear acceleration field (see figure 4.26(a)). To the 6 jags that are closer to the Paul trap a voltage of ~ 142 V is applied and to the 6 jags that are closer to lift 1 a voltage U_{lift1} of ~ -2080 V. The ions are accelerated to their final transfer kinetic energy, that is given in first approximation by the potential U_{seg5} of the Paul trap segment 5 and the potential U_{lift1}, $E \approx e(U_{\text{seg5}} - U_{\text{lift1}}) \approx 2304$ eV. The ions pass through the electrostatic einzel lens (lens 1) and enter the pulsed drift tube here called lift 1. Lift 1 consists of two electrodes that are connected with a cylindrical, conductive mesh. When the ions are in the middle of lift 1 the voltage of the lift tube is switched from ~ -2080 V to ground potential. Hence, the ions remain at their gained kinetic energy of ~ 2304 eV within the subsequent grounded beamline. The ions pass through another einzel lens (lens 2) before they are bend by the quadrupole bender QPB 1. Afterwards the ion beam is focused by lens 3 and lens 4 before the ions are injected into the MR-ToF device.
The PoP setup is simulated in SimIon (see chapter 4.4 and [48]) to find the potentials for an optimal ion injection into the MR-ToF device. Those simulated values are taken as starting parameters for the experiment and a further optimization of the electrode potentials is done experimentally. Additionally to the electrodes mentioned above there are steerer electrodes to move the ion beam in horizontal or vertical direction in order to correct small geometrical imperfections or misalignment. All electrodes in the PoP setup can be seen in figure A.7.

4.2.5 MR-ToF Device

The MR-ToF device (see insert of figure 4.1 and figure 4.5) consists of two opposing electrostatic ion mirrors positioned at either side of a central drift tube (CDT) or also called central lift tube (lift 2). Each electrostatic mirror is composed of four cylindrical electrodes of which the one closest to the CDT is biased to a negative potential for radial refocusing of the ions. The reflecting potential walls are realized by the three outer electrodes of each mirror. Given the sensitivity of the ions' trajectories to field distortions at their turn-around point, the outermost mirror electrode has a 12 mm diameter aperture at its outer end to shield the MR-ToF device from fringe fields of nearby electrodes (see figure 4.6). The mirror potentials used in the experiment and the lengths of the mirror electrodes can be found in table 4.1.
The CDT is made out of two electrodes and a connecting cylindrical, conductive mesh. Next to the ODR, the initial fine mesh is replaced by a mesh with higher transparency for an improved photon-detection efficiency. At both ends of the CDT, the inner diameter is reduced to 14 mm compared to 40 mm inside the mirrors and the center of the CDT in order to shield the drift region from penetrating electric fields, providing a large field-free region inside the CDT.

Table 4.1: Lengths and applied voltages of the MR-ToF device electrodes (ME1 is the mirror electrode closest to the central drift tube, ME4 is the outermost mirror electrode)

respective electrode	potential / V	electrode length / mm
ME1	-4814.0	26
ME2	1897.0	16
ME3	584.5	10
ME4	1706.3	22
central drift tube		212
in- and ejection:	665-1500	
trapping:	0	

During ejection, the ions' kinetic energy exceeds the mirror potentials and therefore the ions can enter the MR-ToF device. When the ions are in the middle of the CDT the in-trap lift is activated, i.e. its potential is switched from some positive value U_{lift2} (e.g. 825 V) to ground. The kinetic energy E of the ions in the middle of the CDT is in good approximation given by $E \approx e(U_{\text{seg5}} - U_{\text{lift1}} - U_{\text{lift2}}) \approx 1479$ eV and is smaller than the mirror potentials. Thus, the ions are trapped between the electrostatic mirrors (see chapter 3.3.2). For ion ejection the voltage U_{lift2} is applied again and the ions can leave the MR-ToF device (see chapter 3.3.2.2). The potential distribution along the MR-ToF axis for trapping and in- or ejection can be seen in figure 4.21. After ejection of the ions from the MR-ToF device the ion beam is focused by lens 5, bend by the QPB 2, and detected with the help of a MCP. Some ion distributions recorded at the MCP for single-ion counting with less than 10 ions/shot can be seen in figure 4.7. This figure illustrate the principle of a MR-ToF device. A longer flight path leads to an increased separation of the $^{24-26}Mg^{+}$ isotopes.

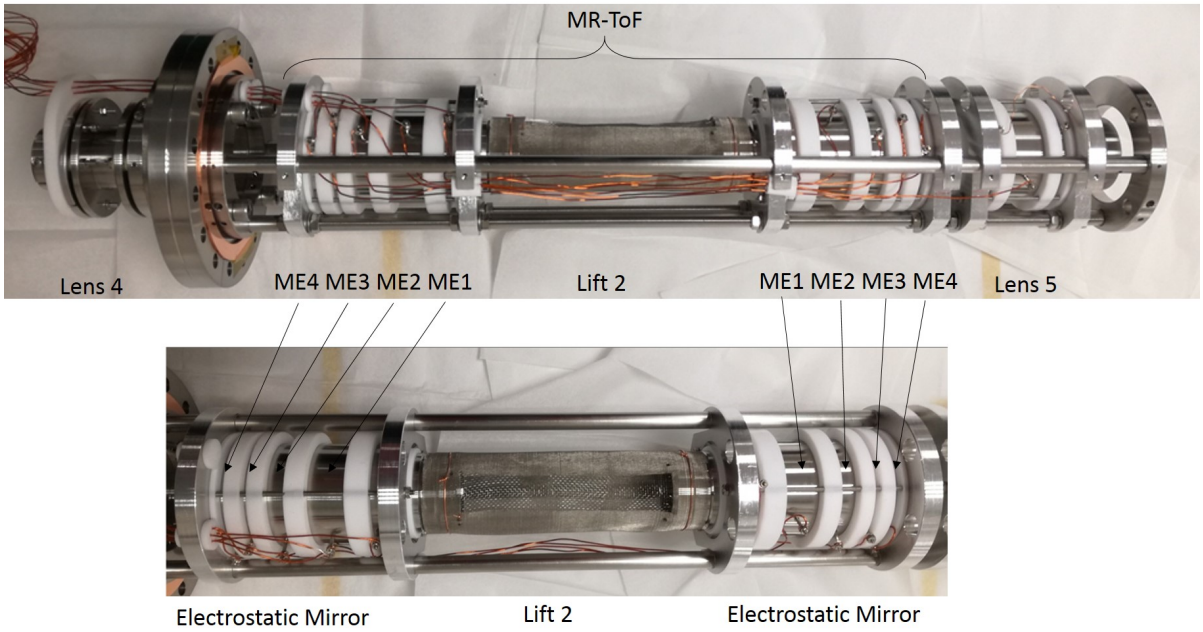

Figure 4.5: Photos of the MR-ToF device: Top: Side view of the lens 4, MR-ToF device and lens 5. Bottom: Top view of the MR-ToF device.

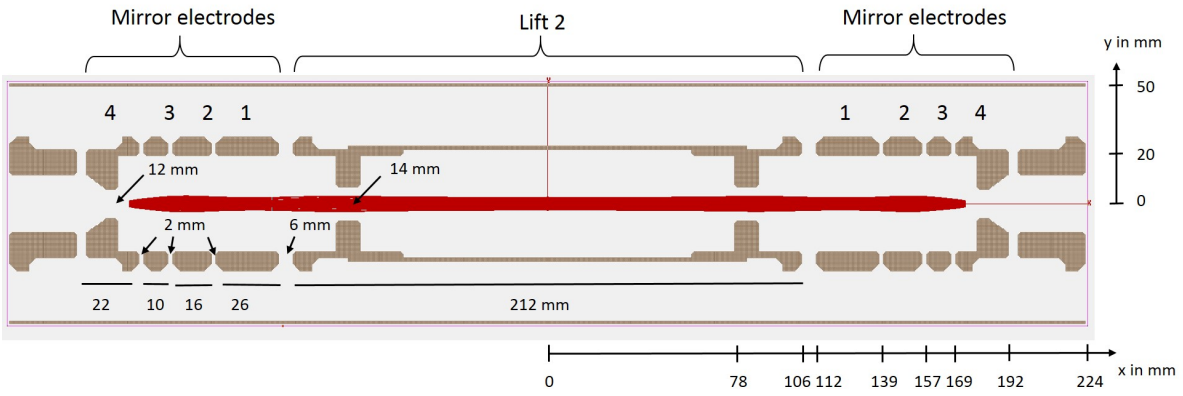

Figure 4.6: Cross section view of the MR-ToF device. The electrodes on the very left and right are added for the simulations in SimIon to minimize computational errors due to the not well-defined potentials at the end of the simulation region and these electrodes are hence not there in the experiment. Examples of simulated ions' trajectories are drawn in red.

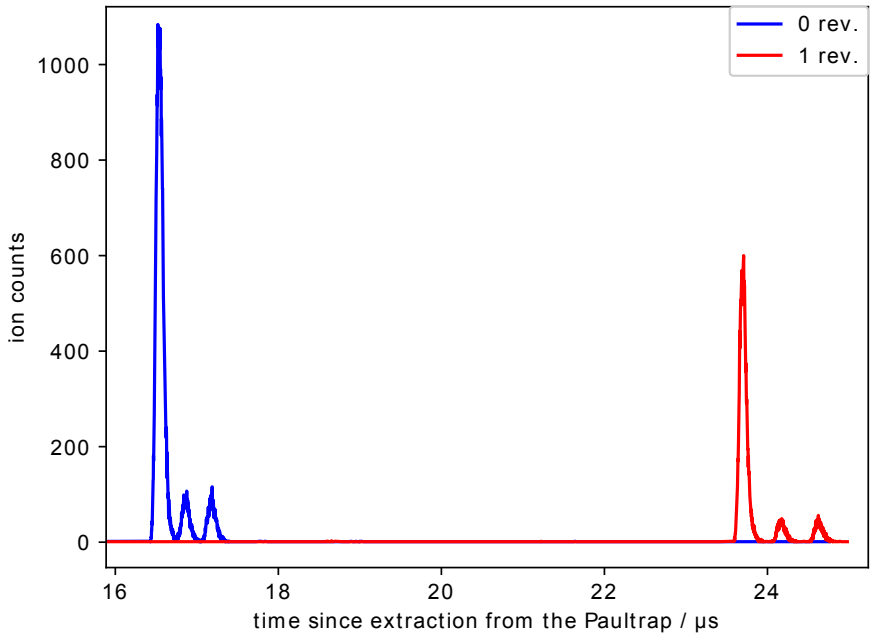

Figure 4.7: Ion counts on the MCP in single-ion counting mode versus the time-of-flight ToF since extraction from the Paul trap. The blue distribution is without trapping in the MR-ToF device and for the red distribution the trapping time is 7.16 μs such that the ions make one revolution in the MR-ToF device. The data is recorded with 10,000 ion shots and the potential applied to lift 2 is $\sim$ 795 V. The highest peak is formed by $^{24}Mg^{+}$ ions, the middle peak by $^{25}Mg^{+}$ ions and the right peak by $^{26}Mg^{+}$ ions, respectively. The integrated counts underneath the peaks reflect the different natural abundances of the three stable Magnesium isotopes, that are 78.99, 10.00 and 11.01% [56]. Due to different masses the isotopes of Magnesium need different times until they reach the MCP detector. The FWHM of the ToF peaks of $^{24}Mg^{+}$ for 0 and 1 revolutions are $\sim$ 98 and $\sim$ 88 ns.

4.2.6 Control System

The control of the PoP setup (data acquisition, timing sequence, communication with some power supplies) is integrated in the ClusterTrap-CS from the University of Greifswald [72]. A FPGA card (National Instruments) generates as a pulse-pattern generator the time-sequence of signals to control the fast HV switching for the electrode potentials (blocking voltage, endcap of the Paul trap, lift 1, and lift 2). The time pattern for a typical measurement cycle is shown in figure 4.8. After some waiting time the ions are injected into the Paul trap during the loading time where the blocking voltage is 0 V instead of $\sim$ 400 V (see chapter 4.2.2). After the cooling time the ions are ejected from the Paul trap by switching the endcap of the Paul trap EAneg from $\sim$ 265 to $\sim$ 169 V. The ions need some microseconds to travel from the Paul trap to the middle of lift 1. Once the ions reached the middle of the lift tube, lift 1 is switched from ~ -2080 V to ground potential. During some microseconds the ions travel from the middle of lift 1 to the middle of lift 2 and lift 2 is switched from e.g. 875 V to ground potential. After being trapped for a specific number of revolutions the ions are ejected from the MR-ToF device by switching of lift 2 from ground to e.g. 875 V. Finally, the measurement cycle is repeated after some waiting time. The waiting times are used to provide some time to (re)charge the capacitors which buffer the high voltage switches to ensure to provide stable potentials. The ejection of the ions is synchronized to a given phase of the RF potential of the Paul trap.
After the ions are ejected from the MR-ToF device they hit a MCP. The data acquisition for single-ion counting is either performed with a Multichannel Scaler (SRS 430) or with the ClusterTrap-CS. Alternatively the data acquisition can also be done with a commercial program that uses a 4-GHz Time-of-Flight Multiscaler (card P7887). The data acquisition for a larger number of ions per bunch is done with an oscilloscope. The data acquisition is either triggered on the ejection of the ions from the Paul trap or from the MR-ToF device.

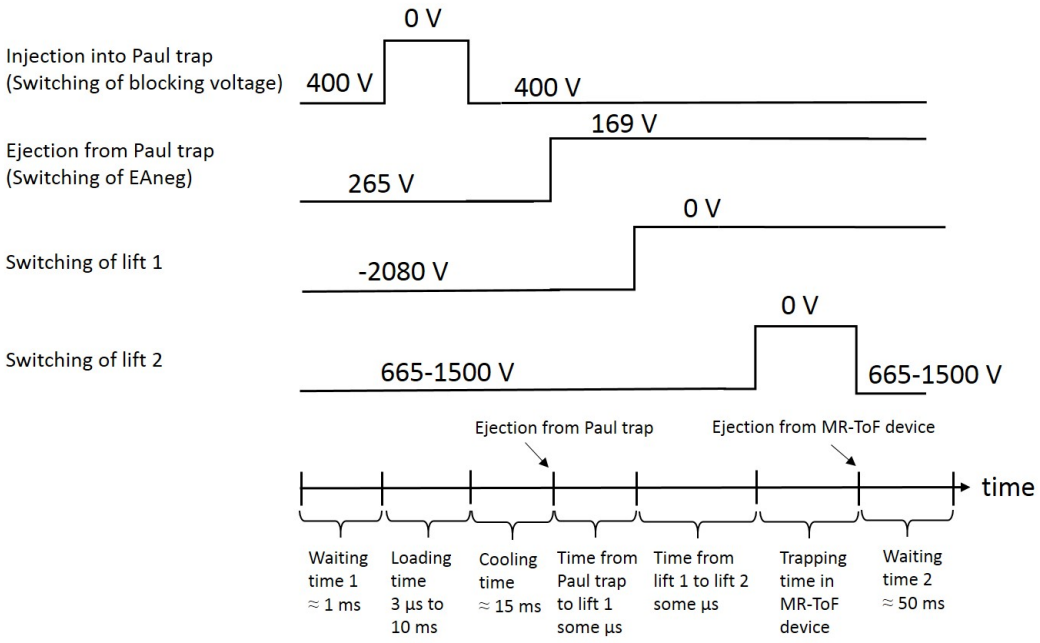

Figure 4.8: Time pattern for a typical measurement cycle.

4.2.7 Laser System in MIRACLS' PoP experiment

4.2.7.1 Setup

For the excitation of the stable Mg^+ ions in the D1 and D2 line a cw laser with a wavelength of around 280 nm and a scanning range of a few GHz is needed. The laser power that is used for CLS of Mg^+ ions is around 1 mW.
Due to space constraints and insufficient temperature stability in the MIRACLS' lab, a part of the laser setup is installed in a dedicated laser lab, that is around 25 m away from the PoP setup. The fundamental laser light of 560 nm is created by a dye laser and about 1 W is transported via a high-power optical fibre (LMA-15 Single-mode 15-μm core fiber) to the laser table in the MIRACLS' lab, where the light is frequency doubled to 280 nm.

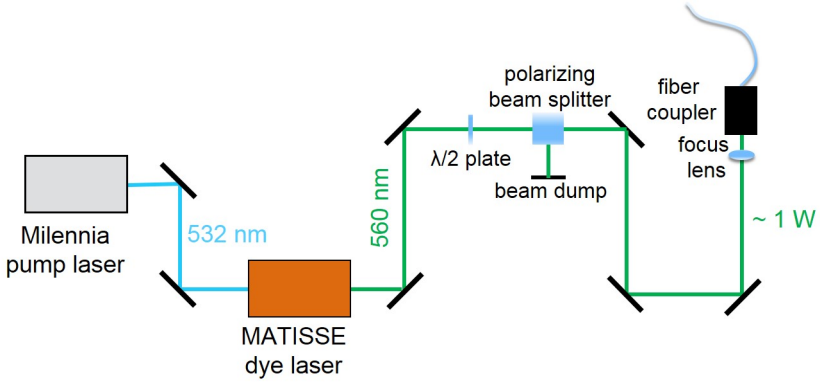

Figure 4.9: Laser setup in the dedicated laser lab. See text for details.

The laser setup in the dedicated laser lab can bee seen in figure 4.9. The laser light with a wavelength of around 560 nm is created by the actively stabilized dye ring laser *Matisse 2 DS* which is pumped by a cw diode-pumped solid-state laser (*Milennia eV*) with a wavelength of 532 nm and a power of up to 20 W (normal operation: 9-13 W). The dye laser system uses an external reference cavity and a fast piezo driven mirror to narrow the linewidth down to less than 250 kHz. Moreover, single frequency scanning without mode hopping is possible in a range of over 60 GHz [82].
The *Matisse 2 DS* laser is operated with the dye *Rhodamine 560* dissolved in ethylene glycol and has an output power of 0.5 to 1 W (depending on the dye pressure, the age of the dye, and the power of the pump laser). A rotatable $\lambda/2$ plate and a polarizing beam splitter provide an easy power regulation for fibre coupling. A 30 mm focusing lens and two high precision mirrors are used for proper coupling into the fibre. The theoretical transmission of the fibre over a distance of 25 m is 83%, under normal circumstances we experimentally achieve around 50-70%. Therefore the power in the MIRACLS' lab is around 250 to 700 mW, which is sufficient for a stable operation of the frequency doubler. The wavemeter (WSU-10 by HighFinesse) used to measure, control and stabilize the actual wavelength of the dye laser is regularly calibrated using a diode laser, that is locked to the hyperfine transition from the $5p\ ^2S_{1/2}$ state with $F = 2$ to the $5p\ ^2S_{3/2}$ state with $F = 3$ of ^{87}Rb at around 780 nm. The specifications of the wavemeter manufacturer state an accuracy of 10 MHz when calibrated by a well-known reference within 200 nm or an accuracy of 30 MHz if the well-known reference is more than 200 nm away, as it is here the case.

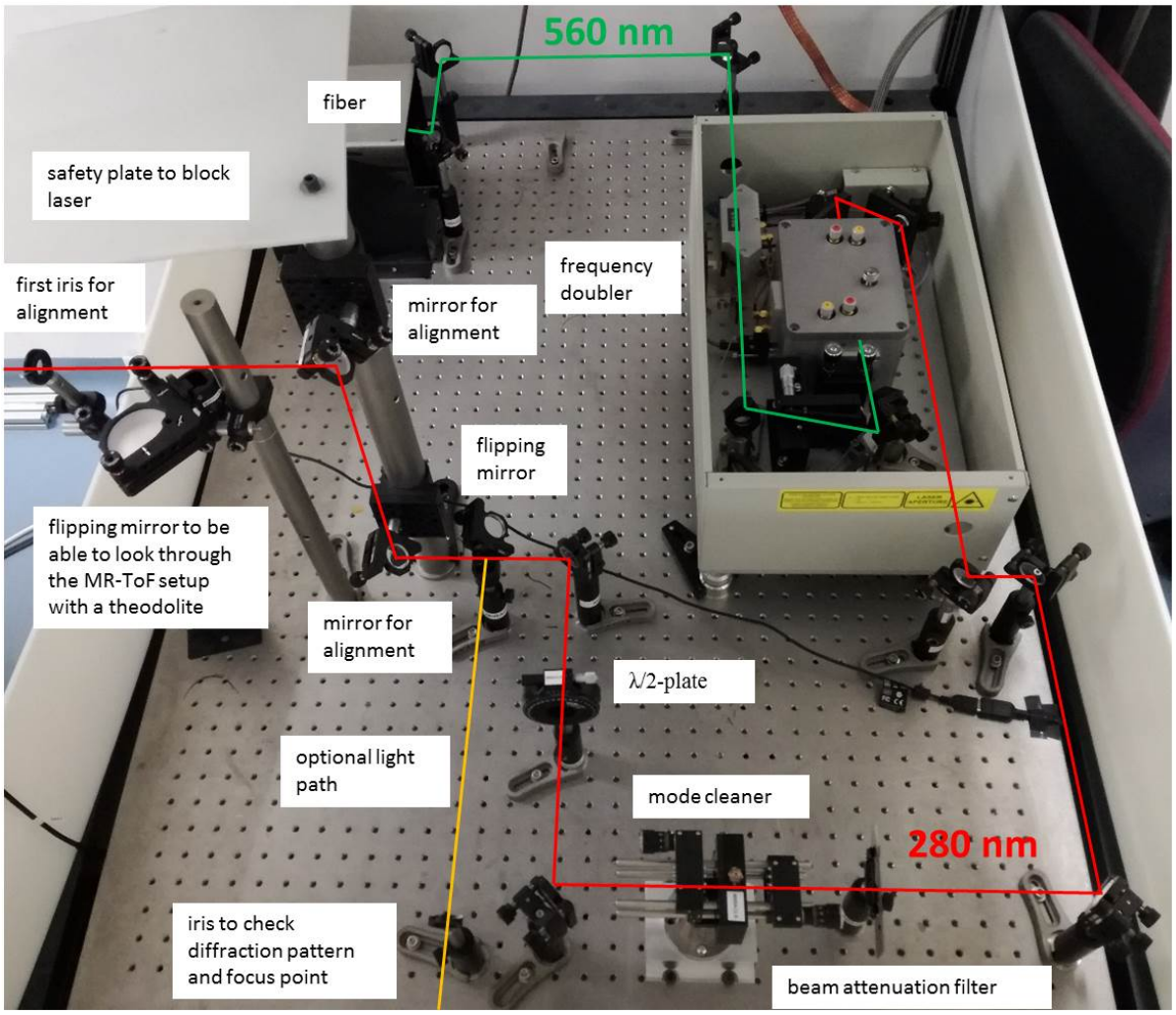

Figure 4.10: Laser Setup in the MIRACLS' lab. See text for details.

The laser setup after the fibre in the MIRACLS' lab can be seen in figure 4.10. The laser light first passes through a frequency doubler (Wavetrain2) to obtain the required wavelength of around 280 nm. The power after the frequency doubler is around 1-15 mW and can be further adjusted with the help of a beam attenuation filter. To produce a clean Gaussian beam profile, a spatial filter or also called mode cleaner [86] is used to remove the unwanted multiple-order energy peaks and spatially varying intensity noise. The spatial filter system consists of an aspheric lens, a pinhole and a collimating lens, that are built in a way that only the central maximum of the diffraction pattern can pass through the pinhole. The collimator and the aspheric lens are selected such that a laser beam with a diameter of 2.0(5) mm is obtained.

A $\lambda/2$-plate is used to rotate the polarisation such that the laser light reflections on the entrance Brewster window are minimized. The entrance Brewster window is shown in figure 4.11. The Brewster windows are made out of synthetic fused silica with a refraction index at 280 nm of 1.49416 [69]. Therefore the Brewster angle θ_B at 280 nm is 56.21 degree. The Brewster windows are cut with an angle of (90-θ_B)=33.8 degree between the MR-ToF axis and the Brewster window. Although the transmittance

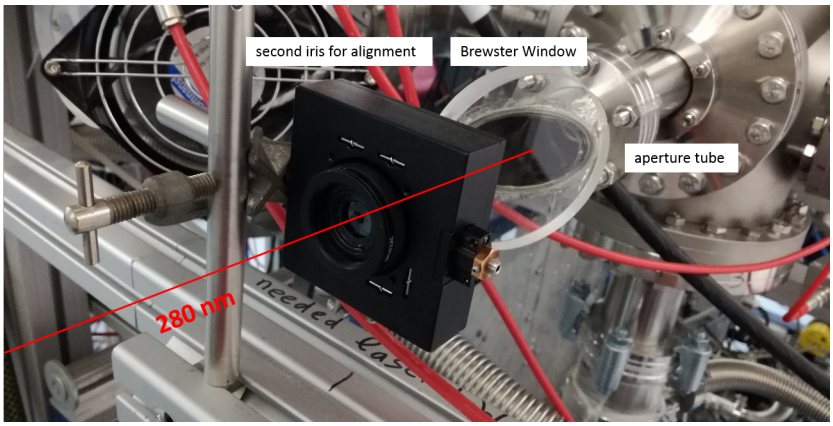

Figure 4.11: Laser setup in the MIRACLS' lab: second iris for alignment and entrance Brewster window

of the synthetic fused silica is specified as 90% [69] by the manufacturer, no power reduction is seen when passing the Brewster windows.

Two mirrors (labelled with mirrors for alignment in figure 4.10) are used to align the laser beam to the MR-ToF axis. The first and second iris for alignment in figures 4.10 and 4.11 are used for a rough alignment. For the precision alignment the second iris for alignment and a cross at the wall after the exit Brewster window are used. The alignment of this cross and the two iris to the MR-ToF axis is done with the help of a theodolite. The second iris for alignment is also used to cut away a distinct Airy pattern that is still present after the mode cleaner. Therefore the inner diameter of the second iris is set to typically ~ 2.5 mm.
With the help of a flipping mirror the laser path can be changed (marked with optional light path in figure 4.10). This optional light path is used to cross-check the laser spot size along a distance of 5 m.

4.2.7.2 Scanning of the Laser Frequency

In nearly all CLS beamlines the laser frequency is Doppler tuned by changing the velocity of the ions with the help of electrodes before the ODR while the laser frequency is kept at a constant value in the lab frame (see chapter 2.3). However, changing the kinetic energy of the ions in a MR-ToF device leads to uncontrollable ions' trajectories. Therefore, the laser frequency has to be scanned in the lab frame of the MIRACLS' experiment. The data acquisition program from the CRIS collaboration [15, 27, 73], that scans the laser frequency, has been adapted to the needs of the MIRACLS' PoP experiment [36]. The data acquisition program for MIRACLS is synchronized to the ejection of the ions from the Paul trap and records the photon counts over time for each laser frequency step.

4.2.7.3 Stray-Light Suppression

For efficient CLS a high signal-to-noise ratio is important. Therefore the background photon rate due to laser-stray light in the ODR has to be minimized. A stray-light shield is installed around the ODR to reduce the diffuse stray light from multiple scattering on the stainless steal walls of the vacuum vessel or electrodes. It consists of a cylinder and a plate with a slit mounted inside the cylinder. The slit (see upper right picture of figure 4.12) is designed in a way that all fluorescence photons emitted from an ion beam with a radius of 3 mm can still reach the lens while photons coming from other directions are

suppressed [51].
An aperture system as described in [48] is installed next to the Brewster windows and can be seen in figure 4.13. The aperture system cuts away the tails of the Gaussian shaped laser beam that otherwise would be scattered at the edges of the small holes in the setup.
The apertures as well as the inner side of the stray-light shield are painted with photon-absorbing colour (Tetenal Camera Spray). From the perspective of stray-light suppression it would be desirable to paint the entire setup. However, this would lead to degradation of the vacuum. Painting the very localised regions of apertures and stray-light shield in black where it matters most for stray-light suppression did not lead to any noticeable reduction of the vacuum quality (see figure A.8 in the appendix). After installing the stray-light shield and the aperture tubes the laser-induced background could be reduced by more than an order of magnitude.

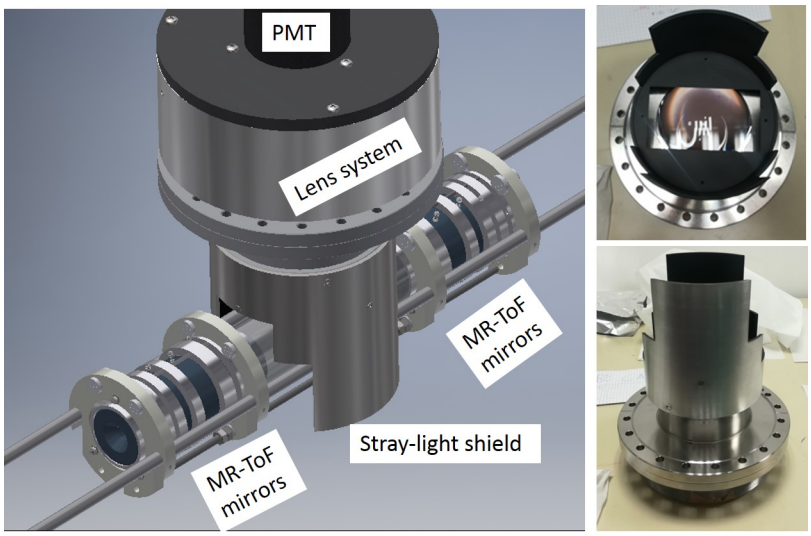

Figure 4.12: Stray-light shield installed around the ODR.

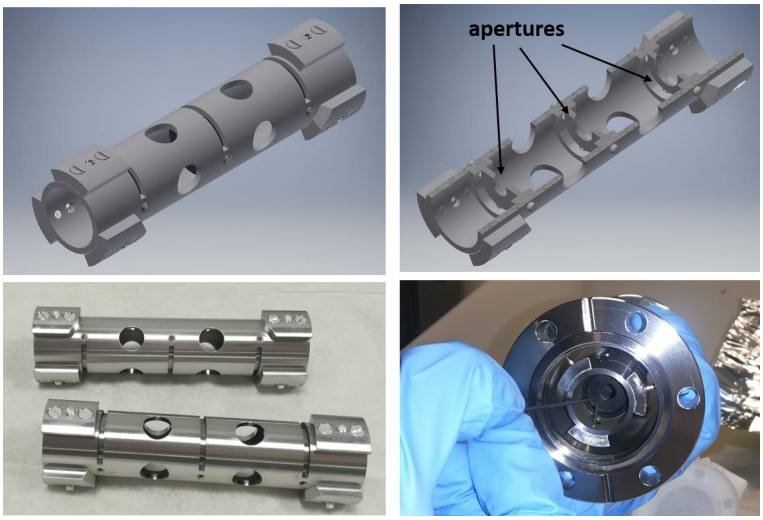

Figure 4.13: tube hosting the aperture system

4.3 Experimental Results

4.3.1 First Experimental Results

Both laser and ion beam are overlapped in the MR-ToF region and the laser frequency is scanned around the Doppler-shifted resonance frequency in the lab frame,

$$f_L = f\sqrt{\frac{1+\beta}{1-\beta}} \tag{4.1}$$

(compare equation 2.7), calculated based on the literature value for the resonance frequency in the ions' rest frame f [6] and the kinetic energy E of the ions, that is given in first approximation by the potentials U of segment 5, lift 1 and lift 2, $E \approx e(U_{\text{seg5}} - U_{\text{lift1}} - U_{\text{lift2}})$ (see chapter 3.3.2). Every time when the ions are within the ODR the laser excites the ions if the frequency of the laser matches the energy difference of the selected electronic transition and subsequently emitted fluorescence photons are detected in the ODR. For conventional CLS the ions are only once in the ODR, whereas in a MR-ToF device the ions pass the ODR multiple times. A distribution of the detected photon counts versus the time-of-flight ToF of the ions since extraction from the Paul trap at the resonance frequency f_L is shown in figure 4.14. Note, that for this ToF distribution the ions are ejected after 7 revolutions due to illustration purposes. However, we demonstrated CLS in a MR-ToF device for up to 1000 revolutions so far (see chapter 4.4.4.8). Some non-statistical fluctuations in the height of the peaks in photon counts for the first few tens of revolutions are commonly observed. In the shown ToF distribution for instance the peak corresponding to the fourth revolution is significantly smaller compared to the fluorescence photon peaks of the other revolutions. This might be due to some rearranging of the ion distribution in the MR-ToF device within the first few tens of revolutions (see also chapter 4.4.3) leading to a worse ion-laser overlap for specific revolution numbers.
By counting the number of photons as a function of the scanned laser frequency the (hyper)fine structure of the optical transition is obtained (see on the right of figure 4.15). If the laser frequency is far away from the resonance frequency f_L only background photons are detected by the PMT (1 in figure 4.15). Approaching the resonance frequency f_L the photon count rate is increasing because the first fluorescence photons are emitted and can hence be detected (2). For the resonance frequency the photon count rate measured at the PMT is the highest (3). For background reduction only photon counts are accepted when the ion bunch is within the ODR (see chapter 2.3) and a time gated spectrum (see figure 4.15) is obtained.

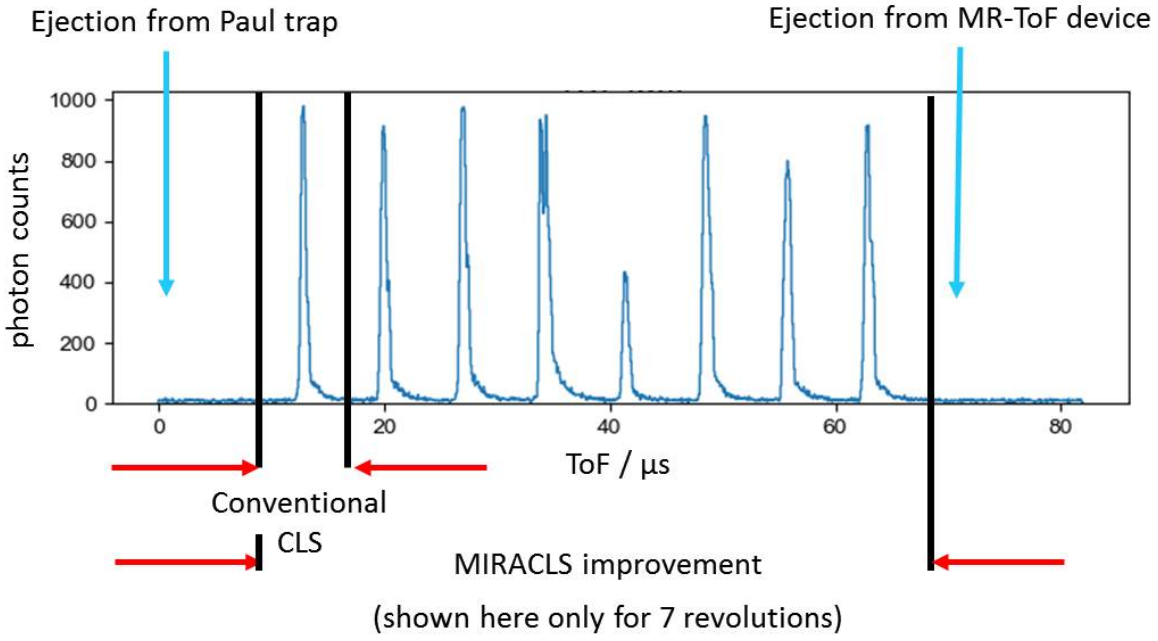

Figure 4.14: Distribution of the detected fluorescence photon counts versus the ToF of the ions since extraction from the Paul trap for the resonance frequency f_L. The data is recorded with 300 ion shots.

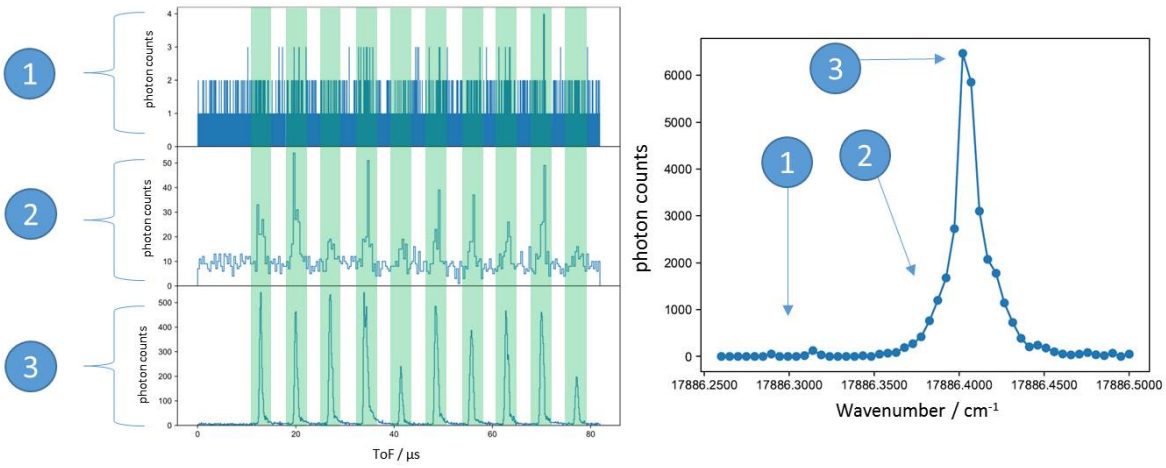

Figure 4.15: Left: Distribution of the detected fluorescence photon counts versus the ToF of the ions since extraction from the Paul trap for a laser wavenumber completely off the resonance wavenumber (1), close to the resonance wavenumber (2) and at the resonance wavenumber (3). Right: Obtained hyperfine spectra: By counting the number of all detected photons as a function of the scanned laser frequency a hyperfine spectrum is obtained. For background reduction only photon counts are accepted when the ion bunch is within the ODR. The time gates that are applied to the ToF distribution to obtain the shown hyperfine spectrum are shown in green. Note, that the fundamental wavenumber measured with the wavemeter (shown here) has to be multiplied by a factor of 2 due to the used frequency doubler. Furthermore the Doppler shift has to be taken into account to obtain the resonance frequency in the rest frame of the ions f. The data is recorded with 100 ion shots per frequency step.

4.3.2 Isotope Shifts

The isotope shift between $^{24}Mg^+$ and $^{26}Mg^+$ will in the following be exctracted from the measured D2 line to investigate systematic effects when performing CLS in a MR-ToF device. The laser frequency is scanned around the Doppler-shifted resonance frequencies in the lab frame f_L calculated from literature values in the ions' rest frame f for $^{24}Mg^+$ and $^{26}Mg^+$ ions, respectively. The photon counts detected by the PMT as a function of the ToF of the ions since extraction from the Paul trap can be seen in figure 4.16(a) for the first few revolutions, once for a laser frequency close to the resonance frequency of $^{24}Mg^+$ and once close to the resonance frequency of $^{26}Mg^+$. Due to the higher mass, $^{26}Mg^+$ ions need a slightly longer time for one revolution. Hence, the peaks in fluorescence-photon counts for the two different isotopes separate in time. The respective time gated hyperfine spectra can be seen in figure 4.16(b) for both isotopes. In figure 4.16(c) a zoom of the individual hyperfine spectra is shown, that are fitted with an asymmetric Pseudovoigt line shape to obtain the centroid frequency f_L in the lab frame.

In the following, two different approaches for the calculation of the isotope shifts are used. For the first one, the kinetic energy of the ions in the middle of the central drift tube is calculated via $E = e(U_{\text{seg5}} - U_{\text{lift1}} - U_{\text{lift2}})$ (see chapter 3.3.2), where all the potentials U are measured with a precision voltage divider. Once the kinetic energy is known, β (see equation 2.8) is calculated and the Doppler-shifted frequency f in the rest frame of the ions follows as (see equation 2.7)

$$f = f_L \sqrt{\frac{1-\beta}{1+\beta}}, \tag{4.2}$$

for each of the two isotopes. It is important to take the correct masses of the $^{24,26}Mg^+$ ions that can be calculated via

$$M_0 = M_{0,\text{atom}} + \frac{E_{\text{ionization}}}{c^2} - m_e, \tag{4.3}$$

where $M_{0,\text{atom}}$ is the mass of the ^{24,26}Mg atoms (23.985041697(14) u and 25.982592971(32) u), $E_{\text{ionization}} = 7.646236(4)$ eV is the ionization energy and m_e is the electron mass (all values taken from [62]). The isotopeshift follows then as the difference between the two centroid frequencies f in the rest frame of the ions. One disadvantage of this method is, that the kinetic energy of the ions in the middle of central drift tube has to be known quite precisely. To circumvent the knowledge of the precise kinetic energy of the ions a second method for the calculation of the isotopehifts is employed.
For this second approach, the resonance frequency f in the ions' rest frame for the $^{24}Mg^+$ ions is taken from the literature [6] and with the measured resonance frequency f_L of the $^{24}Mg^+$ ions in the lab frame β can be calculated according to equation 4.2. Once β is known the kinetic energy of the ions in the middle of the MR-ToF device follows according to equation equation 2.8 which should be the same for both $^{24}Mg^+$ and $^{26}Mg^+$ ions. This calculated kinetic energy is then used to extract the resonance frequency f of the $^{26}Mg^+$ ions in the rest frame of the ions from the measured $^{26}Mg^+$ resonance frequency f_L in the lab frame according to equation 4.2. The isotope shift follows from the difference of the determined resonance frequency f of the $^{26}Mg^+$ ions and the literature value f for the $^{24}Mg^+$ ions in the rest frame of the ions.

The isotope shifts obtained in both methods can be seen in figure 4.17. The literature value for the isotope shift between $^{24}Mg^+$ and $^{26}Mg^+$ ions in the D2 line is 3087.560(87) MHz [6] and is shown with a green line.

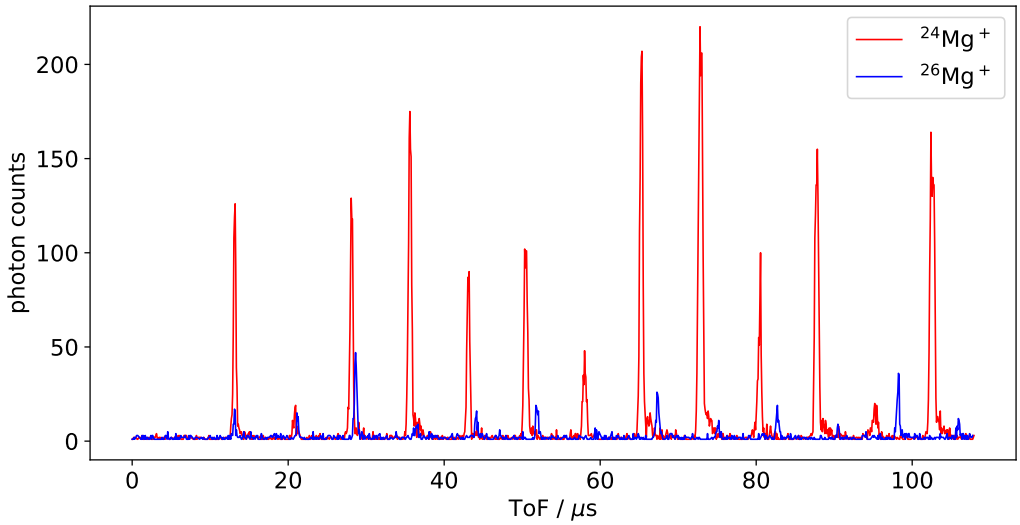

(a) Photon counts versus the ToF since extraction of the ions from the Paul trap for the resonance frequency f_L of $^{24}Mg^+$ and $^{26}Mg^+$, respectively. The data is recorded with 100 ion shots.

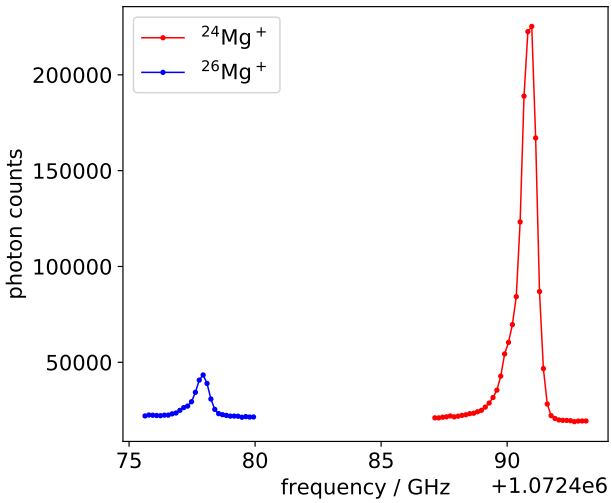

(b) time-gated hyperfine spectra of $^{24}Mg^+$ and $^{26}Mg^+$, respectively

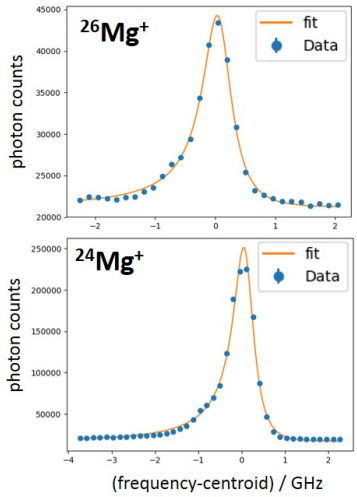

(c) asymmetric fit of the hyperfine spectra

Figure 4.16: Photon counts versus ToF of ions since extraction from Paul trap (a) and hyperfine spectra (b) and (c) recorded during measurement campaign 1. These data sets are used for the calculation of the isotope shift between $^{24}Mg^+$ and $^{26}Mg^+$ for the D2 line. The smaller peak heights of $^{26}Mg^+$ in respect to $^{24}Mg^+$ are due to the natural abundances of the stable Mg isotopes. The data is recorded with 100 ion shots per frequency step and the ions are trapped for 150 revolutions in the MR-ToF device. The potential applied to the in-trap lift tube is 655 V and the pressure in the MR-ToF region is around $2.5 \cdot 10^{-7}$ mbar. The gate width used to obtain the time-gated hyperfine spectra is chosen with 2 μs. For the fits of the lineshape in (c) an asymmetric Pseudovoigt lineshape is used to obtain the centroid frequency f_L for the calculation of the isotope shift.

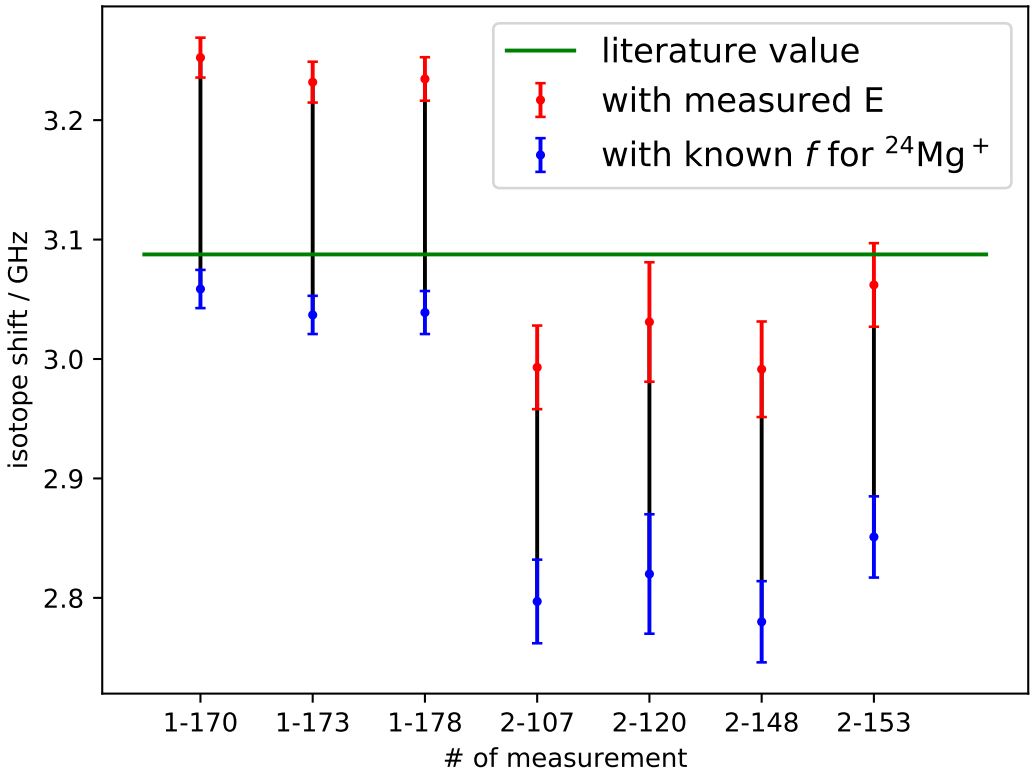

Figure 4.17: Isotope shifts for different measurement numbers and two different calculation methods. The first calculation method (red data points) is based on the kinetic energy of the ions in the MR-ToF device as extracted from the measured acceleration potentials. The second method (blue data points) takes the known literature value for the resonance frequency f of $^{24}Mg^+$ ions in the ions' rest frame [6] to calculate the resonance frequency f of the $^{26}Mg^+$ ions in the ions' rest frame. See text for details. The minimal systematic error follows as the difference of the two methods and is marked with a black line. The literature value [6] is shown in green. The measurement number, e.g. 1-170, stands for run number 170 in the measurement campaign 1.

The isotope shift measurements are carried out during two different measurement campaigns 1 and 2. For measurement campaign 1 the set value of lift 2 is 655 V and for measurement campaign 2 the set value of lift 2 is 750 V. The isotope shifts calculated by the two different methods differ by ~ 195 MHz for measurement campaign 1 and by ~ 211 MHz for measurement campaign 2.

The discrepancy between the two different methods and the disagreement with the literature value remains an open question. Moreover, while the individual results of each campaign appear statistical consistant, the results of the two campaigns do not agree well with each other. Hence, the following scenarios have been studied to investigate whether they can explain or even resolve these discrepancies.

Accuracy of Kinetic Energy of the Ions

The kinetic energy that is calculated with the second method is more than 35 eV different to the kinetic energy that is calculated based on the measured potentials U, $E = e(U_{\text{seg5}} - U_{\text{lift1}} - U_{\text{lift2}})$. This indicates that the ions' kinetic energy may not be known as accurately as assumed. Indeed, simulations of the ions in the proof-of-principle setup (see chapter 4.4) show that the ions' kinetic energy at the middle of the MR-ToF device is 1.94 eV higher than the calculated E based on the measured potentials (see energy difference between worst-case and complete scenario in table 4.2). This is due to the fact that the ions are not stored at the position of segment 5 in the Paul trap but between the segments 4 and 5. For the measurement number 2-153 in measurement campaign 2 this would mean an increase of the isotope shift from 3.055 to 3.064 GHz. This is smaller than our statistical error and hence does not explain the observed discrepancies. It appears unlikely that the kinetic energy is 35 eV different from our estimates based on the measurement of the relevant potentials in combination with field calculations in the PoP setup.

Accuracy of Set Laser Frequency

Another reason for the deviation of the isotope shift calculated by the two methods could be that the absolute laser frequencies recorded with the WSU-10 wavemeter by HighFinesse are not correct. To resolve the discrepancies between the two approaches for the calculation of the isotope shift, the absolute laser frequencies would need to be shifted by 2.5 GHz compared to the present readings of the wavemeter. The specifications of the wavemeter manufacturer state an accuracy of 10 MHz when calibrated by a well known reference within 200 nm or an accuracy of 30 MHz if the well known reference is more than 200 nm away, as it is the case for these measurements. In measurement campaign 2, the wavemeter is calibrated at an regular basis. No indications for large calibration drifts have been noticed. Hence, a wrong calibration of the wavemeter is also ruled out as a potential cause for the observed discrepancies.

Ions' Trajectories in the MR-ToF Device

For the calculation of the isotope shift it is assumed that the ions are flying parallel to the MR-ToF axis. However, simulations (see chapter 4.4) show that the average angle between MR-ToF axis and ion paths is 0.4 degree and the angular spread (1σ) is 0.4 degree. Therefore, the average Doppler-shifted frequency in the lab frame is shifted by around 12 MHz (see chapter 4.4) in respect to the one calculated for ions flying perfectly parallel to the laser-beam axis. Thus, this shift is too small to have any effect on the kinetic energy or the isotope shift at the observed magnitude.

Centroid Frequency as a Function of Revolution Number

The centroid frequency is fluctuating significantly during the first few revolutions (see e.g. figure 4.18(a)) until a constant value is reached. Due to ion losses in the MR-ToF device over revolution number (see e.g. figure 4.18(c)) the first few revolutions contribute more to the hyperfine spectrum. The centroid of the Doppler-shifted frequencies in the lab frame for taking all the revolutions into account is up to

0.03 GHz smaller than the one for only taking the last 100 revolutions into account. Thus, the isotope shifts for only the last 100 revolutions is about 0.02 GHz different from the one for all the revolutions for both methods for the calculation of the isotope shift. The seen discrepancies hence can still not be explained. However, a more detailed analysis of the centroid frequencies and the isotope shift versus revolution number might be helpful for a better understanding of the observed discrepancies. Moreover, it is planned to block the laser beam by means of a pockel cell during the first tens of revolutions to investigate the reasons for the fluctuations of the centroid. One reason for the unstable centroid over revolution number might be due to space-charge effects in the MR-ToF device, see below.

System Instabilities

Sizeable drifts over time have been observed in a few setup observables as for instance in the number of stored ions in the MR-ToF device. Another example is shown in figure 4.18(b). Although no changes are carried out between scans 173 and 179 (except of changing the frequency range for either recording $^{24}Mg^+$ or $^{26}Mg^+$ hyperfine spectra) and the measurement are done directly after each other, the centroid of scan 176 shows a different behaviour over revolution number than the two other scans for $^{26}Mg^+$, 174 and 179. For the isotope shift measurements presented in figure 4.17 only measurement runs are accepted where the centroid stays stable over revolution number when the first few revolutions are neglected (except of measurement number 2-153, see below). These 'system drifts' over time need to be identified and eliminated in a future work.

Space-Charge Effects

Space-charge effects due to the repulsive Coulomb interactions may effect the CLS centroid when large amount of ions are stored in the Paul trap and/or MR-ToF device. At MIRACLS' PoP setup the number of ions is controlled via the loading time of the Paul trap. A longer loading time of the Paul trap means that more ions are injected into the MR-ToF device. Indeed, the loading time of the Paul trap plays a role for the evolution of the centroid over revolution number (see figure 4.19). For measurement 2-153 the loading time of the Paul trap is three times higher than for the measurement 2-148. Although the exact relationship between large number of stored ions and CLS in a MR-ToF device is not yet understood, the Doppler-shifted centroid frequency over revolution number for measurement runs with long loading times consistently show a different behaviour than measurement runs with shorter ones (see figure 4.19). However, the isotope shift is within statistics the same as the other measurements during measurement campaign 2, hence, do not appear to be a major cause for the observed discrepancies. Nevertheless, the space-charge induced effects in Paul trap and/or MR-ToF device need to be systematically studied in future measurement campaigns.

Timing of HV Switching

In principle it could be possible that the $^{26}Mg^+$ ions are not exactly in the middle of the MR-ToF's central drift tube when the in-trap lift is activated. Hence, the $^{26}Mg^+$ ions obtain a different kinetic energy than the $^{24}Mg^+$ ions. Taking the resonance frequency f in the ions' rest frame for the $^{24}Mg^+$

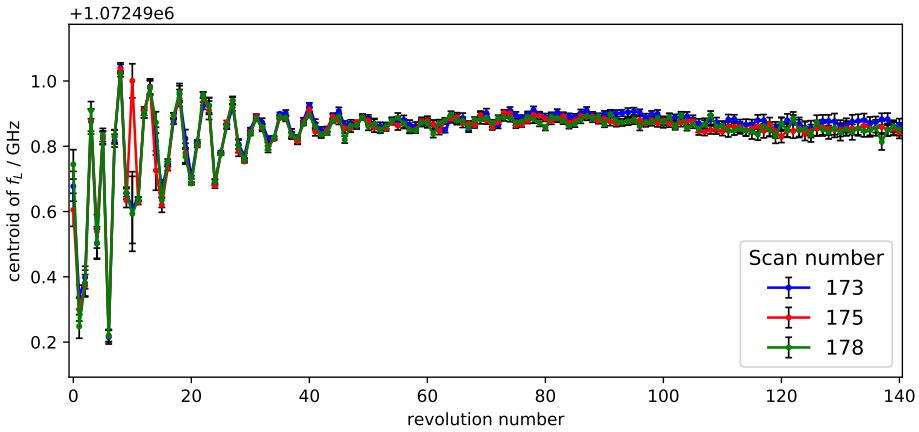

(a) $^{24}Mg^+$ ions: centroid over revolution number for three different scans

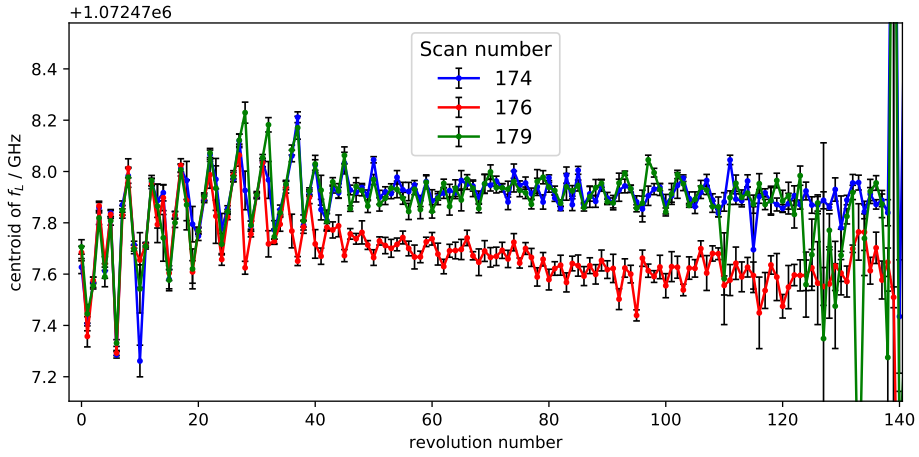

(b) $^{26}Mg^+$: centroid over revolution number for three different scans

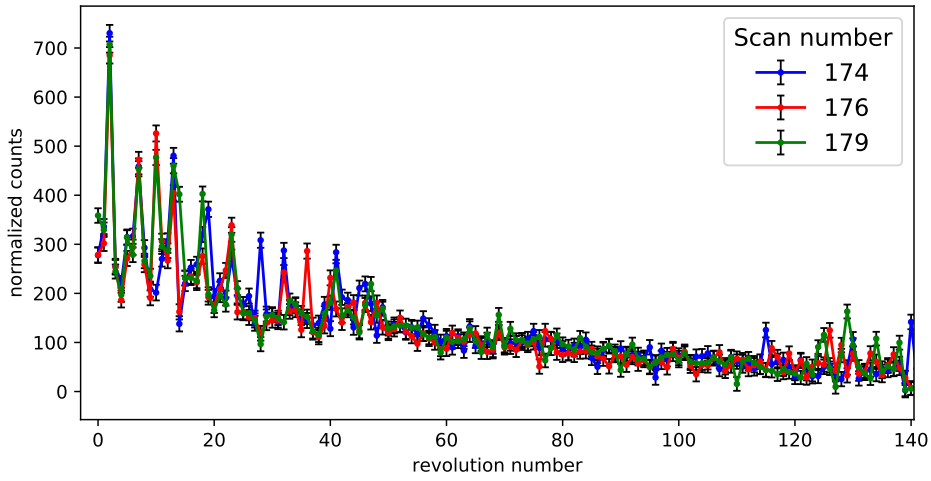

(c) $^{26}Mg^+$ ions: normalized photon counts over revolution number for three different scans

Figure 4.18: Fitted HFS resonance centroid (a) and (b) and counts (c) over revolution number for selected measurements of $^{24}Mg^+$ and $^{26}Mg^+$ ions during measurement campaign 1. The data is recorded with 100 ion shots per frequency step. The potential applied to the in-trap lift tube is 655 V and the pressure in the MR-ToF region is around $2.5 \cdot 10^{-7}$ mbar. The gate width used to obtain the time-gated hyperfine spectra is chosen with 2 μs.

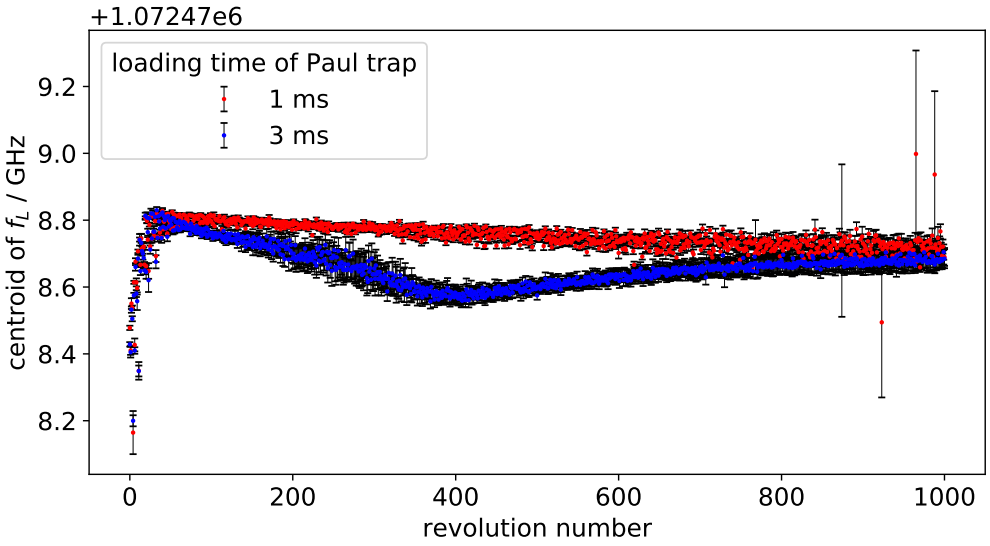

Figure 4.19: Centroid of the Doppler-shifted frequency for $^{24}Mg^+$ ions over revolution number for two different loading times, hence different amount of ions stored in the MR-ToF device. These data sets are recorded during measurement campaign 2 (measurement run number for the loading time of 1 ms: 2-148, measurement run number for the loading time of 3 ms: 2-153). The data is recorded with 300 or 500 ion shots per frequency step.

ions from the literature [6] and using the measured resonance frequency f_L of the $^{24}Mg^+$ ions in the lab frame, the kinetic energy of the ions in the middle of the central drift tube can be calculated. Similarly, the calculation of the kinetic energy can be done for the $^{26}Mg^+$ ions by taking the literature value for the resonance frequency f in the ions' rest frame for the $^{26}Mg^+$ ions [6] and the measured resonance frequency f_L for the $^{26}Mg^+$ ions in the lab frame. This kinetic energy is indeed lower than the kinetic energy calculated for the values of the $^{24}Mg^+$ ions. For measurement campaign 1 the kinetic energy difference is around 0.4 eV and for measurement campaign 2 the difference is around 2.3 eV. At the present status of measurements and analysis a mismatch in the in-trap lift timing leading to energy differences at this relatively small level cannot be fully excluded. Hence, this might be a possible reason for the disagreement of method 2 with literature values. However, the kinetic energy is still around 35 eV off from E calculated based on the measured potentials and simulation and the discrepancy in the two different methods for the calculation of the isotope shift can not be explained.

In summary, following the very first CLS signals in a MR-ToF device in August 2018, the first isotope shifts between $^{24}Mg^+$ and $^{26}Mg^+$ have been successfully measured. The comparison between the two different analysis methods in the calculation of the isotope shift as well as the comparison of their results and the accurate literature value reveals discrepancies which indicate a hitherto unidentified systematic effect. Several scenarios to explain these discrepancies have been investigated, but more work remains to resolve this issue. Especially, temporal system instabilities, space-charge effects, as well as accurate timing in the control of the $^{24}Mg^+$ and $^{26}Mg^+$ ions should be studied more carefully. It is here expected that future measurement campaigns as well as ion-optical simulations of the MR-ToF device from the CLS perspective will help for a better understanding of the experimental results for CLS within a MR-ToF device.

4.4 Simulations of the Proof-of-Principle Experiment

All simulations of ions' trajectories are carried out with SimIon (version 8.1.1.32) to find suitable potentials for the transfer of the ions from the Paul trap into the MR-ToF device as well as an optimal set of mirror potentials, such that a large fraction of trapped ions can be excited by the laser beam and a narrow linewidth approaching the Doppler limit can be reached. The simulations will help for a better understanding of the experimentally obtained data for CLS measurements within a MR-ToF device. Coulomb interactions between the different ions and between ions and image charges on the electrodes are not taken into account.

4.4.1 Simulations of Optimal Ion Transfer from the Paul Trap into the MR-ToF Device

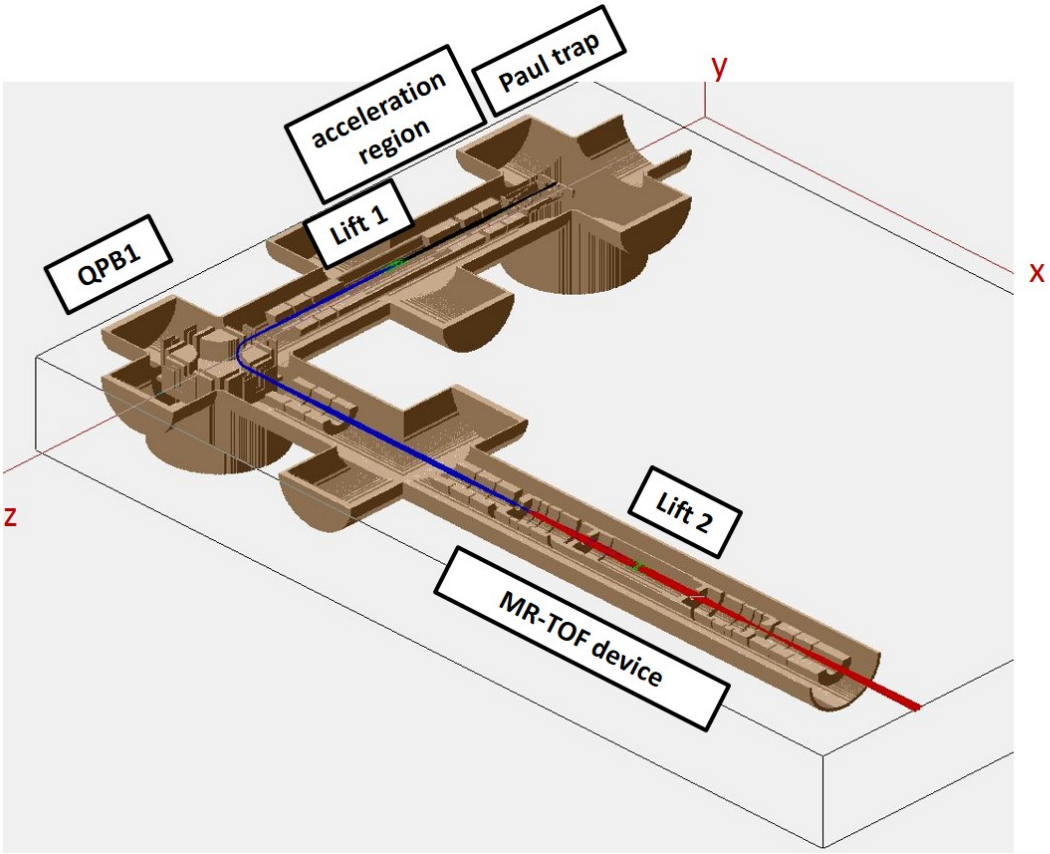

Figure 4.20: Simulations in SimIon for MIRACLS' PoP setup. The trajectories of 1000 ions are shown in black, blue and red. The ions start in the middle of the endcap of the Paul trap, are accelerated and injected into the MR-ToF device. The region where each individual ion sees the switching of lift 1 or lift 2 is marked in green. In this figure the ions perform 20 revolutions in the MR-ToF device before they are ejected. See text for details.

Simulations of ions' trajectories of the PoP setup are carried out to ensure optimal ion transfer from the Paul trap into the MR-ToF device. For this purpose, 1000 $^{24}Mg^{+}$ ions are created in the middle of the endcap hole of the Paul trap with a worst-case transversal emittance given by the geometry of the setup. The longitudinal emittance is varied separately (here σ_E is typically 1 eV). The position

of the ions inside the hole is given by a cylindrical distribution, where the start position is uniformly distributed in a cylinder with a radius of 1.25 mm and a length of 2.5 mm. For the direction of the ions a cone distribution with a half opening angle of 5 degrees is used. The kinetic energy at the start of the ions is Gaussian distributed with a mean of 55 eV and a standard deviation between 1 and 5 eV. The 55 eV represent the potential difference of the position where the ions are stored in the Paul trap (Segment 5 of the Paul trap has a voltage of 224 V) and the endcap potential (169 V) for ejection of the ions. The MR-ToF mirror electrodes are biased to a first trial combination which is known to perform well for mass measurements. The time that the ions need to travel from the endcap of the Paul trap to the middle position of lift 1 is recorded which is 2.52(4) μs. The simulation is repeated with switching of the lift 1 tube after 2.52 μs and the ions need another 8.13(5) μs to travel from the middle of lift 1 to the middle of lift 2. The simulation is repeated once more with switching of both lift tubes and the ion distribution is recorded in the middle of the MR-ToF device (hence in a field free region).

All the potentials along the beam line are varied to obtain the best injection into the MR-ToF device [48]. Although a tiny ion signal could be seen at the MCP with these simulated potentials in the experiment, the ion signal at the MCP is increased significantly by changing some of the potentials and applying potentials to the steerer electrodes. The simulation is repeated with the experimentally improved potentials of all the electrodes apart from the steerer electrodes that are all grounded in the simulation. However, utilising the experimentally found potentials for QPB 1 in the simulation leads to large ion losses during the transport into the MR-ToF device. Likely, this is caused by a 4 mm horizontal misalignment of the QPB 1 with respect to the MR-ToF axis in the experiment (see chapter A.1.2). Therefore the QPB 1 potentials differ significantly between simulation ($\pm$1575 V) and experiment ($\sim 1700/-2070$). Similarly, the lens 3 potential has to be changed in the simulation compared to experiment for an optimal ion-laser overlap in the middle plane of the MR-ToF device (experimental potential for lens 3: $\sim$ 640 V, potential in simulation: 1240 V). Apart from these bias voltages for QPB 1 and lens 3, and the steerer electrodes that are all grounded in the simulation, the experimental potentials are used for all the simulations presented in the following.

4.4.2 Search for Optimal Mirror Potentials of the MR-ToF Device in CLS Mode

The ion distribution in the middle of the MR-ToF device obtained after simulating the whole PoP apparatus as described in chapter 4.4.1 with a potential of the in-trap lift of 825 V is taken as a starting ion distribution for a separate, dedicated simulation of the MR-ToF device itself (see figure 4.21). Such a two-stage simulation approach is necessitated by limitations in computing power when considering the entire setup. In the simulation, the MR-ToF region is especially prone to electric field errors which are amplified while ions are stored for many revolutions in the trap. By exclusively considering the MR-ToF device and taking advantage of its cylindrical symmetry in the second step of the simulation, the linear geometrical resolution can be increased by a factor of 10 compared to the first-step simulation of the entire setup and electric field errors are minimized.

In order to identify suitable MR-ToF potentials for CLS, a Monte Carlo approach is employed utilising the ion distribution generated before. The potential of the innermost mirror electrode is varied between -6 kV and 0 V and the three other mirror electrodes between 0 and 6 kV. In figure 4.22 the randomly chosen combinations of mirror potentials which lead to a trapping efficiency of 100% for 20 revolutions in the MR-ToF device are shown. Each point corresponds to one potential combination that is characterized according to the mass resolving power, the spectral linewidth of the CLS spectra (Doppler width), and

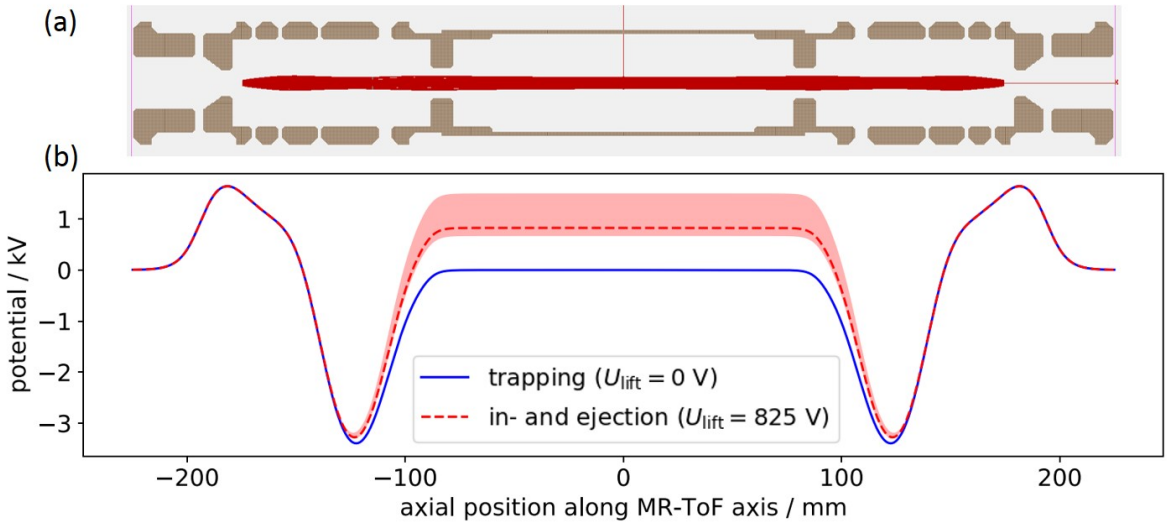

Figure 4.21: MR-ToF device of MIRACLS' proof-of-principle experiment: (a) Cut view of its electrode structure together with the simulated ions' trajectories (in red) for 1000 ions performing 100 revolutions in the MR-ToF device. (b) Electric potential distribution along the central axis of the MR-ToF device for the chosen set of mirror potentials. The potential distribution used for trapping of the ions is shown in blue. All bias voltages of the central drift tube prior to the switch of the in-trap lift leading to close to 100% trapping efficiency are shown in red. The one that is chosen for the simulations is marked with a dashed line.

the ion-laser overlap, e.g. the fraction of ions with a radial displacement r smaller than the laser beam radius. All of these are evaluated when an ion passes the axial middle plane of the central drift tube in the direction of the laser beam propagation during each revolution. The mass resolving power $R = t/(2\Delta t)$ is determined by the total flight time t and the time-of-flight width Δt at the middle plane of the MR-ToF device after a specific number of revolutions in the MR-ToF device (see chapter 3.3.1).

The Doppler width σ_f is given by the standard deviation of the Doppler-shifted resonance frequencies f in the lab frame (see chapter 2.3),

$$f = f_0 \frac{\sqrt{1 - \left(\frac{v}{c}\right)^2}}{1 - \frac{v \cos\alpha}{c}}, \tag{4.4}$$

where c is the speed of light, v the velocity of the ions, and α is the angle between ion path and laser-beam axis. The latter is assumed to be identical to the central axis of the MR-ToF device x. The angle α can be calculated from the velocity components of the ions v_x, v_y, v_z according to $\alpha = \arccos\left(v_x/\sqrt{v_x^2 + v_y^2 + v_z^2}\right)$. The resonance frequency f_0 in the rest frame of the $^{24}Mg^+$ ions is $1,072,082,934.33(16)$ MHz in the D2 line [6]. While both transitions are probed during the PoP experiments, the present simulations are without loss in generality restricted to the D2 line. For this thesis, we define the Doppler limit as the Doppler induced linewidth broadening exclusively due to the ions' velocity (hence energy) spread, that is in the limit of perfectly parallel ions' trajectories with respect to the laser beam. This is to distinguish it from the more general Doppler width which reflects the entire linewidth broadening due to Eq. 4.4, so the spread in the angles between ions' trajectories and the laser beam as well as in energy (see also chapter 2.3). At the present beam energies of 1.3 to 1.7 keV, the spectral linewidth of conventional CLS spectra is essentially governed by the Doppler limit. However, for a MR-ToF device, a further investigation has to be carried out, since typically an ion passes the

central drift tube at different angles α for different revolutions (see figure 4.28(b)), which can lead to an additional broadening.

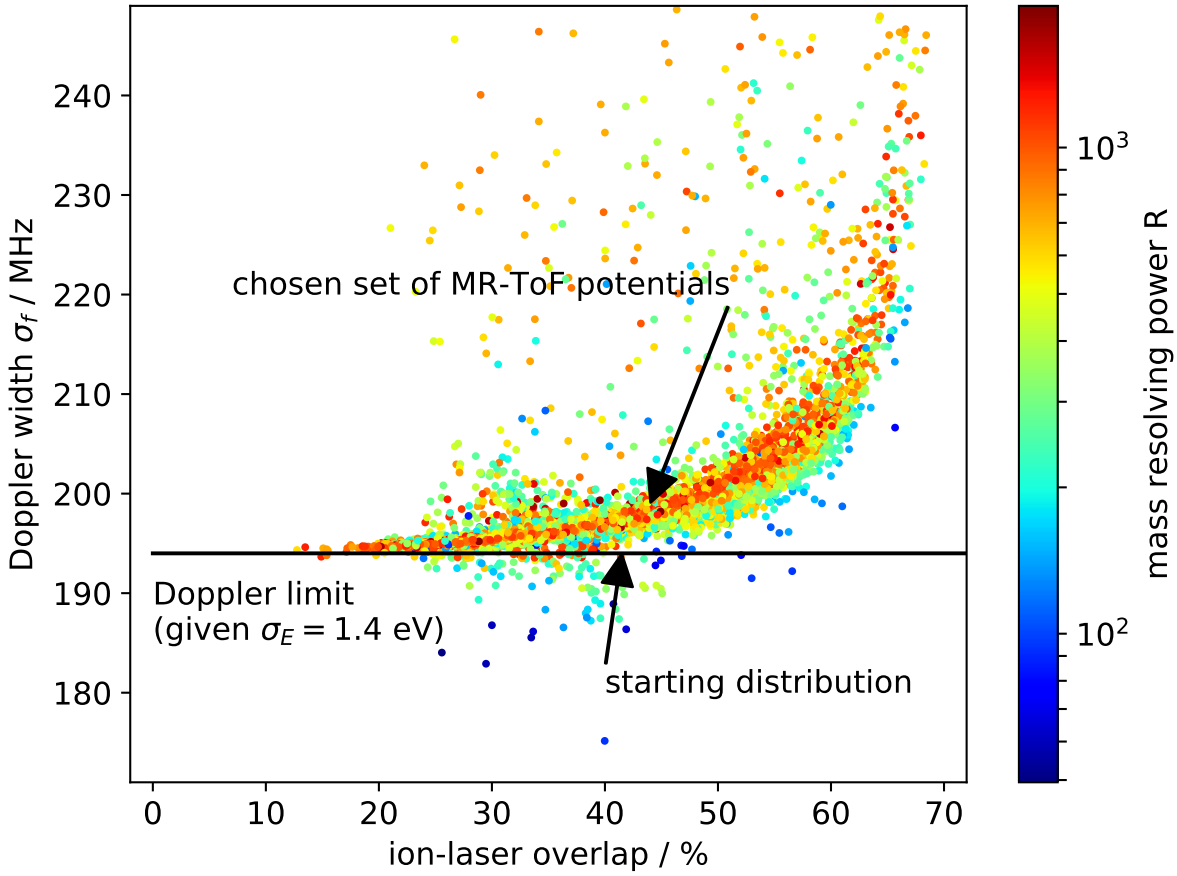

Figure 4.22: Doppler width σ_f and mass resolving power R versus the ion-laser overlap (assumed laser diameter: 2 mm) for different combinations of electric potentials of the MR-ToF mirrors as probed in the described Monte Carlo approach. The selected set of potentials for the rest of this chapter is marked with an arrow as well as the results of the ions' starting distribution. The evaluation of the starting distribution in terms of ion-laser overlap and Doppler width can be interpreted as how traditional CLS would perform based on such an ion distribution. Note that potential combinations with a Doppler width of up to 300 MHz summed over the 20 revolutions are found, that are not shown in this plot. The kinetic energy of the ions is $\sim$ 1479 eV and the energy spread (standard deviation) is 1.4 eV.

As figure 4.22 shows, the Doppler width is increasing with better ion-laser overlap. This behaviour is interpreted as a consequence of the conserved transversal emittance $\Delta r \Delta \alpha$. For a given emittance of the beam coming from the Paul trap, an increase of the spatial width Δr implies that the angular divergence $\Delta \alpha$ is decreased and so is the Doppler width. However, the increase of Δr also leads to a reduction of the overlap with the laser beam of fixed limited diameter. This observation emphasizes the importance of an excellent transversal emittance for highly sensitive and high-resolution CLS. Since the transversal emittance is governed by the beam preparation in the Paul trap [55], special attention will be given to this aspect of beam cooling and preparation in the future 30-keV MIRACLS' apparatus.
The calculated Doppler width for ions flying parallel to the MR-ToF axis (Doppler limit) is $\sigma_f = 194$ MHz for the assumed energy spread of $\sigma_E = 1.4$ eV and a kinetic energy of $\sim$ 1479 eV. In principle, this

should be the smallest attainable Doppler width for any potential combination. However, for a few sets of potentials the ions penetrate deeper into the mirror potentials and the angles α between MR-ToF axis and ion path tend to be correlated to the ions' velocities: Ions with large velocities v have in these cases typically larger angles such that their resonance frequencies in the lab frame matches to the ones of ions with smaller velocities which tend to have smaller angles in their trajectories to the laser-beam axis. Therefore, this correlation between v and α leads, according to Eq. 4.4, to a compression in the resonance frequencies f in the lab frame and the Doppler width can be smaller than the Doppler limit for these specific potential combinations (figure 4.22).
To illustrate the unusual appearance of a correlation between the angle α and the kinetic energy of the ions, figure 4.23 compares these parameters in the chosen set of MR-ToF potentials (which can be found in table 4.1) to the ones in the set of mirror potentials leading to the smallest Doppler width of just 176 MHz (where -3739.693, 1965.899, 304.134,1546.486 V are applied to the mirror electrodes ME1-4).

4.4.3 Simulated Results for One Specific Set of Mirror Potentials

In the following a set of potentials with a good compromise in ion-laser overlap, Doppler width and a reasonable mass resolving power is opted for, see table 4.1. High mass resolving power is equivalent to short ion bunches which leads to high signal-to-noise ratios when gating the photon counting on the passage of the ion bunch. In figure 4.21, its resulting potential distribution along the MR-ToF axis is shown for trapping (in-trap lift potential $U_{\text{lift}} = 0$ V) and for in- or ejection, where in-trap lift potential between 665 V and 1500 V result in close to 100% trapping efficiency for 100 revolutions. For higher kinetic energies the Doppler broadening is smaller and therefore in-trap lift potentials between 665 V and 870 V are preferred for the operation of the MR-ToF device in CLS mode. Within this potential range the difference in the Doppler widths is $\sim$ 35 MHz and in ion-laser overlap $\sim$ 12%. Thus, an in-trap lift potential of 825 V is selected for the simulations discussed below. Employing the selected set of MR-ToF mirror potentials and the chosen bias voltage of the in-trap lift, the ion beam injection from the Paul trap into the MR-ToF device is repeated. This confirms that the ion distribution obtained in the middle of the MR-ToF device is very similar to the ion ensemble utilised in the previous Monte-Carlo based probing of MR-ToF mirror potentials.

While all CLS simulations discussed so far assumed ions to be in the middle transversal plane of the MR-ToF device, photons emitted by ions within 45 mm on both sides of the center can also be detected efficiently [43]. However, only in a completely field-free region, the ion velocity is independent of its position in the ODR. In practice, remaining potential gradients result in slightly different velocities and hence different laser frequencies in the ions' rest frame. As shown in figure 4.24, in a region of 92 mm, the change in electric potential is less than 0.04 V corresponding to a change of the Doppler-shifted frequency of less than 5 MHz for an ions' kinetic energy of 1479 eV. Given the lifetime of around 3.8 ns [4] of the excited states of the D1 and D2 transitions for the Mg^+ ions and the kinetic energy in the MR-ToF device of 1.3 to 1.7 keV, an excited ion will typically move less than 0.5 mm until it decays back to the ground-state. Hence, ions potentially excited outside the ODR at different velocities (and therefore other resonance frequencies in the lab frame) will not be detected.

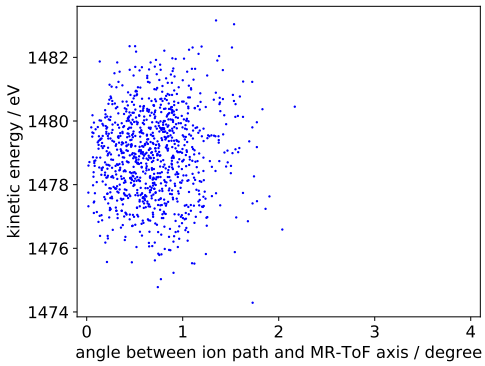

(a) starting ion distribution in middle of MR-ToF device

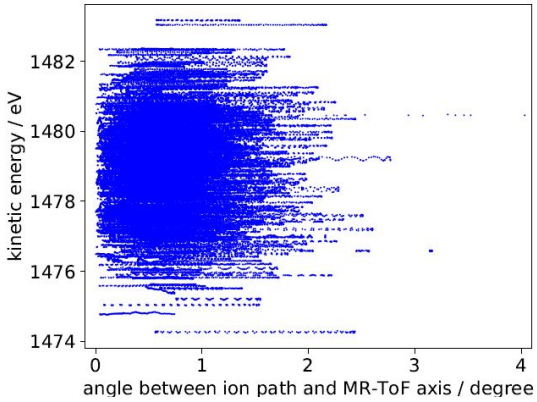

(b) all ions, chosen potentials

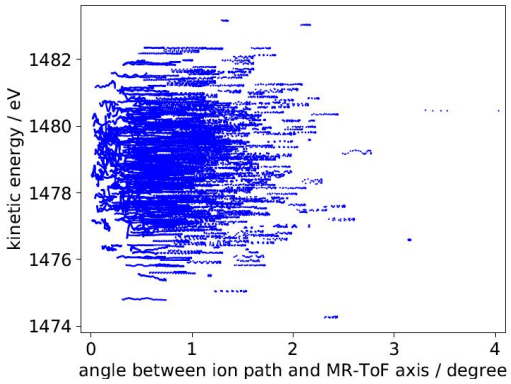

(c) excited ions, chosen potentials

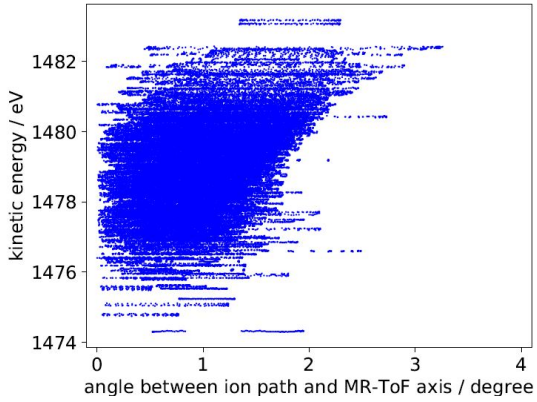

(d) all ions, potential with lowest Doppler width

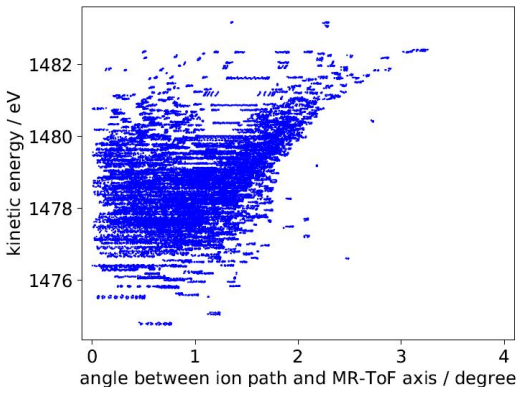

(e) excited ions, potential with lowest Doppler width

Figure 4.23: Kinetic energy versus the angle between ion path and MR-ToF axis: (a) starting distribution; (b) and (c) potential combination used in the experiment; (d) and (e) potential combination leading to the lowest Doppler width obtained in the Monte Carlo simulations. In (b) and (d) the results for all the ions are shown, whereas in (c) and (e) the results for only the laser-excited ions whose radial deviations from the MR-ToF axis are less than 1 mm are shown. See text for details.

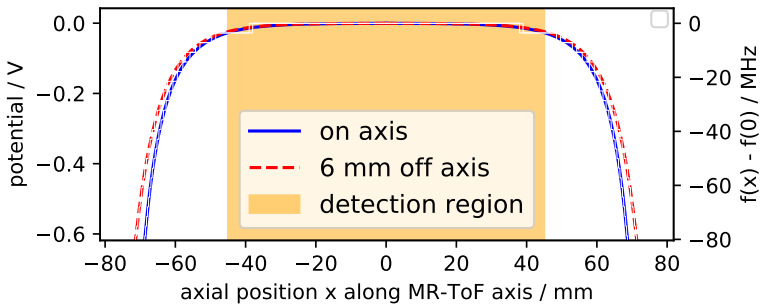

Figure 4.24: Electric potential and the change of the Doppler-shifted frequency $f(x) - f(0)$ for a kinetic energy of 1479 eV once for a $^{24}Mg^{+}$ ion flying along the central axis of the MR-ToF device and once on a parallel line shifted 6 mm off axis. The length of the ODR is marked in orange. The central drift tube itself is reaching from −106 to 106 mm.

4.4.3.1 Simulations Including the Ions' Thermalization in the Paul Trap

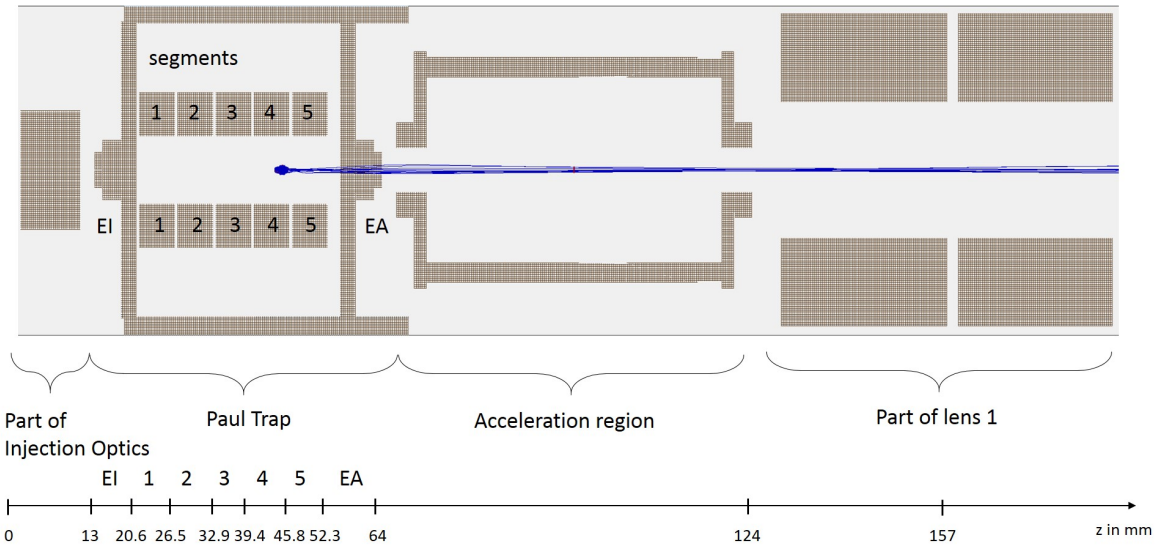

Figure 4.25: Cut view of the Paul trap and neighbouring electrodes. Examples of simulated ions' trajectories are shown in blue. See text for details.

In order to implement more realistic conditions for the transversal and longitudinal emittance, simulations of the ion preparation in the Helium-filled Paul trap are performed. Therefore, the Paul trap is implemented in SimIon similar to the simulations for the new MIRACLS' Cooler and Buncher [47]. A cut view of the simulation together with some sample ions' trajectories can be seen in figure 4.25. 1000 $^{24}Mg^{+}$ ions are randomly distributed around the trapping position in the Paul trap. The ions are thermalized through collision with Helium buffer-gas atoms at a pressure of 10^{-3} mbar. The ion-buffer-gas interactions are based on a hard-sphere collision model already implemented in SimIon. After 2 ms the ions are ejected from the Paul trap. For the simulations buffer gas is restricted to the cylinder hosting the Paul trap if not stated differently.

To validate the Paul trap simulations, the transversal and longitudinal transmittance of the extracted ion bunch will be calculated according to chapter 3.2.4 and compared to the simulated results. For the calculation of the transversal emittance equation 3.21 is employed. The circular RF frequency ω is given by $2\pi f$ with $f = 1.997$ MHz and the amplitude of the RF voltage V is 138 V. The normalization factor r_0 is half of the distance between two opposite rods (see figure 3.1) and is ~ 6.2 mm. According to equation 3.15 the dimensionless parameter q is ~ 0.367. The Paul trap operates at room temperature, therefore $T \approx 300$ K. The transversal 95%-emittance follows as $\sim 3.9\ \pi$ mm mrad for the mean kinetic energy of the ions in the middle of the acceleration zone of ~ 1196 eV, $\sim 2.8\ \pi$ mm mrad for a mean kinetic energy of the ions in the middle of pulsed drift tube lift 1 of ~ 2306 eV or $\sim 3.5\ \pi$ mm mrad for a mean kinetic energy of the ions in the middle of the MR-ToF device of ~ 1500 eV, corresponding to a rms emittance of ~ 0.65, ~ 0.47 or $\sim 0.58\ \pi$ mm mrad, respectively.

For the validation of the Paul trap simulation, the transversal emittance is estimated from the simulated ions' trajectories. Therefore the ion distribution is recorded at the middle plane of the acceleration zone or at the middle plane of lift 1, which is a field-free region. The rms emittance in the simulations calculated according to equation 3.5 with $u = x$ or $u = y$ and $u' = x' = \frac{v_x}{v_z}$ or $u' = y' = \frac{v_y}{v_z}$ is 1.05(6) π mm mrad at the middle plane of the acceleration zone and 0.73(2) π mm mrad at the middle

plane of lift 1.
To see the effect of the collisions with the helium atoms along the extraction path, the simulations are repeated with switching the buffer-gas pressure off once the endcap is switched for extracting the ions. In this case the transversal rms emittance is still 1.07(7) π mm mrad at the middle plane of the acceleration zone. The differences between the transversal emittance calculated according to equation 3.21 and the one extracted from the simulations might be due to the insufficient description of the collisions of the Mg^+ ions with the Helium buffer-gas atoms employing the hard-sphere collision model [80].

The longitudinal emittance can be calculated with the help of equation 3.17. For this purpose knowledge about the potential distribution along the Paul trap axis is required, which can be seen in figure 4.26. A zoom close to the region of the potential minimum (figure 4.26(c)) indicates that the axial potential there is in good approximation a parabolic function as stated in equation 3.19,

$$U(z) = U_0 + C_2(z - z_0)^2, \tag{4.5}$$

with $U_0 \approx 232.57$ V, $C_2 \approx 0.12$ V/mm^2 and $z_0 \approx 44.63$ mm. According to equation 3.18 the axial oscillation frequency ω_z is ~ 0.9822 MHz. The longitudinal 95%-emittance is (see equation 3.17) ~ 0.495 eV μs and the rms emittance is $\sim 0.495/6 = 0.0825$ eV μs. The rms emittance in the simulations calculated according to equation 3.7 is 0.146(5) eV μs for the ion distribution recorded at the middle plane of the acceleration zone, the middle plane of lift 1 as well as the middle plane of the MR-ToF device. The energy spread is 1.79(6) eV and the time spread is 83(5) ns in the middle plane of the acceleration zone. During ejection some of the ions collide with the Helium atoms and therefore their energy spread and consequently their longitudinal emittance increases. To investigate this effect, the simulations are repeated with switching the Helium pressure off once the endcap is switched for extracting the ions. There the rms emittance calculated according to equation 3.7 is 0.0340(32) eV μs, the energy spread is 0.752(15) eV and the time spread is 75.5(28) ns in the middle of the acceleration zone. The longitudinal emittance without buffer gas present during ejection of the ions is indeed smaller than for the case where a buffer-gas pressure of 10^{-3} mbar is present in the Paul trap region during extraction. However, the longitudinal emittance extracted from the simulations is not in agreement with the calculated value according to equation 3.17 perhaps again due to the insufficient description of the collisions of the Magnesium ions with the Helium buffer-gas atoms employing the hard-sphere collision model.
Although both longitudinal and transversal emittance exctracted from the simulation data differ significantly from the calculated emittances according to chapter 3.2.4, the ion distribution obtained after including the ions' thermalization in the Paul trap is regarded as more realistic than the one obtained for the scenario with the worst-case transversal emittance.

After ejection from the Paul trap the ion distribution is recorded in the middle plane of the acceleration zone and taken as a starting ion distribution for the previously discussed two-stage simulation. Even though in the middle of the acceleration region there is no field-free region, the simulations can be split at this plane, when the potential distribution at the splitting plane is exactly the same for the next simulation step as for the previous one. This is verified in two different simulations once without and once with splitting at the middle plane of the acceleration zone for the scenario with the worst-case transversal emittance.
Some ions undergo collisions with buffer-gas atoms during the extraction from the Paul trap which may change their flight trajectory. These ions are typically lost in the MR-ToF device within the first three

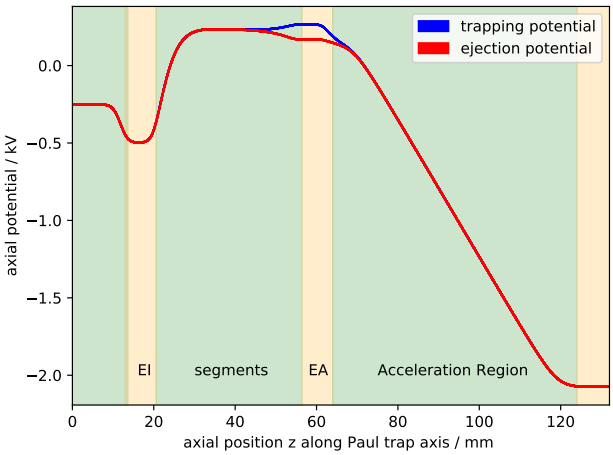

(a) potential distribution for injection optics, Paul trap, and acceleration region

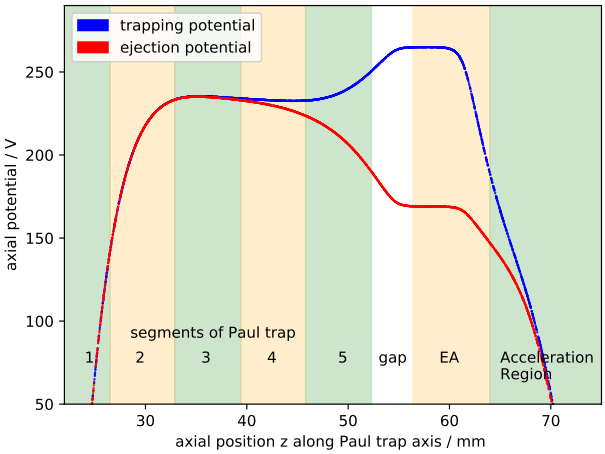

(b) potential distribution for the Paul trap region

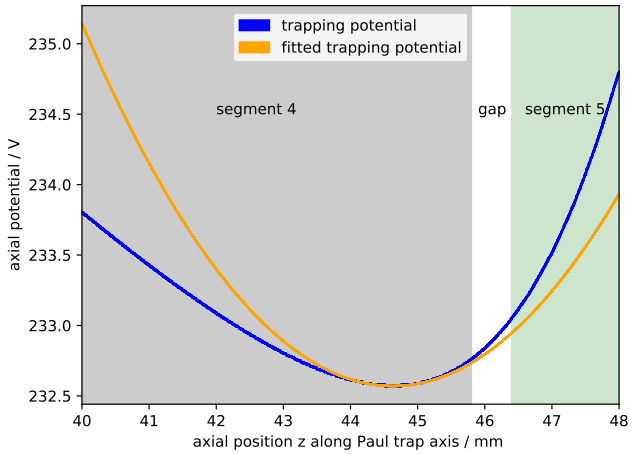

(c) potential distribution for the trapping region

Figure 4.26: Electric potential along the Paul trap axis as a function of the axial position z once for trapping (blue) and once for ejection (red) constituted by the electrodes shown in figure 4.25 when the bias voltages as listed in table A.1 are applied. Close to the potential minimum the axial trapping potential (blue) is in good approximation a parabolic function (orange) $U(z) = U_0 + C_2(z - z_0)^2$ with $U_0 \approx 232.57$ V, $C_2 \approx 0.12$ V/mm^2 and $z_0 \approx 44.63$ mm.

revolutions. Hence, the trapping efficiency is $\sim 97\%$. Once again, the ion distribution is recorded for each revolution when the ions pass the transversal middle plane of the MR-ToF device in the direction of the laser-beam propagation.

From this data, the radial distances of the ions in y and z to the central axis x of the MR-ToF device are shown in figure 4.27(a) for 100 revolutions. A laser beam with a diameter of 2 mm overlaps with 77% of the ions. Such a diameter of the laser beam is typically chosen in the experiment to keep the laser-induced stray-light background at a reasonable level. Exemplary for all simulated ions, sample ions are tracked for 2000 revolutions as they move in regular pattern through the MR-ToF device's transversal middle plane 4.28(a) with oscillating angles of flight trajectories to the MR-ToF axis (figure 4.28(b)).

For the simulated 1000 ions and a laser beam diameter of 2 mm, a histogram of the Doppler-shifted frequencies of the D2 transition in $^{24}Mg^{+}$ summed over 100 revolutions is shown in figure 4.27(b). The Doppler width due to the energy spread and varying angles between ions' trajectories and laser-beam axis is 160 MHz compared to the Doppler limit of 156 MHz for the energy spread of 1.2 eV of all laser-excited ions. A non-vanishing angle between ions' trajectories and laser-beam axis will shift the laser frequency observed in the ions' rest frame according to Eq. 4.4 in one direction, i.e. to lower values for a collinear ion-laser overlap (and to higher values for the anti-collinear case which is not considered here). This results in an asymmetric line shape. However, as seen in figure 4.27(b), this asymmetry is not pronounced since the angles between ions' trajectories and laser axis are small (average value of 0.4 degree, standard deviation of 0.4 degree) leading to shifts in mean values of typically only 12 MHz.

In figure 4.29 histograms of the angles between ion paths and MR-ToF axis are shown, once at the time where the ions hit the middle plane of the MR-ToF for the first time (a) and once where all 100 revolutions are taken into account (b). Note, that α is not Gaussian distributed because according to the definition of α only positive angles are possible and all directions around the MR-ToF axis are taken into account. The starting distribution is unrelated to the MR-ToF device. Hence, its evaluation can be interpreted as how traditional CLS would perform based on such an ion distribution. For the chosen set of MR-ToF mirror potentials, the distribution of α is quite the same for the starting distribution and for taking all the 100 revolutions into account. Therefore the Doppler width should be the same for the starting distribution and all the 100 revolutions. However, some of the ions with larger angles are lost in the MR-ToF device during the first few revolutions, therefore the Doppler width for the starting distribution is even slightly larger than the Doppler width taking all the 100 revolutions into account (see figure 4.30).

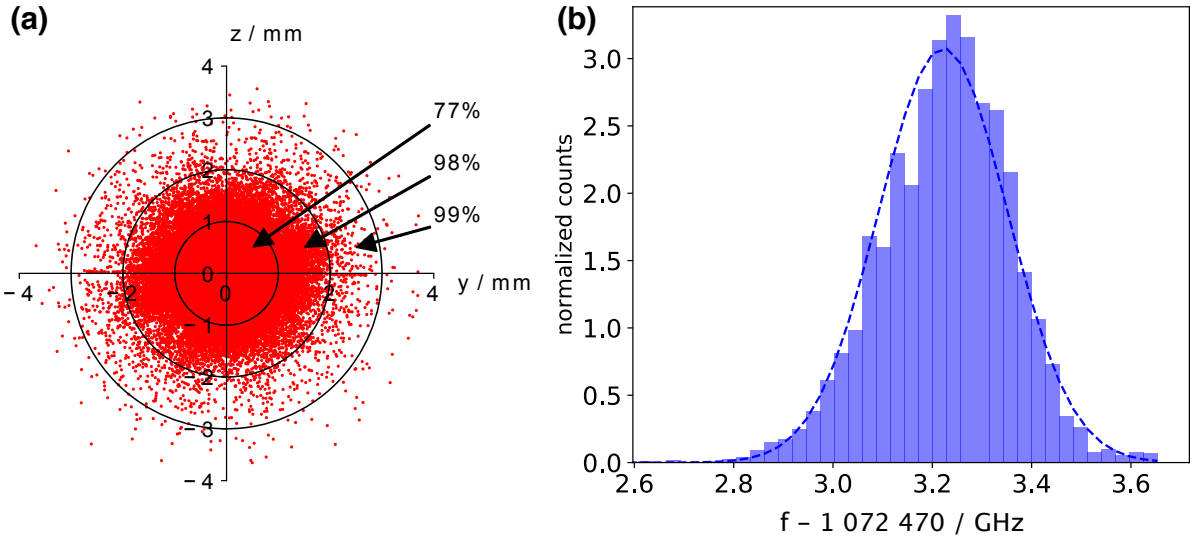

Figure 4.27: CLS-relevant results for the scenario including the ions' thermalization in the Paul trap when ions are stored in the MR-ToF device for 100 revolutions: (a) Transversal distances of the ions from the central axis of the MR-ToF device. A circle with a diameter of 2 mm, i.e. a typically laser beam size, spans over 77% of the ions. (b) Histogram of the Doppler-shifted frequency for CLS only considering the laser-excited ions for a laser beam with a diameter of 2 mm. A Gaussian line shape with centroid and width extracted from the data shows a slight shape asymmetry. See text for details.

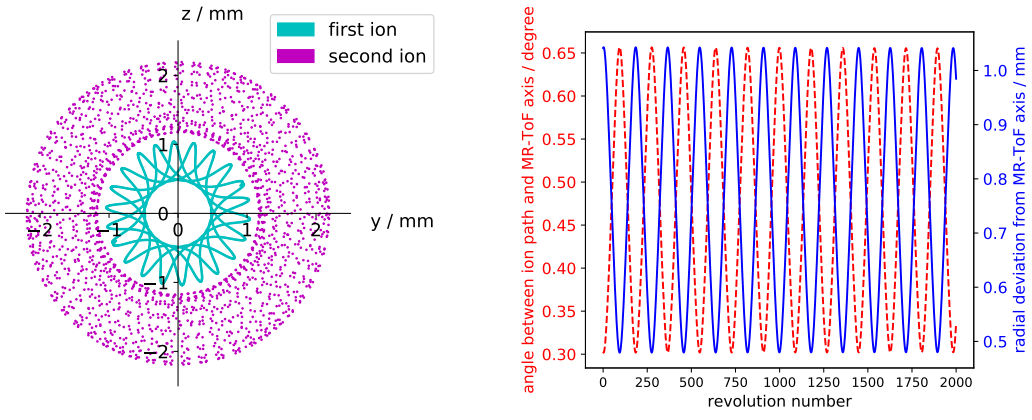

(a) (b)

Figure 4.28: (a) Transversal distances from the MR-ToF axis for two sample ions with different starting parameters (different angle to MR-ToF axis and different transversal distance to MR-ToF axis) for 2000 revolutions. (b) Transversal distance from the MR-ToF axis (blue) and angle between ion path and MR-ToF axis (red) for the first ion. The amplitude, phase, and frequency depend on the ions' starting parameters as well as on the potential combination of the mirror electrodes.

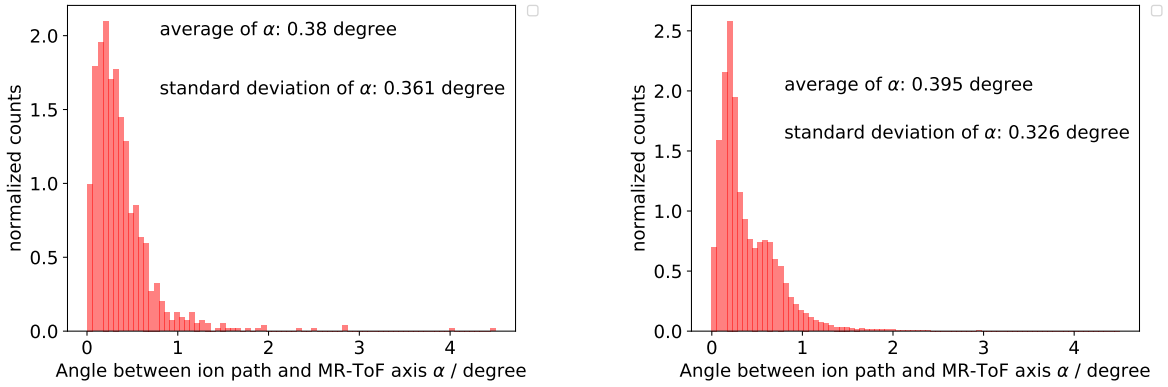

(a) starting distribution

(b) all 100 revolutions taken into account

Figure 4.29: Histogram of angles between ion path and MR-ToF axis for the 0th revolution (a) and for all the 100 revolutions (b). The simulation is based on the scenario including the ions' thermalization in the Paul trap.

4.4.3.2 CLS Parameters Versus Revolution Number for the Simulation Scenario Including the Ions' Thermalization in the Paul Trap

The evolution of the ion-laser overlap (a) and the Doppler width (b) with increasing revolution number can be seen in figure 4.30. It typically takes some tens of revolutions until the ions are accommodated to stable ions' trajectories in the MR-ToF device. This 'acclimatisation' process over the first few tens of revolutions is well visible in the ion-laser overlap (figure 4.30(a)). Although such a settling of the ions' trajectories during the first revolutions is known in other storage devices [89], it might in our case be due to ion-optical aberrations induced by QPB 1. QPB 1 transforms the previous elliptical shaped phase space area into a S-shaped area in the horizontal sub space (z, z'). Moreover, the ellipse is elongated in the vertical (y, y') space, most probably not related to QPB 1 but to beam translation. The phase space area can bee seen in figure 4.31 once before the QPB 1 (in the middle of lift 1) and once after the QPB 1 (in the middle of the MR-ToF device). Due to reflections in the MR-ToF device, the horizontal and vertical sub space are mixed (compare also to figure 4.28(a)) and the ion distribution in the (y, y') subspace becomes S-shaped, too, see figure 4.32. As illustratede in figure 4.32, after around 40 revolutions in the MR-ToF device the transversal ion distribution in the middle plane of the MR-ToF device has mostly an elliptical shape again and remains largely identical for consecutive revolutions. It is hence recommended to neglect the first few tens of revolutions for the actual CLS experiment in the PoP MR-ToF device. Moreover, for the 30-keV MR-ToF device it is not recommended to place a QPB before the MR-ToF device and use instead a 5-10 degree bent to facilitate the coupling of the laser beam into the beamline.
The phase space area in longitudinal direction is not effected by the quadrupole bender (see figures 4.31(a) and 4.31(b)) and remains the same for all the revolutions in the MR-ToF device.
The Doppler width for ions excited by a laser beam with 2-mm diameter is fluctuating between 130 and 200 MHz (figure 4.30(b)), mostly related to the fact that only 1000 ions are simulated. Hence, it depends which subset of ions can interact with the laser beam during one specific revolution number. For a larger laser-beam spot covering all ions the Doppler width is rather stable around 228 MHz, when the first three revolutions are neglected. The initial drop from 270 to 228 MHz is due to the loss of unsuitable ions within the first revolutions.

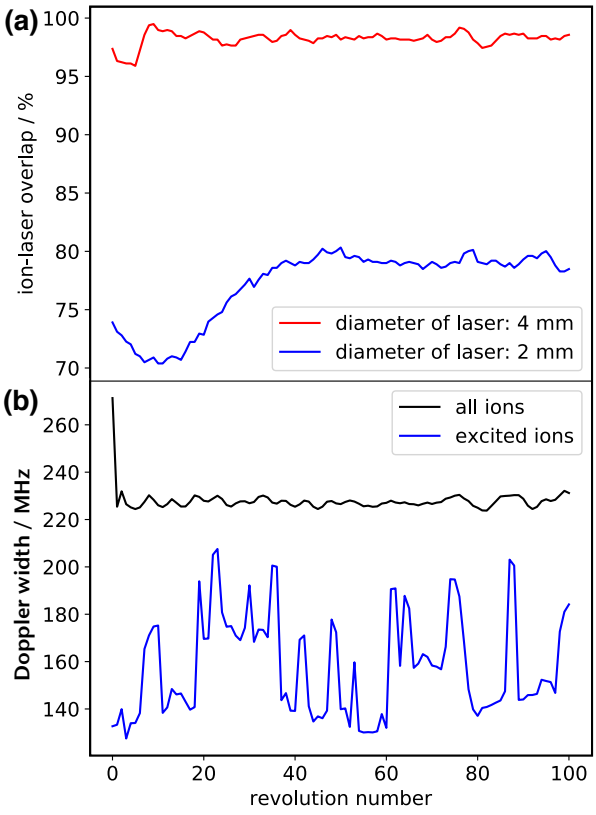

Figure 4.30: Ion-laser overlap (a) and Doppler width (b) versus revolution number for the simulation scenario including the ions' thermalization in the Paul trap. See text for details.

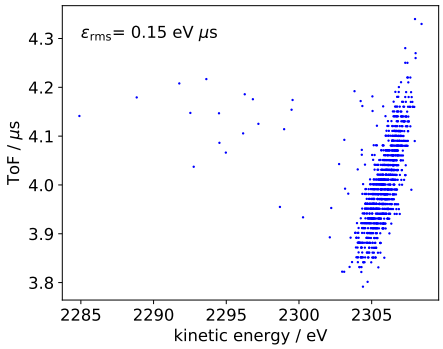

(a) action diagram in longitudinal direction in middle of lift 1

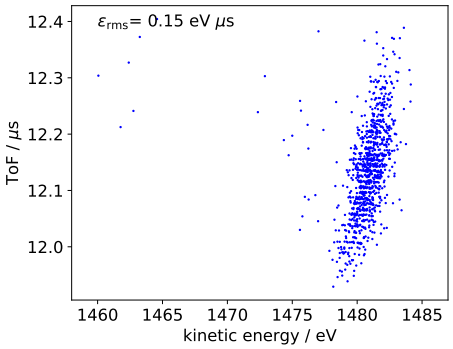

(b) action diagram in longitudinal direction in middle of lift 2

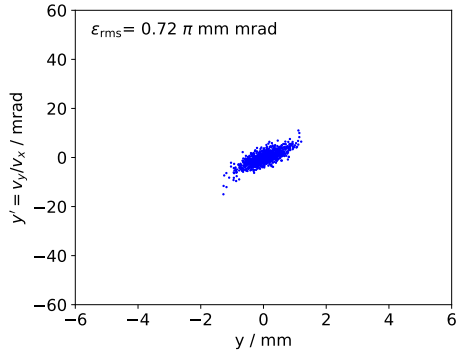

(c) action diagram in transversal sub space (y, y') in middle of lift 1

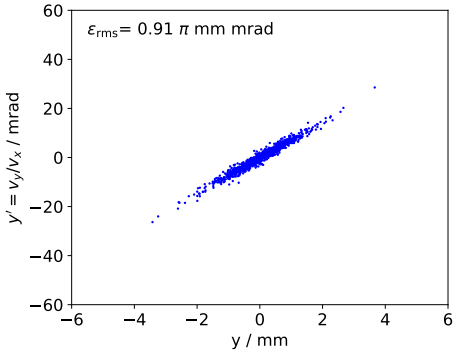

(d) action diagram in transversal sub space (y, y') in middle of lift 2

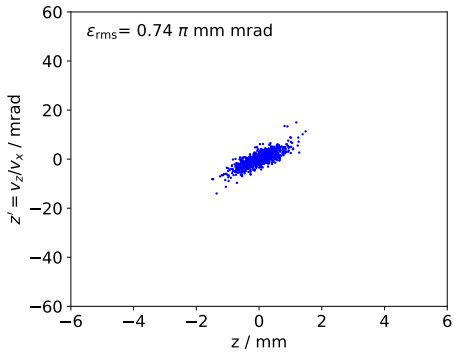

(e) action diagram in transvesal sub space (z, z') in middle of lift 1

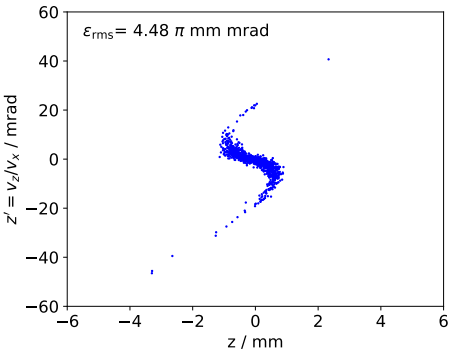

(f) action diagram in transversal sub space (z, z') in middle of lift 2

Figure 4.31: Action diagrams in the middle of lift 1 (left column) and in the middle of lift 2 (right column) for the simulation scenario including the ions' thermalization in the Paul trap without trapping of the ions in the MR-ToF device. The QPB 1 leads to a distortion of the shape of the transversal emittance. The phase space area is a conserved quantity. However, the calculated rms emittance can become large if a few particles are in the outer region of the phase space, as it is the case for the transversal emittance in the middle of lift 2. Therefore the calculated rms emittance is not staying constant in this case.

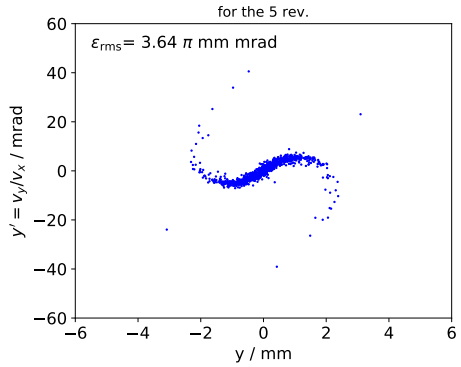

(a) action diagram in transversal sub space (y, y') for the 5th revolution

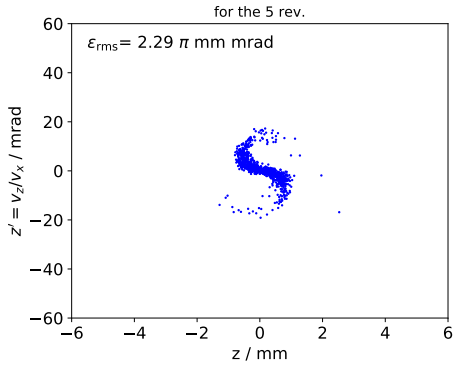

(b) action diagram in transversal sub space (z, z') for the 5th revolution

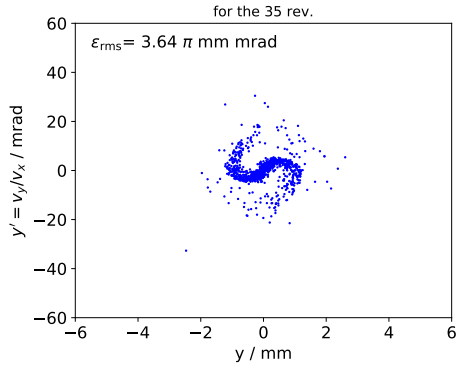

(c) action diagram in transversal sub space (y, y') for the 35th revolution

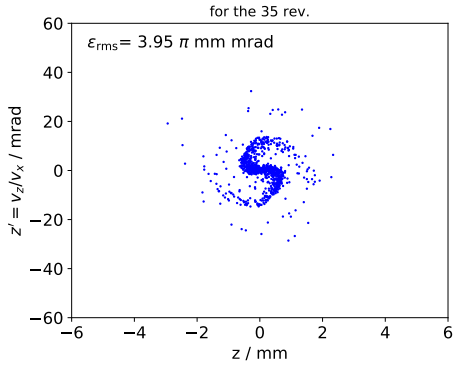

(d) action diagram in transversal sub space (z, z') for the 35th revolution

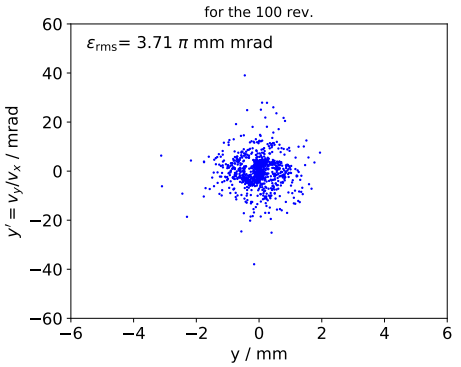

(e) action diagram in transversal sub space (y, y') for the 100th revolution

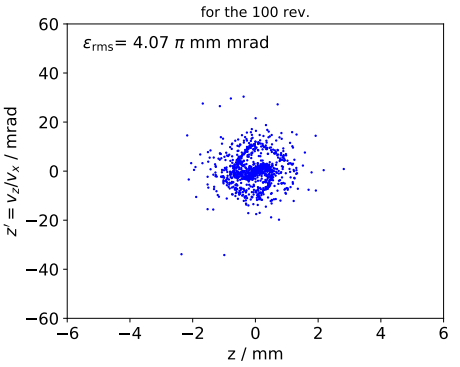

(f) action diagram in transversal sub space (z, z') for the 100th revolution

Figure 4.32: Action diagrams in the transversal sub spaces (y, y') (left column) and (z, z') (right column) in the middle plane of the MR-ToF device for the simulation scenario including the ions' thermalization in the Paul trap for the 5th, 35th and 100th revolution in the MR-ToF device. Due to the reflections in the MR-ToF device also the ion distribution in the (y, y') sub space becomes S-shaped. After around 40 revolution in the MR-ToF device the transversal ion distribution has an elliptical shape again and remains therefore largely identical for consecutive revolutions.

4.4.3.3 Comparison Between Scenario with Worst-Case Transversal Emittance and Scenario Including the Ions' Thermalization in the Paul Trap

In light of the limitations of the hard-sphere collision model [80], the discrepancies between the longitudinal and transversal emittance extracted from the simulation data and the calculated emittances according to chapter 3.2.4 and our incomplete knowledge about the helium pressure in the Paul trap, the results obtained for the simulation scenario including the ions' thermalization in the Paul trap are compared in Tab. 4.2 to the initially introduced simulation scenario based on a worst-case transversal emittance (see chapter 4.4.1). The results differ significantly only for the ion-laser overlap reflecting the large difference in transversal emittance. However, determining the experimental ion-laser overlap is not straightforward. The slight difference in the kinetic energy of the ions of 1.94 eV is due to the fact that the ions are not stored at the position of segment 5 in the Paul trap (as assumed for the scenario with the worst-case transversal emittance) but between segments 4 and 5 for the scenario including the ions' thermalization in the Paul trap. The spectral linewidth is dominated by the ions' energy spread in both cases, providing confidence that line shape distortions due to the MR-ToF characteristics are well under control in properly chosen settings.

Table 4.2: Summary of the simulation of the PoP experiment including the ions' thermalization in the Paul trap (right column, complete scenario) and for the worst-case transversal emittance (left column, worst-case scenario). For the latter an energy spread of 1.5 eV is assumed. A laser beam size of 2-mm diameter is assumed. Doppler widths, energy and angular spreads are given in one standard deviation. Both simulations are done with 1000 ions and 100 revolutions in the MR-ToF device.

	worst-case scenario	complete scenario
transversal rms emittance	5.3 π mm mrad	0.9 π mm mrad
trapping efficiency	100%	97.6%
average angle α between ion path and laser axis	0.8 degree	0.4 degree
spread of α	0.5 degree	0.4 degree
ion-laser overlap	47%	77%
kinetic energy (all ions)	1478.9 eV	1480.8 eV
kinetic energy (excited ions)	1479.0 eV	1480.9 eV
energy spread (all ions)	1.5 eV	1.7 eV
energy spread (excited ions)	1.4 eV	1.2 eV
spectral linewidth (all ions):		
Doppler limit	194 MHz	224 MHz
Doppler width	201 MHz	228 MHz
spectral linewidth (excited ions):		
Doppler limit	188 MHz	156 MHz
Doppler width	196 MHz	160 MHz

4.4.4 Comparison Between Simulated and Experimental Results

To investigate the influence of different lift 2 potentials prior called in-trap lift on the CLS characteristics the simulations including the ions' thermalization in the Paul trap are repeated with lift 2 potentials of 700 and 795 V. A summary of the simulated results for the most important parameters for CLS is given in table 4.3 for lift 2 potentials of 700, 795 and the previously chosen 825 V. For higher lift 2 values the kinetic energy of the ions is decreasing as expected whereas the energy spread stays within statistics the same. Hence, the spectral linewidth is slightly increasing with increasing lift 2 potentials. The time spread obtained after 100 revolutions is quite different for the different lift 2 potentials and will be discussed in more detail in chapter 4.4.4.3. All the other parameters, such as the angle between ion path and laser axis or the ion-laser overlap are fairly the same.

Table 4.3: Comparison between the simulation results for different potentials of lift 2. Doppler widths, time, energy and angular spread are given in one standard deviation. The simulations are done with 1000 ions and 100 revolutions in the MR-ToF device.

potential of lift 2	700 V	795 V	825 V
transversal rms emittance	0.9 π mm mrad	0.9 π mm mrad	0.9π mm mrad
trapping efficiency	99.43%	99.16%	97.6%
average angle α between ion path and laser axis	0.4 degree	0.4 degree	0.4 degree
spread of α	0.4 degree	0.4 degree	0.4 degree
average kinetic energy before the first revolution	1605.7 eV	1510.7 eV	1480.7 eV
energy spread before the first revolution	1.9 eV	1.9 eV	1.9 eV
average kinetic energy for all rev. (all ions)	1605.8 eV	1510.8 eV	1480.8 eV
energy spread for all rev. (all ions)	1.7 eV	1.7 eV	1.7 eV
average kinetic energy for all rev. (excited ions)	1605.98 eV	1510.94 eV	1480.95 eV
energy spread for all rev. (excited ions)	1.1 eV	1.2 eV	1.2 eV
Spectral linewidth (all ions)			
Doppler limit	216 MHz	218 MHz	224 MHz
Doppler width	232 MHz	228 MHz	228 MHz
spectral linewidth (excited ions)			
Doppler limit	140 MHz	153 MHz	156 MHz
Doppler width	145 MHz	158 MHz	160 MHz
ion-laser overlap	78%	79%	77%
time spread after 100 revolution	1700 ns	200 ns	116 ns

4.4.4.1 Trapping Efficiency in the MR-ToF Device

The suitable mirror potentials for CLS found by the Monte Carlo approach as explained above are tested in the experiment and it is indeed possible to trap for up to 5000 revolutions if the in-trap lift potential is greater than 650 V what is in good agreement with the simulated value of 665 V. However, ion losses over revolution number are visible in the experiment that are not present in the simulation. To obtain the experimental trapping efficiency, the ion counts at the MCP detector are measured as a function of the ToF since extraction from the MR-ToF device for revolution numbers between 1 and 300 in steps of one revolution for $^{24}Mg^{+}$ ions and for a lift 2 value of 815 V (see figure 4.33(a)). For the first 4 revolution $^{24-26}Mg^{+}$ isotopes are detected at the MCP detector. Afterwards the Magnesium isotopes separate in time such that they are at different times in the middle of the lift tube and only the $^{24}Mg^{+}$ ions are ejected from the MR-ToF device onto the MCP. However, after certain revolution numbers the

faster $^{24}Mg^+$ overtake the slower $^{25}Mg^+$ or $^{26}Mg^+$ ions and one of the two different isotopes is again at the same time in the middle of lift 2 and can therefore be seen at the MCP detector. Every time when $^{24}Mg^+$ ions overtake the slower $^{25}Mg^+$ or $^{26}Mg^+$ ions a horizontal line is visible in the colorcoded ToF distribution (see figure 4.33(a). Figure 4.33(b) shows the total ion counts at the MCP detector versus revolution number and reveals sizeable ion losses with increasing revolution numbers and hence storage time in the MR-ToF device. These ion losses are mainly associated with collisions with Helium atoms in the MR-ToF device. At the current setup, the separation of the vacuum section of the MR-ToF device from the vacuum section of the Helium-filled Paul trap is not sufficient (see appendix A.1.4). At ISOLTRAP it is possible to trap for over 2000 revolutions without significant ion losses [91]. Their vacuum pressure in the MR-ToF region is in the order of 10^{-10} mbar compared to the vacuum pressure of the PoP experiment in the order of 10^{-7} to 10^{-8} mbar. The measurement is redone with a factor of 7.5 lower pressure of Helium buffer gas in the Paul trap region, what also leads to an improvement of the vacuum quality in the MR-ToF section as described in chapter A.1.4. Even though the reduced Helium pressure in the Paul trap is not optimal for the cooling of the Mg ions, by increasing the loading time of the Paul trap still enough ions are transferred into the MR-ToF device and the ion losses versus revolution number are a factor of close to 4 less compared to the measurement with a factor of 7.5 higher Helium pressure in the Paul trap region. With the reduced Helium pressure it is possible to trap for over 5000 revolutions as can be seen in figure 4.34 for a scan over the revolution number up to 1000 revolutions. Due to sizeable drifts over time (see chapter 4.3.2) the potential of lift 2 has to be changed from 815 V to 795 V to obtain a slightly better time focus. However, for CLS in a MR-ToF device a good time focus at the MCP detector plane is less relevant and therefore is not further optimized here.

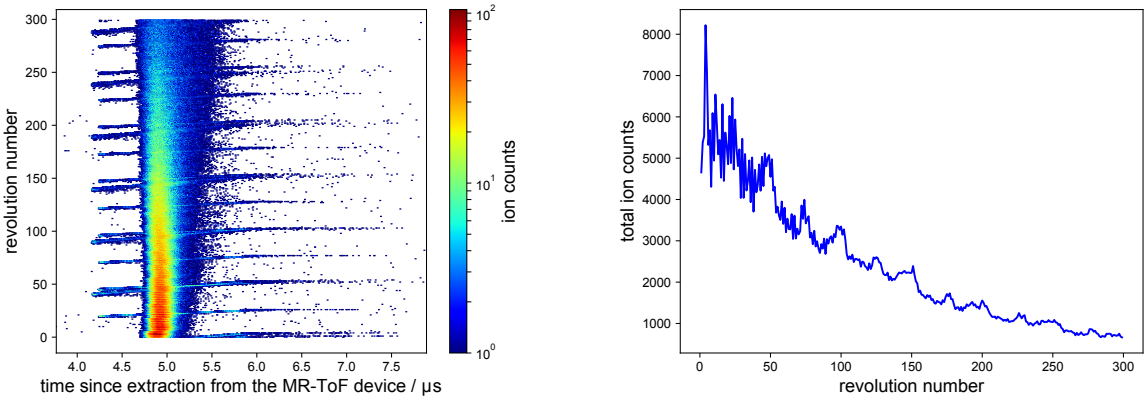

(a) (b)

Figure 4.33: (a) Colorcoded number of ion counts as as function of the ToF since extraction from the MR-ToF device for different revolution numbers for $^{24}Mg^+$ ions. (b) Total ion counts for each revolution as a function of revolution number. The duration of one revolution is 7.148 μs. The potential of lift 2 is 815 V and the data is recorded with 500 shots per scan. The pressure in the region of the Paul trap is $1.87 \cdot 10^{-5}$ mbar which corresponds to a vacuum pressure in the MCP region of $5 \cdot 10^{-7}$ mbar according to figure A.5. The pressure readings are normalized to N_2 as residual gas and the used vacuum gauges are not calibrated. Therefore this pressure values are only given to illustrate the relative changes in the vacuum.

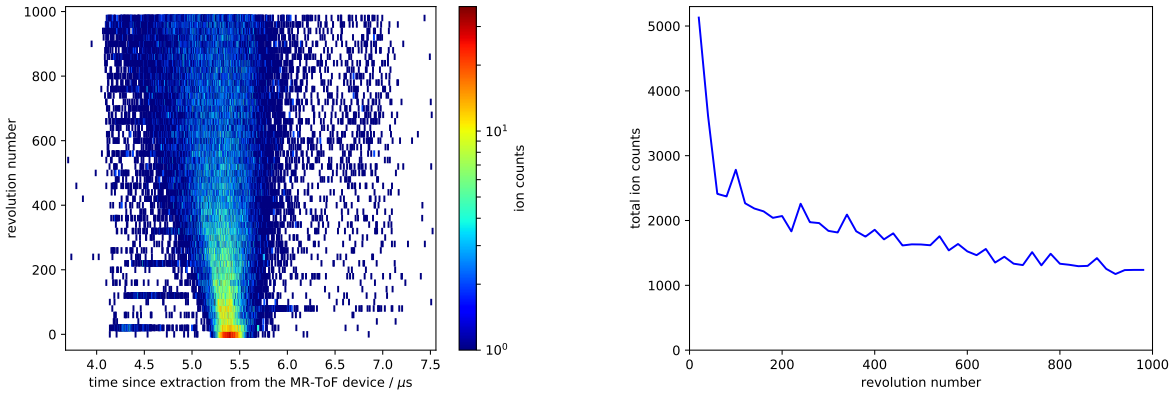

(a) (b)

Figure 4.34: (a) Colorcoded number of ion counts as as function of the ToF since extraction from the MR-ToF device for different revolution numbers for $^{24}Mg^{+}$ ions. (b) Total ion counts for each revolution as a function of revolution number. The time for 20 revolution is 142.975 μs. The potential of lift 2 is 795 V and the data is recorded with 300 shots per scan. The pressure in the Paul trap is $2.5 \cdot 10^{-6}$ mbar which corresponds to a vacuum pressure in the MCP region of $1.5 \cdot 10^{-7}$ mbar according to figure A.5.

4.4.4.2 Time Spread of the Ions Before the MR-ToF Device

One benchmark of the simulation approach is found in the ToF distribution of the ions measured by the MagneToF detector installed between the QPB 1 and the MR-ToF device. The FWHM in the ToF peak of the $^{24-26}Mg^{+}$ ions is 202(12) ns in the experiment. Its agreement with the 194 ns extracted from the simulation of 5000 $^{24}Mg^{+}$ ions provides some confidence in the Paul trap simulation. However, as can be seen in figures 4.35 and 4.36, it is not possible to resolve the $^{24-26}Mg^{+}$ ions experimentally, even though in the simulations the $^{26}Mg^{+}$ ions are resolved from the $^{24-25}Mg^{+}$ ions. Moreover the mean value of the experimental ToF from extraction from the Paul trap until detection at the MagneToF detector is 9.572(9) μs, whereas the simulated mean value for the $^{24}Mg^{+}$ ions is 8.8734 μs. The difference of $\sim$ 700 ns can be partly explained by the measured switch delay of the endcap of the Paul trap of $\sim$ 425 ns. The remaining $\sim$ 275 ns are currently not fully understood.

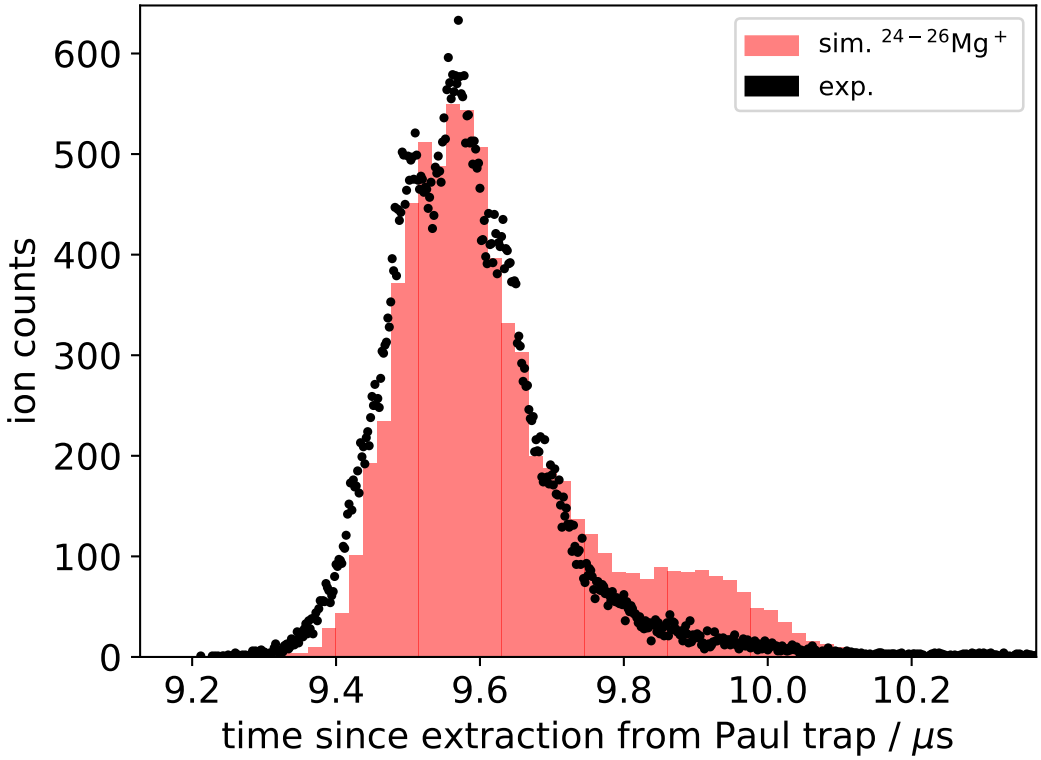

Figure 4.35: Comparison of the ToF distribution between simulation (red) and experiment (black) for $^{24-26}Mg^{+}$ ions recorded with the MagneToF detector installed between QPB 1 and MR-ToF device. The data is recorded with 1600 ion shots. The histogram of the simulated data is normalized to the experimental data and shifted by 700 ns in respect to the experimental data. See text for details.

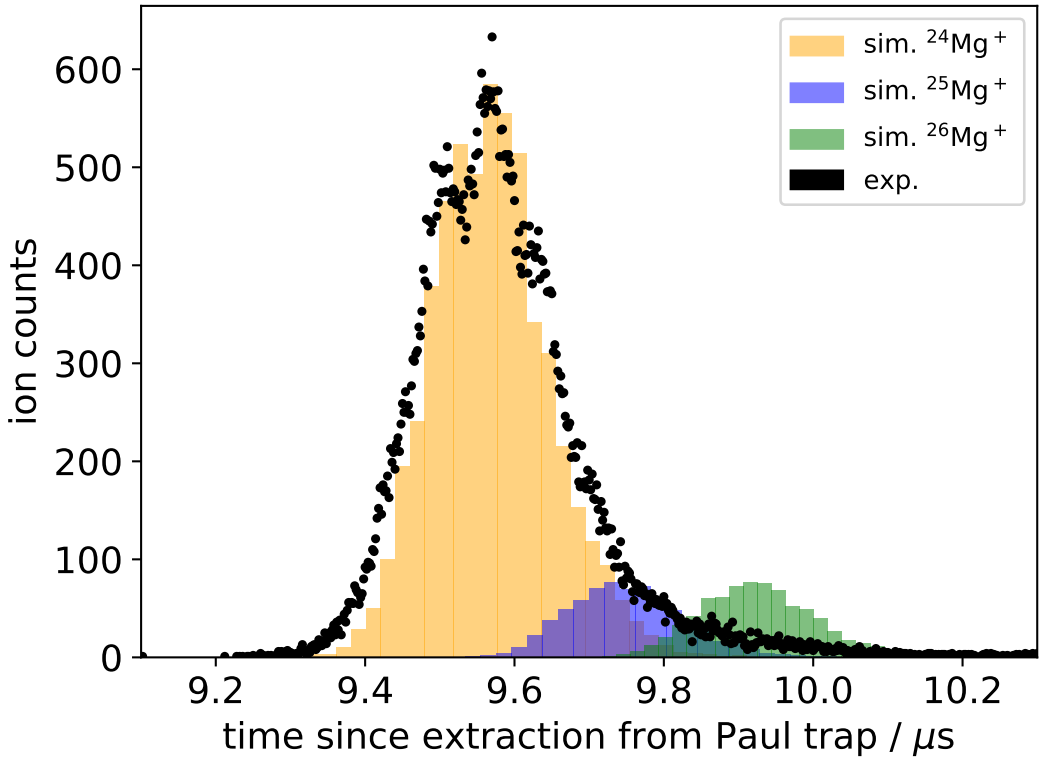

Figure 4.36: Comparison of the ToF distribution between experiment (black) and simulation for the individual $^{24-26}Mg^+$ ions (red, blue and green). The data is recorded with 1600 ion shots. The histogram of the simulated data is normalized to the experimental data and shifted by 700 ns in respect to the experimental data. See text for details.

4.4.4.3 Time Spread of the Ions Over Revolution Number in the MR-ToF Device

For a next benchmark of the simulations the time spread of the ion bunch over revolution number is measured and compared to the simulated data. To obtain the experimental time spread of the ions, the ions are ejected from the MR-ToF device after a certain revolution number and their ToF is recorded at the MCP detector. The recorded ToF distribution is fitted with a Gaussian function and the FWHM is extracted. The FWHM of the ToF distribution can be seen in figure 4.37(a) for different lift 2 values and different revolution numbers. The time spread Δt of the ions ejected after a certain revolution number r from the MR-ToF device is given by [91]

$$\Delta t = \sqrt{\Delta t_0^2 + (r\Delta t_1)^2}, \tag{4.6}$$

where Δt_0 is the initial bunch width given by the Paul trap and Δt_1 describes the dispersion per turn in the MR-ToF device. If Δt_0 is small enough, Δt increases in good approximation linearly with revolution number. Therefore, the experimental obtained datasets are fitted with a straight line. For a lift 2 of 830 V the slope is the smallest, for a lift 2 of 795 V the slope is higher and for a lift 2 of 700 V the slope is the highest. The reason for the different slopes is that for different lift 2 values the kinetic energy of the ions in the MR-ToF device is different and therefore the ions move differently far into the MR-ToF mirrors. Even though one data set (labelled with 795 V-11102018) is recorded more than a month before the other data sets with completely different parameters (especially potentials of the electrodes) on the ions' way from the Paul trap to the MR-ToF device, its slope is quite the same as for the two other datasets for a lift 2 potential of 795 V. This should be the case, because different parameters on the ions' way from the Paul trap to the MR-ToF device only change the initial bunch width Δt_0 but not the dispersions per turn in the MR-ToF device, if the mirror potentials and the in-trap lift potential of the MR-ToF device remain the same. Due to known drifts in the setup operation probably due to an insufficient temperature stability in the MIRACLS' lab, the measurement of the ToF distribution is repeated on the next day. No systematic differences are observed for the FWHM of the ToF distribution. For the simulations, the ion distribution is recorded for each revolution when the ions pass the transversal middle plane in the direction of the laser beam propagation for the scenario including the ions' thermalization in the Paul trap. From this data, the time spread of the ions is calculated for each revolution (see figure 4.37(b)). Again, the FWHM of the ToF distribution increases in good approximation linearly with revolution number and the slope is the highest for a lift 2 of 700 V, smaller for 795 V and the smallest for 830 V. Even though this behaviour is qualitatively the same as in the experiment, absolute values for the slope or the FWHM of the ToF distribution for specific revolution numbers are not in agreement between simulation and experiment (see table 4.4).
For a lift 2 value of 700 V and a revolution number >200 the experimental ToF distribution recorded with the MCP is not Gaussian anymore. This is related to the fact, that the width of the ion bunch is too big. Then, the ion bunch may extend beyond the field-free region of the MR-ToF's central drift tube. Hence, an increasing fraction of the ions is not properly ejected from the MR-ToF device during the final in-trap lift switching and those ions can not be directed onto the MCP anymore. The ions need around 7 μs for one revolution in the MR-ToF device and around 900 ns from one end of the detection region to the other. However for a lift 2 value of 700 V and a revolution number >200, their FWHM of the ToF distribution is greater than 1 μs already. Hence, a quantitative disagreement to the simulations is expected for higher revolution numbers. However, this observation does not explain the numerical discrepancies for earlier revolutions.

Table 4.4: Dispersions per turn Δt in ns/revolution for different lift 2 values for both simulation and experiment. The dispersions per turn are given by the slope of the fitted lines in figure 4.37.

lift 2	**700 V**	**795 V**	**830 V**
simulation	39.1	3.6	0.8
experiment -11102018		0.9	
experiment -13122018		1.3	0.4
experiment -14122018	3.6	1.3	
experiment -14122018-2	3.5		

In this context, it is interesting to note, that fluorescence-photon peaks recorded at the PMT are still visible for over 1000 revolutions. To first order, there is no significant broadening of the photon peaks visible over revolution number (see figure 4.38). This discrepancy to the results presented in this chapter might be related to the fact that for the CLS measurements typically many ions are stored in the MR-ToF device (likely a few thousand), whereas the measurements described here are done in single-ion-counting mode with a few detected ions per shot. Space-charge effects in the MR-ToF device may not be negligible for the ion number in CLS operation. This might lead to a so-called selfbunching of the ion beam as reported e.g. in [72] in which the FWHM of the ToF distribution becomes smaller if large amount of ions are stored in the MR-ToF device even though in principle the Coulomb interaction has repulsive character. If selfbunching is indeed the reason for the observations for larger ion numbers during CLS operation, it is speculated, whether this effect could also explain the discrepancy between simulation and experiment in the ToF width even in the single-ion-counting mode. If the number of stored ions in the MR-ToF device is largely underestimated when considering the ion counts on the MCP detector then space-charge effects as selfbunching may also occur in the data set to which the simulation of ToF widths is compared to. Indeed, some experimental evidence for a poor efficiency in the ion transfer from the MR-ToF device to the MCP detector has been found. For this reason, it is planned to install a retractable MagneToF detector straight after the MR-ToF device. This will enable close to 100%-transport efficiency from the MR-ToF device to the ion detector because the ions do not need to be bent by QPB 2 anymore. The number of stored ions can be solidly estimated and well controlled to ensure that less than ~ 5 ions are trapped in the MR-ToF device at a time such that space-charge effects will become negligible. Once the exact position of the new MagneToF detector is known, a new set of simulations can be carried out, where the ions are extracted after different revolution numbers from the MR-ToF device and the width of the ToF peaks for simulation and measurement can be compared at the actual detector position. These future advances in the experimental setup and simulation will consequently represent a more solid benchmark in terms of the ToF peaks' width over revolution number.

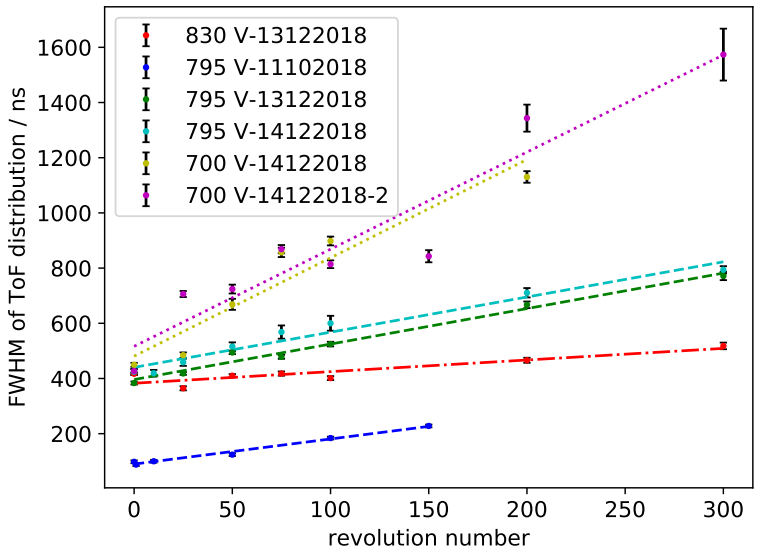

(a) experimental data

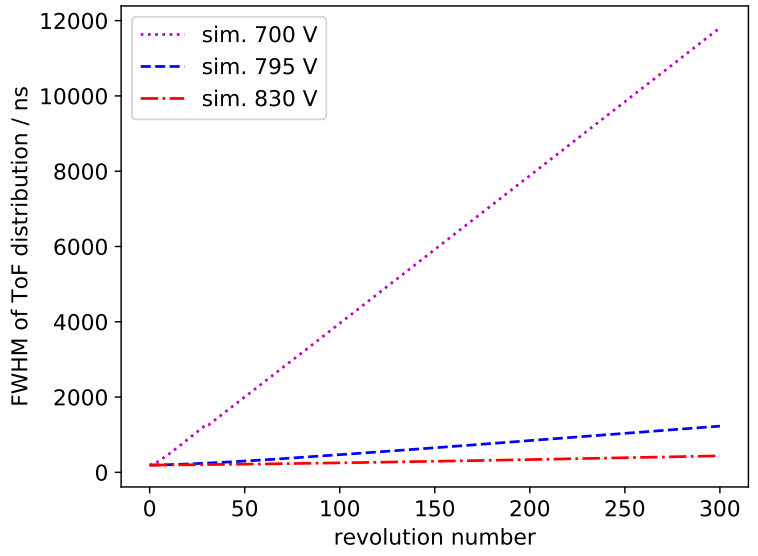

(b) simulated data

Figure 4.37: FWHM of the ion bunch's ToF distribution over revolution number for three different lift 2 potentials (700, 795 and 830 V). (a) Experimental data together with a linear fit. The ions are recorded at the MCP detector after they are stored in the MR-ToF device for the specific revolution number. The data is recorded in single-ion-counting mode with less than 10 ions/shot detected on the MCP. (b) Simulated data.

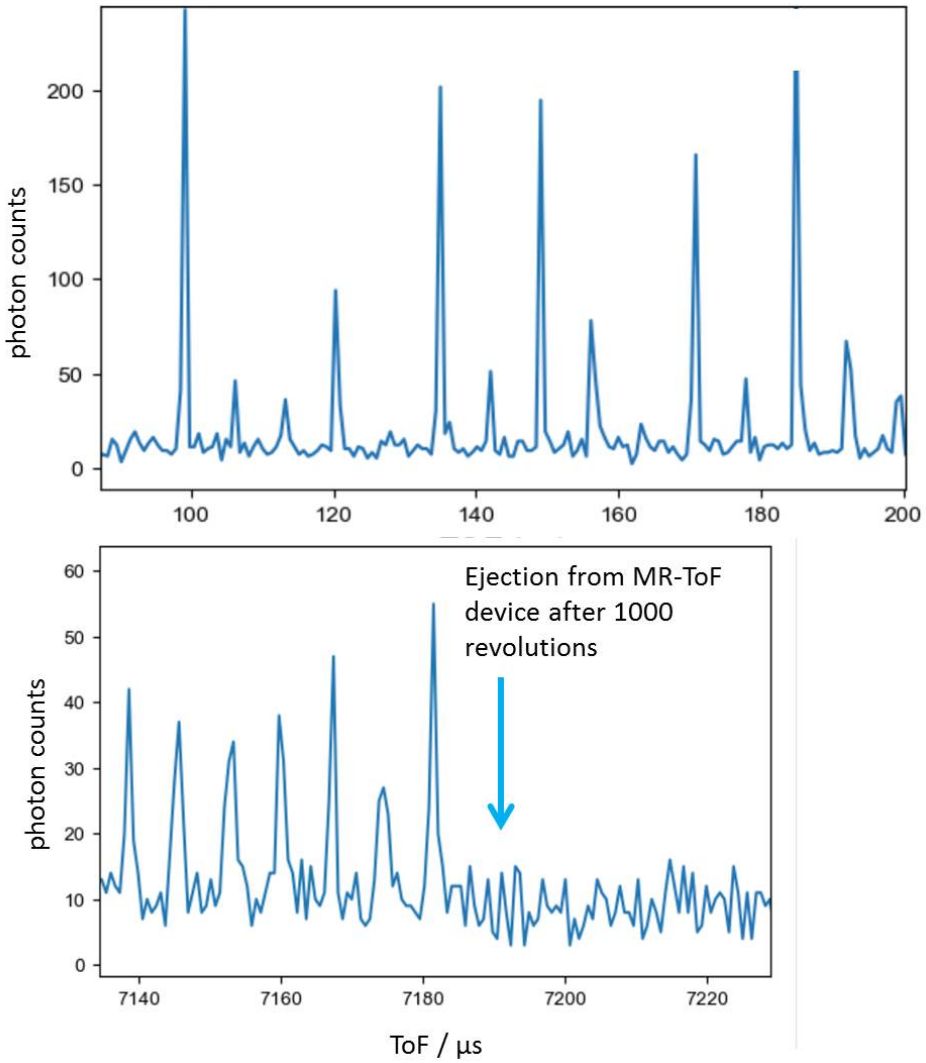

Figure 4.38: Distribution of the detected fluorescence photon counts versus the ToF of the ions since extraction from the Paul trap for the resonance frequency f_L. The data is recorded with 300 ion shots. Top: revolutions 12-25, bottom: revolutions 994-1000.

4.4.4.4 Time for One Revolution in the MR-ToF Device

Another benchmark of the simulation approach is found in the photon counts versus the ToF of the ions since extraction from the Paul trap at the resonance frequency of the $^{24}Mg^{+}$ ions (see figure 4.39). The simulated time for one revolution t_1 for an in-trap lift potential of 795 V is 7.1519(22) μs, whereas the experimental distance in the photon ToF peaks is 7.15(5) μs. According to simulations, the ions need a time of $\Delta t \sim 820$ ns from one end of the detection region to the other. The simulated time spread of the ions for the shown revolution numbers of 45-49 is $\sigma_t \sim 125$ ns. This leads to an increase of the duration of the fluorescence signals (see figure 4.39) which is in good agreement with the experimental ToF width of the recorded fluorescence-photon counts.
For a lift 2 of 700 V the time for one revolution extracted from the experimental data is 7.25(25) μs whereas the simulated time is 7.417(17) μs. Note that the experimental error for 700 V is higher than for 795 V because of a larger used DAQ bin width in the photon ToF. A comparison of the time for one revolution can also be seen in table 4.5 for the two different lift 2 potentials which summarizes the good agreement between simulation and experiment for this parameter.

Table 4.5: Time for one revolution t_1: Comparison between experiment and simulation for two different potentials of lift 2.

lift 2 potential	700 V	795 V
Experiment	7.25(25) μs	7.15(5) μs
Simulation	7.4170(17) μs	7.1519(22) μs

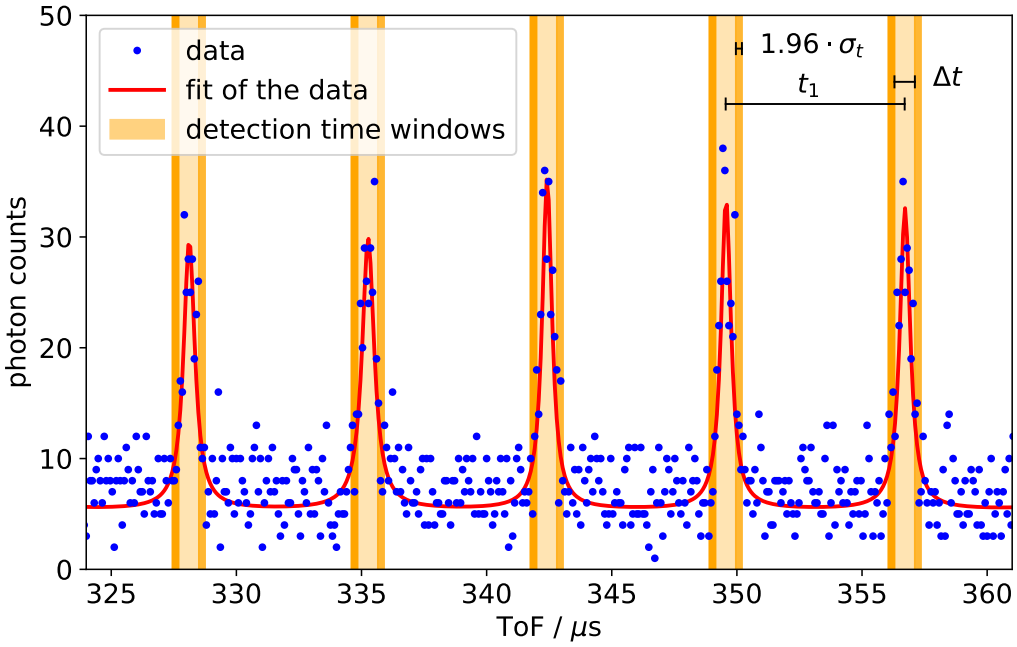

Figure 4.39: Detected photon counts versus the ToF of the ions since extraction from the Paul trap for 100 ion shots and a potential of lift 2 of 795 V. The photon peaks result from fluorescence photons associated with the passage of the ^{24}Mg ion bunch through the ODR. The photon peaks are fitted with a Gaussian line shape to guide the eye. The exact temporal peak shape is beyond the scope of this work. The simulated time duration of one revolution t_1 is indicated together with the time Δt a single ion needs to pass the ODR (light orange). The ions' ToF distribution causes an additional extension of the detection time windows, which approximative size is indicated by dark orange bands on both sides of the photon peaks. The duration of the combined orange bands corresponds to a 95% width of the ions' ToF peak, given by $3.92\sigma_t \approx 485\,\text{ns}$ for the shown revolution numbers of 45-49.

4.4.4.5 Spectral Linewidth

Table 4.3 provides a comparison of experimental and simulated CLS linewidth. Due to the fact that the natural linewidth is much smaller (42 MHz) than the Doppler width it can be neglected for the present discussion. The linewidth obtained in the experiment is indeed in the same order as the simulated Doppler width, see table 4.6. The simulated linewidth assuming that all the ions can interact with the laser is very close to the experimental obtained linewidth. In principle it could be that the laser-beam axis is not perfectly identical with the MR-ToF axis. Therefore the measurement is repeated with a slightly changed laser-beam axis (see chapter 4.4.4.8).

Table 4.6: Spectral linewidth (FWHM): Comparison between experiment and simulation for two different potentials of lift 2. The standard deviation of the simulated Doppler-shifted frequencies is multiplied by a factor of 2.3548 to obtain the FWHM of the Doppler width. The first value in the experimental line in the table is the linewidth for the ions that have a radial deviation of less than 1 mm from the MR-ToF axis and can therefore be excited by the laser with a diameter of 2 mm, the second value is the linewidth if all the simulated ions can interact with the laser.

lift 2 potential	700 V, 300 revolutions	795 V, 100 revolutions
Experiment	573(7) MHz	551(5) MHz
Simulation	371/535 MHz	342/547 MHz

4.4.4.6 Spectral Linewidth Over Revolution Number

The spectral linewidth is evaluated for each revolution in the MR-ToF device separately. Note that the first revolutions contribute more to the spectral linewidth for all the revolutions as given in table 4.6 because the photon counts are decreasing over revolution number (figure 4.40), mainly due to ion losses in the MR-ToF device, see figure 4.34.

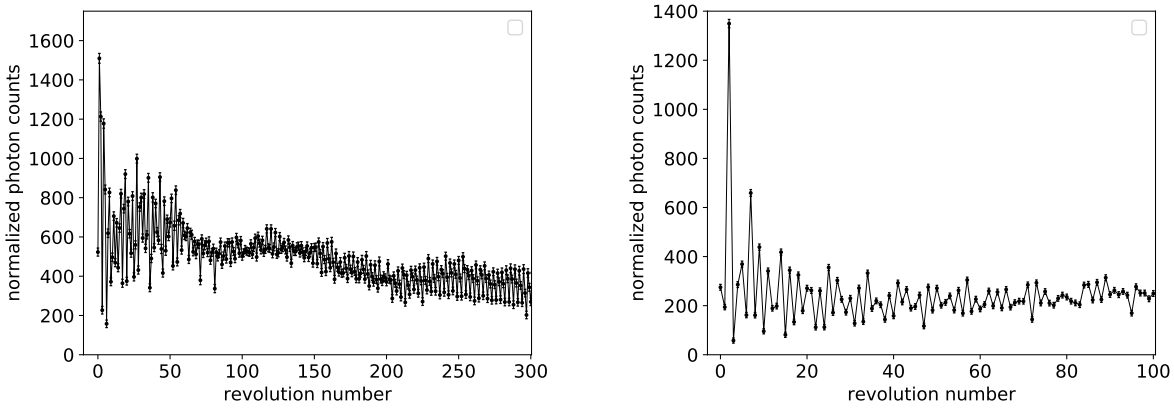

(a) lift 2: 700 V (b) lift 2: 795 V

Figure 4.40: Normalized photon counts over revolution number for a lift 2 of 700 V (a) and a lift 2 of 795 V (b). Lines are added to guide the eye.

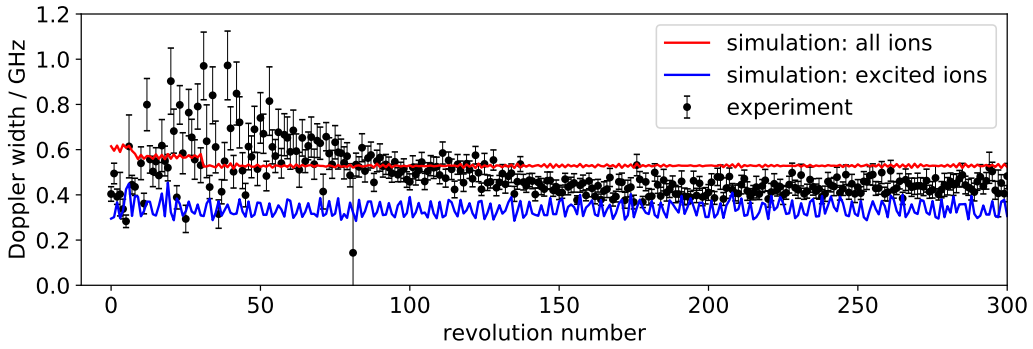

Figure 4.41: Linewidth (FWHM) versus revolution number for a lift 2 of 700 V. The red curve shows the simulated Doppler width for all the ions, the blue curve the one for the laser-excited ions with a laser diameter of 2 mm and the black points represent the experimentally obtained linewidth.

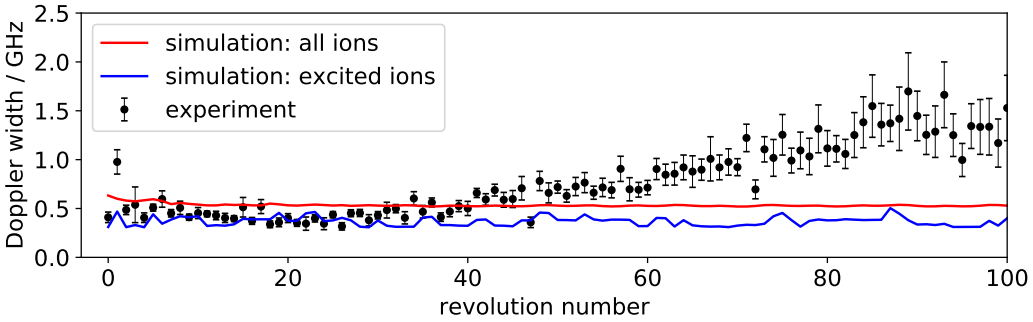

Figure 4.42: Linewidth (FWHM) versus revolution number for a lift 2 of 795 V. The red curve shows the simulated Doppler width for all the ions, the blue curve the one for the laser-excited ions with a laser diameter of 2 mm and the black points represent the experimentally obtained linewidth.

For a lift 2 of 700 V the experimental linewidth is larger than the simulated one for the first 75 revolutions and fluctuating between around 0.3 and 1 GHz (see figure 4.41). After 150 revolutions the experimental linewidth remains stable over revolution number at around 0.45 GHz and is in between the simulated values for all ions and for the ions that can be excited by a laser beam with a diameter of 2 mm. The deviations from the simulated linewidth for the first few revolutions as well as the fluctuations over the first few revolutions of the experimental linewidth might be explained by the fact that more ion losses take place during the first few revolutions in the experiment compared to the simulation. For a lift 2 of 795 V the experimental linewidth is stable within the first 40 revolutions and in good agreement with the simulated values. After 40 revolution an increase of the linewidth takes place from around 0.5 to 1.5 GHz. This increase of the linewidth over revolution number is not understood yet, although first experimental hints may point to space-charge effects when storing too many ions in the Paul trap or MR-ToF device (see chapter 4.3.2).

4.4.4.7 Centroid Over Revolution Number

The centroid of the Doppler-shifted frequency is evaluated for each revolution in the MR-ToF device separately for both the experiment and the simulation for two different potentials applied to the in-trap lift. Due to the fact that the simulations are done with an ion mass of 24 u that differs slightly from the actual mass of the $^{24}Mg^{+}$ ions, the centroids are not the same in experiment and simulation. Moreover, also the kinetic energy of the ions in simulation and experiment might be slightly different, as discussed in chapter 4.3.2.
Neglecting the first 20 revolutions, the centroid stays stable over revolution number for both experiment and simulation for a lift 2 of 795 V. The qualitative behaviour of the centroid versus revolution number is the same for simulation and experiment, providing confidence of the accuracy of the simulations. However, in the experiment the centroid is fluctuating on a bigger scale. Note, that there exists settings in the experiment where the centroid does not remain constant over revolution number as discussed in chapter 4.3.2. This might be related to space-charge effects in the MR-ToF device if too many ions are stored in the MR-ToF device.

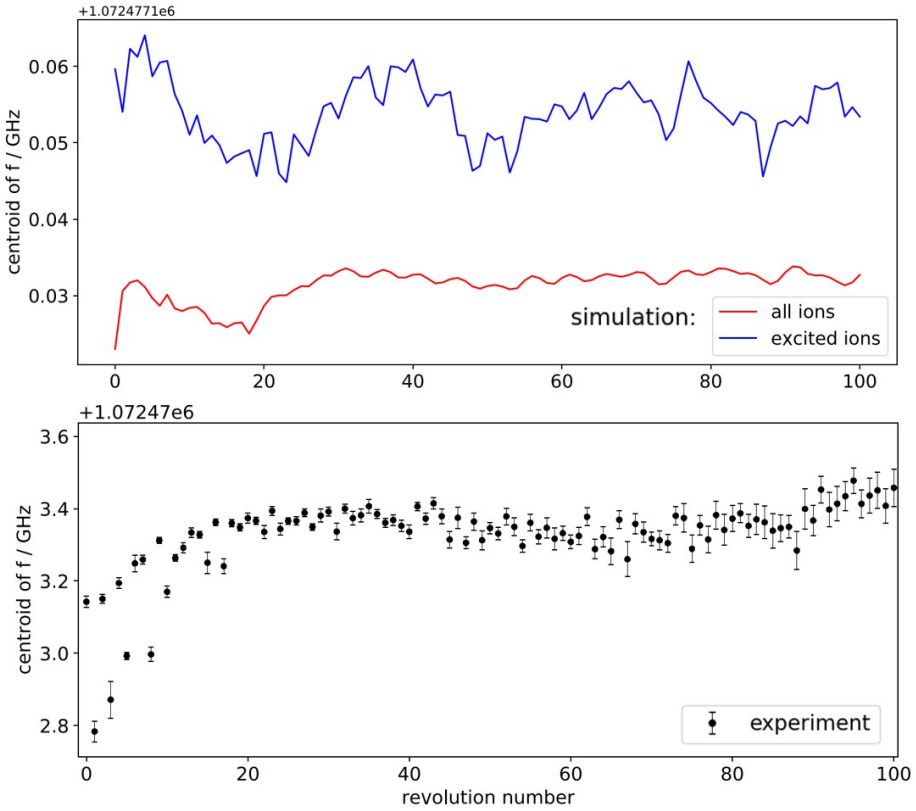

Figure 4.43: Centroid of Doppler-shifted frequency versus revolution number for a lift 2 of 795 V. The red curve shows the centroid for all the ions, the blue curve the one for the laser-excited ions with a laser diameter of 2 mm and the black points represent the experimentally obtained linewidth. Note the different scale on the y-axis.

4.4.4.8 1000 Revolutions

In the following the ions are trapped for 1000 revolutions in the MR-ToF device with an in-trap lift potential of 750 V. A hyperfine spectra, fitted with an asymmetric Pseudovoigt line shape is shown in figure 4.44. Compared to the experimental data sets described above a slightly different laser-beam axis is used and the FWHM of the line shape is reduced to 454(13) MHz. If the reduction of the FWHM is indeed related to the slightly different laser-beam axis or to the known systematic drifts in our setup remains an open question.
The simulated FWHM obtained by multiplying the standard deviation of the Doppler-shifted frequencies for 300 revolutions with 2.3548 is 359 MHz for the ions excited by a laser beam with 2-mm diameter and 527 MHz if all the ions could interact with the laser. The experimental linewidth lies now between the simulated values of the FWHM for the laser-excited ions and for all the ions. For the experiment it takes up to around 50 revolutions until the constant centroid is reached (see figure 4.45). This significant change in centroid during the first tens of revolution which is not seen in the simulation qualitatively explains the differences between experiment and simulation in the observed lineshape (in figure 4.44) and why the simulated FWHM with a laser beam size of 2 mm is lower than the experimental one.
The experimental Doppler width (see figure 4.46) is falling from around 0.8 GHz for the first few revolutions until 0.24 GHz within the first 100 revolutions. Afterwards the Doppler width is increasing from the 0.24 GHz to 0.34 GHz. For revolution numbers >400 the Doppler width remains constant over revolution number with around 0.34 GHz. The simulated Doppler width for the laser-excited ions stays constant over revolution number with 0.359 GHz and is therefore slightly higher than the experimental obtained Doppler width for most of the revolutions. Again the photon counts are decreasing over revolution number, most probably related to the ion losses in the MR-ToF device (see figure 4.47).

This CLS measurement demonstrates best that it is indeed possible to laser-excite ions during each revolution in a MR-ToF device until the ions are released from the MR-ToF device after 1000 revolutions here. Thus, the observation time is extended in comparison to traditional CLS and nuclides with very low production yields will become accessible for the very first time with CLS. At the moment the observation time in the PoP setup is determined by ion losses in the MR-ToF device. However, by improving the vacuum quality in the MR-ToF region, ion losses should become negligible and the observation time is expected to be only limited by the half-life of the ions. The observation of ion losses in the experiment is one major difference to the simulation which shows a trapping efficiency close to 100%. As the experimental vacuum quality in the MR-ToF device has been identified as its major cause, it is likely that collisions of ions with residual gas atoms and ultimately ion losses will also effect other CLS observables. It is hence encouraging that nevertheless experiment and simulation qualitatively agree well. Especially, parameters which are largly uneffected by these collisions and ion losses such as the revolution period (see chapter 4.4.4.4) are in excellent, quantitative agreement. This provides confidence in the simulation approach, which will be applied to MIRACLS' future MR-ToF device in the next chapter 5, even though some work in its validation in the PoP experiment remains for future work as discussed in this chapter.

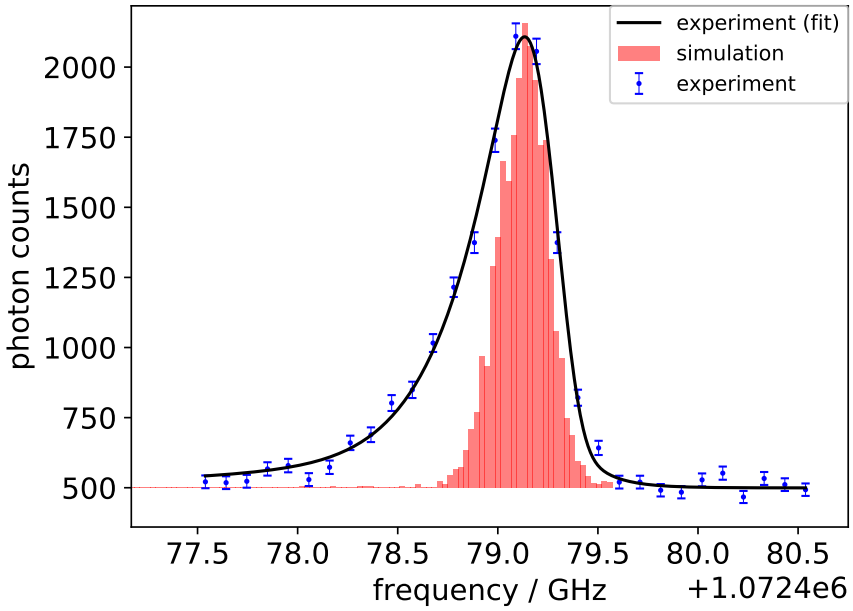

Figure 4.44: Time gated hyperfine spectra (blue dots) for a lift 2 of 750 V fitted with an asymmetric Pseudovoigt line shape (black). The experimental data is recorded with 100 ion shots per frequency step. The chosen gate width is 2 μs. A histogram of the simulated Doppler-shifted frequencies in the lab frame is shown in red for comparison. Note, that the histogram had to be shifted due to the fact that the simulations is carried out with a mass 24 u and not the correct ion mass.

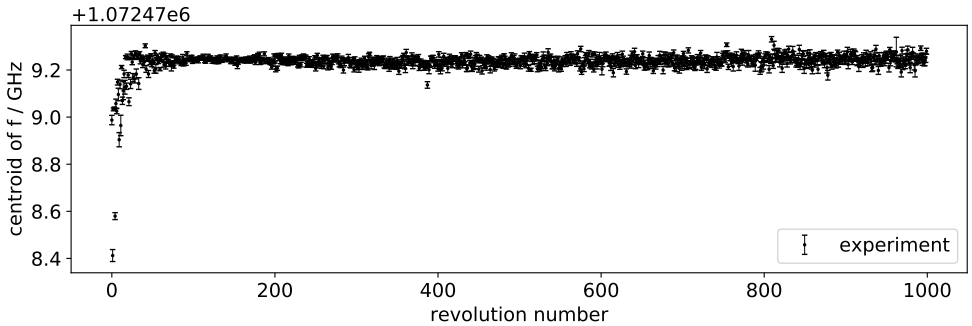

Figure 4.45: Centroid of Doppler-shifted frequency versus revolution number for a lift 2 of 750 V.

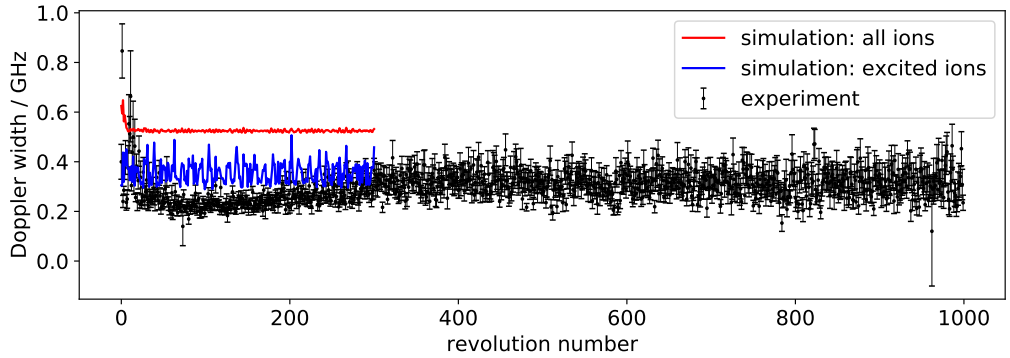

Figure 4.46: Linewidth (FWHM) versus revolution number for a lift 2 of 750 V. The red curve shows the simulated Doppler width for all the ions, the blue curve the one for the laser-excited ions with a laser diameter of 2 mm and the black points represent the experimentally obtained linewidth.

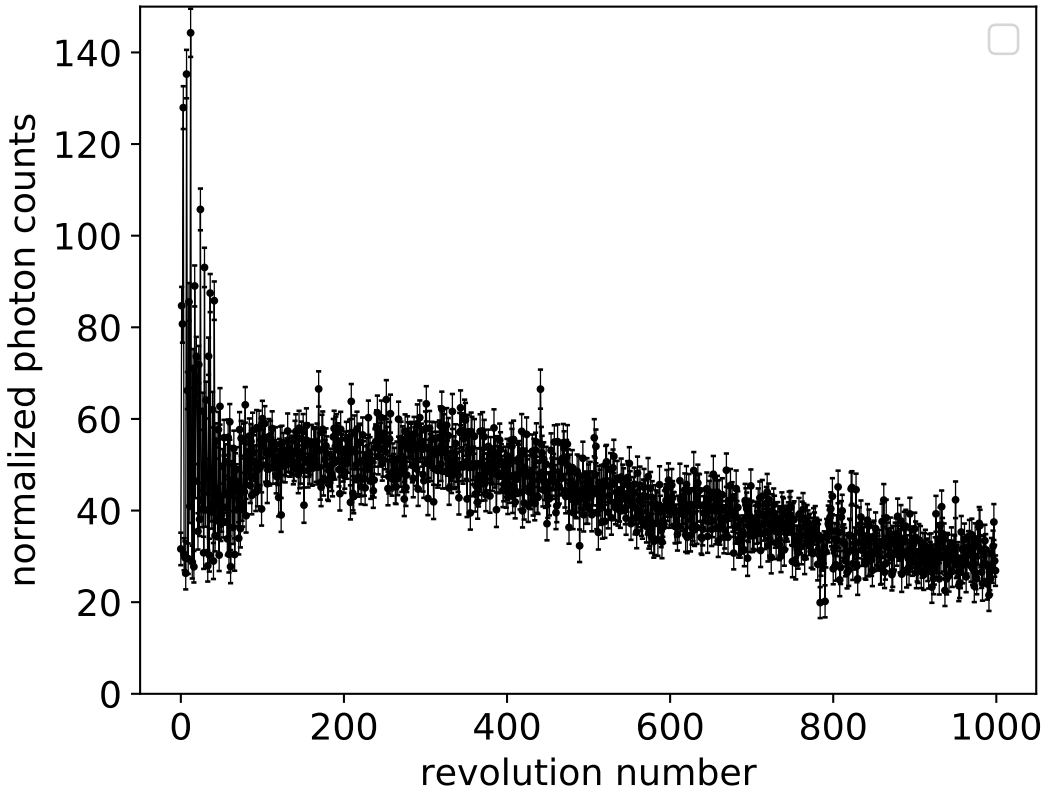

Figure 4.47: Normalized photon counts over revolution number for a lift 2 of 750 V.

Chapter 5

The 30-keV MR-ToF Device for MIRACLS

5.1 Purpose of a 30-keV MR-ToF Device

Like conventional CLS, MIRACLS aims to work with ion beam energies of more than 30 keV such that the spectral resolution of the CLS spectra approaches the natural linewidth. However, all MR-ToF devices built so far utilize ion beam kinetic energies around a few kiloelectronvolts and mirror potentials of less than 8 kV [2, 45, 65, 66, 77, 88, 90, 93]. Therefore a completely new MR-ToF device with mirror potentials of up to 60 kV has to be envisioned, such that the future MIRACLS' MR-ToF device will be worldwide the first one to confine an ion beam with a kinetic energy of 30 keV. Thus, in addition to improving the experimental sensitivity of traditional high-resolution CLS by a factor of 40 to 700 (see chapter 3.4.2) this MR-ToF advances will also offer new opportunities for mass separation of rare isotopes.

According to simulations presented in this chapter mass resolving powers of $R > 10^5$ can be reached within hundreds of microseconds with the 30-keV MR-ToF device. For comparison, MR-ToF devices that exist so far need typically some (tens of) milliseconds to reach this mass resolving power (see figure 3.6). At this time, the fastest MR-ToF mass separation is reported in [19] where a mass resolving power of $R = 10^5$ was achieved for $^{133}Cs^+$ in 1.7 ms. At certain ion densities repulsive Coulomb interactions between the ions can not be neglected anymore and due to these so-called space-charge effects it is not possible to store large numbers of ions in a MR-ToF device while maintaining the high mass resolving power, see e.g. [72]. At this time, maximally $1.2 \cdot 10^6$ ions are mass separated per second with a mass resolving power of $R > 10^5$ from 50,000 isobaric ions per second, as reported in [18] for a mass of 78 u. If the mass separation process was much faster more ions of interest could be mass separated from their contaminants per time unit even when the number of ions stored at a time was well below the space-charge limit. A 30-keV MR-ToF device would thus be advantageous for a wide range of experimental programs at ISOLDE. Indeed, the sensitivity of many of the experimental setups would already be high enough for the measurement of nuclides far away from stability if their operation would not be compromised by overwhelming isobaric contamination.
Even applications close to stability like the production of innovative medical isotopes suffer from isobaric contamination. For instance, a 30-keV MR-ToF device would be highly beneficial for the separation of Terbium isotopes from the isobaric impurities (Gd, Eu) and oxide sidebands. At the moment a chemical separation at the Paul Scherrer Institute is carried out, that is 280 km away from ISOLDE, where the Terbium isotopes are produced. Terbium isotopes promise excellent properties for diagnostic and therapeutic applications [16, 58]. A high amount of radioactive material has to be transported, handled during the chemical separation and the generated radioactive waste has to be disposed. A fast mass separation of a large amount of ions (ion current of hundreds of pA of incoming beam, corresponding

to 10^9 ions/s) with a mass resolving power of $R > 10^5$ would make the chemical separation redundant and hence reduce the radioactive activity during transport and handling as well as radioactive waste.

5.2 Design of a Prototype for the 30-keV MR-ToF Device

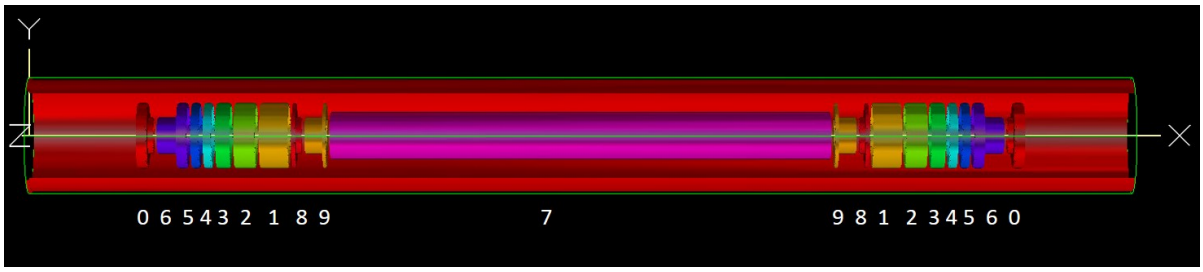

Figure 5.1: Design of the 30-keV MR-ToF device. Some parts of the outer grounded tube are removed to show the interior. The electrodes are marked with numbers: 0: grounded electrode to prevent fields from outside reaching into the MR-ToF device, 1-2: two inner mirror electrodes ensuring radial ion refocusing, 3-6: four outer mirror electrodes for axial confinement, 7: in-trap lift, 8: grounded electrode to shield the in-trap lift region from electric fields from the mirrors, 9: pick-up electrodes or deflector electrodes.

MIRACLS' aim is to build a prototype for a 30-keV MR-ToF device that can be used for both, CLS and mass separation. After testing the prototype in CLS and mass separator mode, a separate MR-ToF device for mass separation and/or CLS can be built based on the experience obtained by testing the prototype. However, there exists a few technical challenges for a 30-keV MR-ToF device. Firstly, to minimize aberration effects of the mirror electrodes that would lead to a degrading of the mass resolving power and likely also to a worse CLS line shape and ion-laser overlap, high voltage power supplies with a stability of a few parts per million are required. Secondly, high voltage breakdowns might occur between neighbouring electrodes of which one is for instance biased to 60 keV and the other electrode right next to it to -40 keV. Hence, excellent vacuum properties of 10^{-10} mbar or better will be essential. According to [46] and [33] the breakdown voltage of two stainless steel plates with a distance of 5 mm between them is larger than 100 kV if the two stainless steel plates are in UHV. There also exists polyethylene insulators with a breakdown voltage of 90 kV/mm [85]. Moreover, it is important that all the corners of the MR-ToF device are rounded off to avoid field emission points along which a voltage breakdown could proceed. However, prior to the construction of such a device, a first design of the 30-keV MR-ToF has to be made and its performance for mass separation and CLS has to be tested in simulations.

The goal of this chapter is to envision a MR-ToF device, where ions with a kinetic energy of 30 keV can be stored. Moreover, this MR-ToF device should meet all the requirements for CLS such as high ion-laser overlap and a narrow linewidth of the CLS spectra and ideally it should also have a high mass resolving power $R > 10^5$ for its later use as a prototype for a fast mass separator device. Even in CLS mode, a reasonably good mass resolving power is important to keep the bunched beam structure and therefore reduce the CLS background due to the laser-stray light (see chapter 2.3).

The design of MIRACLS' 30-keV MR-ToF device is based on the Greifswald MR-ToF device, operating at an ion beam kinetic energy of around 1.3 keV [25, 26]. However, the lengths and inner diameters

of several electrodes are changed and more shielding electrodes are added. A schematic drawing of the prototype of MIRACLS' 30-keV MR-ToF device can be seen in figure 5.1. The MR-ToF device consists of two opposing electrostatic mirrors with a central drift tube (electrode 7) in between. One electrostatic mirror is made out of six mirror electrodes (1-6). The two mirror electrodes (1-2) that are closest to the central drift tube ensure radial refocusing of the ions. The axial trapping potentials is realized by four outer mirror electrodes (3-6). Between the central drift tube and the mirror electrodes a grounded shielding electrode (8) and a pick-up or deflector electrode (9) is installed. Electrode 8 shields the central drift tube region from electric fields from the mirror electrodes. Moreover, the inner diameter of electrodes 7-9 is reduced to 40 mm compared to the inner diameter of the mirror electrodes of 80 mm, hence providing a large field-free region in the central drift tube. Electrode 9 can be used as pick-up electrode or deflector electrode, if it is azimuthally segmented (see chapter 3.3.2.3).

Given the sensitivity of the ions' trajectories to field distortions at their turn-around point, the outermost mirror electrode 6 is reduced at its outer end to an inner diameter of 40 mm to shield the MR-ToF region from electric fields from outside. The turn-around point of the ions itself is at the position of electrode 6 at the part with an inner diameter of 80 mm or at position of electrode 5, depending on the velocity of the ions as well as the applied MR-ToF mirror potentials. Grounded electrodes (0) before and after the MR-ToF device provide an additional shielding from fringe fields. An einzel lens with a potential of either 60 kV or -60 kV is added before the MR-ToF device (see figure 5.2) to investigate its fringe fields into the MR-ToF region. For the set of potentials given in table 5.2 (left column, potential combination 1) the potential difference between 0 V and ±60 kV applied to the middle electrode of the einzel lens is at the maximum of the electric potential distribution along the central axis of the MR-ToF device at ~ -557.5 mm less than ±0.2 V (see figure 5.2). Note that the turn-around point of the ions is ~ 25.5 mm away from this potential maximum where the potential difference is even smaller. Therefore one can conclude, that the MR-ToF region is reasonably well shielded from fringe fields.

The lengths of all the electrodes as well as their possible potential ranges can be found in table 5.1. All gaps between the electrodes have a distance of 5 mm and all corners are rounded off to prevent high voltage breakdowns. Due to the fact that one row of PMTs needs a space of 200 mm [43] and three rows of PMTs are planned the ODR has a length of ~ 600 mm. This region should be field-free as will be discussed in chapter 5.3.6. Hence, the length of the central drift tube is found to be 690 mm.

Table 5.1: lengths and allowed potential range of the electrodes of the 30-keV MR-ToF device

number of electrode	name of electrode	electrode length / mm	potential /kV
0	shielding electrode	22.4	Ground
1	mirror electrode 1 (ME1)	40.0	−60 <ME1< 0
2	mirror electrode 2 (ME2)	30.0	−60 <ME2< 0
3	mirror electrode 3 (ME3)	20.0	0 <ME3< 60
4	mirror electrode 4 (ME4)	12.0	0 <ME4< 60
5	mirror electrode 5 (ME5)	12.0	0 <ME5< 60
6	mirror electrode 6 (ME6)	42.4	0 <ME6< 60
7	central drift tube (lift)	690.0	0 <lift< 60
8	shielding electrode	12.5	Ground
9	pick-up or deflector electrode (defl)	30.0	

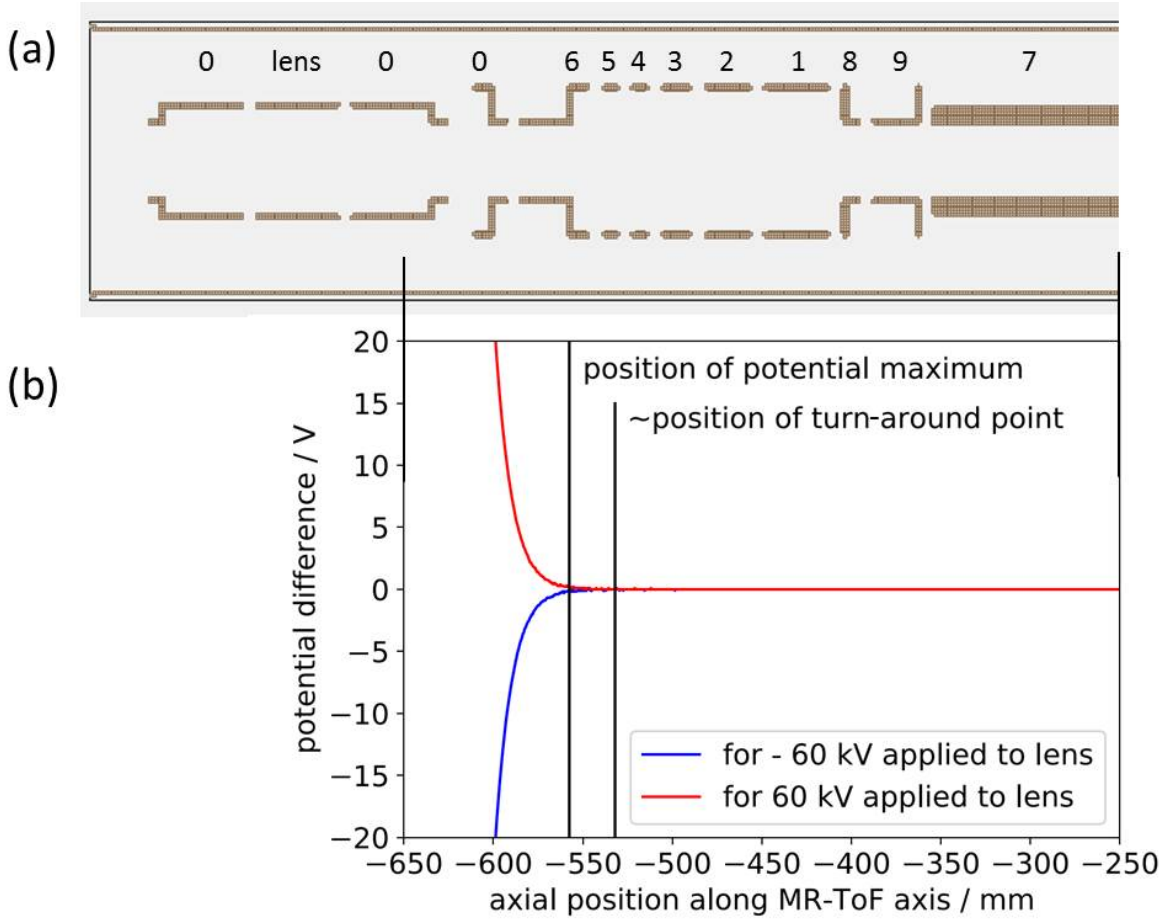

Figure 5.2: (a) An einzel lens with a potential of either 60 kV or -60 kV is added before the MR-ToF device to investigate its fringe fields into the MR-ToF region. (b) Potential difference between ±60 kV and 0 V applied to the lens along the central axis of the MR-ToF device. The position for the potential maximum and the position of the turn-around point are marked with black lines. Note, that the exact position of the turn-around point depends on the velocity of the ions (here $A = 24$ u, $E = 30$ keV, $\sigma_E = 1$ eV). The potential difference is shown for potential combination 1 given in table 5.2.

5.3 Simulations of the Ions' Trajectories in the 30-keV MR-ToF Device

All the simulations in this section are carried out with SimIon, version 8.1.1.32 [17, 81]. Note, that Coulomb interactions between the different ions and between ions and image charges on the electrodes are not taken into account. As was shown experimentally space-charge effects can be neglected if only few ions are stored in a MR-ToF device, see e.g. [72]. So all the simulations here are valid for the MR-ToF device in CLS mode, where anyhow only a very little number of ions is confined at the same time. For the MR-ToF device as a fast mass separator dealing with a large incoming beam intensity the results of the simulations presented here can be taken as a starting point for the investigation of space-charge effects in experiment or simulation.

5.3.1 Starting Distribution

The ions are started in the axial middle plane of the MR-ToF device all at the same time. Note that in reality, the ions already have some time spread when reaching the middle plane of the MR-ToF device, that is neglected here. The radial deviations of the ions' positions from the MR-ToF axis x are in the transversal y and z directions Gaussian distributed with a mean of 0 mm and a standard deviation of $\sigma_z = \sigma_y$, respectively. Also the azimuthal (az) and elevation (el) angles for each ion are Gaussian distributed with a mean of 0 degree and the standard deviations, $\sigma_{\mathrm{az}} = \sigma_{\mathrm{el}}$. The kinetic energy E of the ions is Gaussian distributed with a mean of 30 keV and a standard deviation of $\sigma_E = 1$ eV, if not stated differently. All the ions are singly-positively charged. If not stated differently the mass of the ions is 24 u and the resonance frequency f_0 in the rest frame of the $^{24}Mg^+$ ions is 1,072,082,934.33 MHz in the D2 line [6]. Note that the transversal rms emittance of ISCOOL is reported to be 2π mm mrad [22], but most of the simulations presented in the following are done with a rms emittance of around 3π mm mrad to consider a worst-case scenario. Due to the fact that only conservative forces are applied between ejection from the Paul trap and injection into the MR-ToF device the transversal emittance remains constant. However, with the help of einzel lenses, quadrupole-focusing elements and other ion-optical devices it is possible to in-/decrease the angular divergence by de-/increasing the spatial width of the beam. Therefore different values of σ_y and σ_{az} can be chosen for a constant transversal rms emittance. This starting distribution is considered to lead to a realistic ion distribution. It is quite the same as the ion distribution in the middle plane of the PoP MR-ToF device obtained after 40 revolutions (see chapter 4.4) for the scenario where the ions are thermalized in the Paul trap before their injection into the MR-ToF device.

5.3.2 Search for Optimal Mirror Potential Combinations

In order to identify suitable combinations for mirror potentials for CLS, a guided Monte Carlo Approach similar to the one explaind in chapter 4.4.2 is employed utilising the ion starting distribution described above with a rms emittance of 3π mm mrad with $\sigma_y = 1$ mm and $\sigma_{\mathrm{az}} = 0.175$ degree, a kinetic energy of 30 keV and an energy spread of 1 eV. Less sets of suitable mirror potentials are found compared to the Monte Carlo Approach for the PoP experiment. This may be due to the higher ratio of beam energy (30 keV) to maximal available mirror potential (60 kV). Hence, to speed up the simulation only 50 ions are created in the middle plane of the MR-ToF device. A random combination of electric potentials applied to the mirror electrodes ME1-ME6 is chosen. The mirror potentials have to be in a certain

range as given in table 5.1 due to the chosen power supplies. Moreover, to reduce the complexity of the system the potential of the first mirror electrode ME1 is chosen identically to the one of the second mirror electrode ME2.
In figure 5.3 the randomly chosen combinations of mirror potentials which lead to a trapping efficiency of 100% for 20 revolutions in the MR-ToF device are shown. Each point corresponds to one potential combination that is characterized according to the mass resolving power, the Doppler width and the ion-laser overlap assuming a laser-beam diameter of 4 mm. The global behaviour is quite similar to the results of the Monte Carlo approach for the PoP experiment and is discussed in detail there (see chapter 4.4.2). For the chosen energy spread of 1 eV, the calculated Doppler width for ions propagating parallel to the MR-ToF axis with a kinetic energy of 30 keV (Doppler limit σ_f) is $\sim$ 30 MHz. In principle this should be the smallest attainable Doppler width for any potential combination. However, a correlation between the kinetic energies and the angles between ion paths and MR-ToF axis leads to a compression in the resonance frequencies in the lab frame as explained in chapter 4.4.
Out of all the found sets of mirror potentials leading to 100% of trapping efficiency, only a small fraction of potential combinations is suitable for CLS, i.e. in which the ion-laser overlap is over 80% and the Doppler width is approaching the Doppler limit.

Figure 5.4 shows the results of the Monte Carlo approach for three different transversal emittances with a different angular distribution but always the same radial spatial distribution. The energy spread is for all the shown transversal emittances the same with $\sim$1 eV. Due to the larger angles between ion path and MR-ToF axis the Doppler width is larger for the higher emittances. This illustrates the importance of a small transversal emittance for MIRACLS. In principle, the claimed transversal rms emittance of ISCOOL of 2π mm mrad would be enough for good CLS results in a MR-ToF device. However, if the transversal emittance is further improved, the same linewidth will be obtained with a smaller spatial width of the ion beam. Then, a smaller laser-beam diameter can be chosen that still excites most of the ions, which will make it easier to deal with laser-stray light.

As one can see in figure 5.3 there exists mirror potential sets leading to mass resolving powers of over $R > 10^5$, that are reached in the simulation within the first 20 revolutions so within 100 μs (when assuming that all the ions start at the same time in the middle plane of the MR-ToF device). By choosing one specific set of mirror potential and optimizing it by employing a Simplex Optimizer already implemented in SimIon the mass resolution can even be further optimized by up to a factor of 25. However, the sets of mirror potentials with the highest achievable mass resolving powers found so far are not suitable for CLS due to a severe reduction of the ion-laser overlap as well as an increase in the Doppler width. Due to the fact that there exists optimal potential combination for CLS and other optimal potential combinations for mass spectrometry the same device can be used for CLS measurements as well as for a fast mass spectrometer by only changing the mirror potentials. Note that the Simplex Optimizer used for the optimization of the mass resolving power is not very useful for finding optimal potential combinations for CLS due to the connection between ion-laser overlap and Doppler width because of the conserved transversal emittance, therefore the Monte Carlo approach is chosen.

The Monte Carlo simulations described in this chapter are done with a slightly different electrode structure as explained in chapter 5.2. The elongation part of mirror electrodes 6 with the reduced inner diameter and the grounded shielding electrodes 0 are missing. Due to the fact that in these simulations the ions start in the middle plane of the MR-ToF device and the einzel lens is not considered, it is

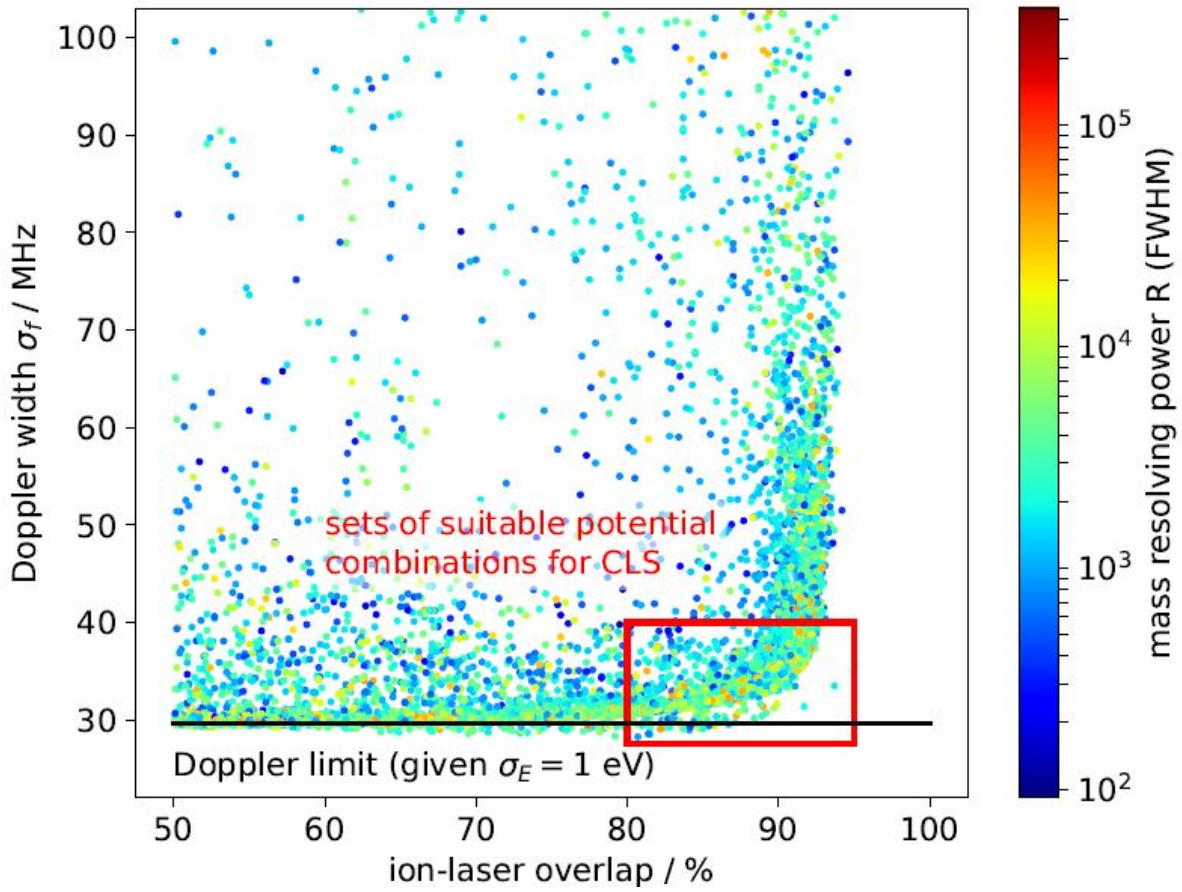

Figure 5.3: Doppler width σ_f and mass resolving power R (FWHM) versus the ion-laser overlap for different combinations of electric potentials of the MR-ToF mirrors as probed in the Monte Carlo approach. Note, that there exists potential combinations outside of the shown range with a Doppler width of up to 530 MHz. The chosen transversal rms emittance of the starting parameters is 3 π mm mrad ($\sigma_y = 1$ mm, $\sigma_{\mathrm{az}} = 0.175$ degree).

expected that those geometrical differences do not have any significant impact on the ions' trajectories in the MR-ToF device. By comparing the results of two simulations with the same set of mirror potentials as well as the same ion distribution it could be shown that the slightly different geometry indeed is not affecting the simulated results.

The results discussed in all the other following chapters are obtained by taking the exact MR-ToF geometries for the electrode structure as explained in chapter 5.2.

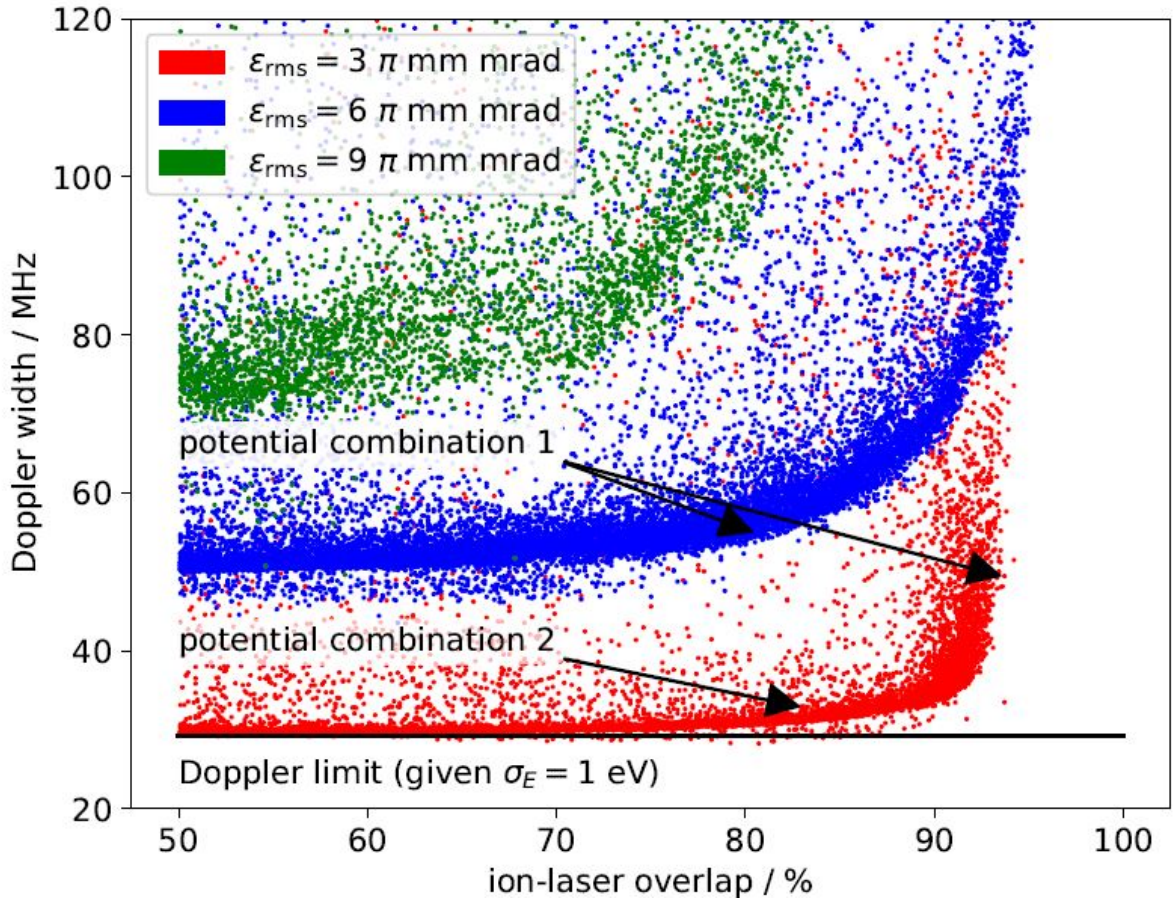

Figure 5.4: Doppler width σ_f versus the ion-laser overlap for different combinations of electric potentials of the MR-ToF mirrors as probed in the Monte Carlo approach shown for three different transversal rms emittances ϵ_{rms}. The radial distances from the MR-ToF axis are the same with $\sigma_y = 1$ mm, whereas the angular distribution is varied with a σ_{az} to obtain a transversal rms emittance of either 3π mm mrad, 6π mm mrad or 9π mm mrad. Note, that there exists potential combinations outside of the shown range.

5.3.3 Testing of Specific Potential Combinations

Two sets of mirror potentials with a good compromise in ion-laser overlap, Doppler width, and a reasonable mass resolving power are taken from the datasets obtained from the Monte Carlo approach. High mass resolving power is equivalent to short ion bunches which leads to high signal-to-noise ratios when gating the photon counting on the passage of the ion bunch. Moreover, in the choice of potential sets it is assured that the difference in electrice potentials between neighbouring electrodes is less than 40 kV, to minimize the risk of HV sparking between two electrodes. The mirror potentials for these two sets can be seen in table 5.2 and the respective potential distribution along the MR-ToF axis is shown in figure 5.5. Potential combination 1 originates from the Monte Carlo results for a rms emittance of 6π mm mrad and potential combination 2 is taken from the Monte Carlo results for a rms emittance of 3π mm mrad.

Table 5.2: Chosen potential combinations for the MR-ToF device electrodes (ME1 is the mirror electrode closest to the central drift tube, ME6 is the outermost mirror electrode).

respective electrode	potential combination 1 potential / V	potential combination 2 potential / V
ME1	-12469.3	-10106.2
ME2	-12469.3	-10106.2
ME3	23002.6	9656.9
ME4	25966.4	39535.0
ME5	29648.9	26335.9
ME6	39013.0	44726.4

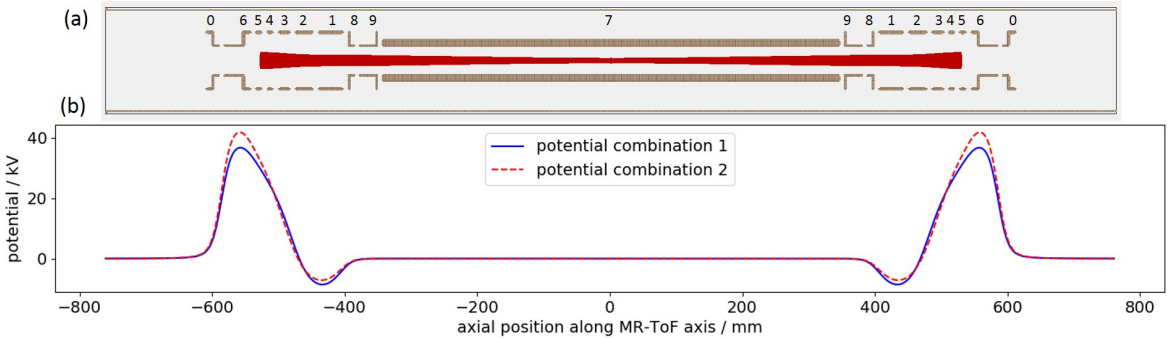

Figure 5.5: 30-keV MR-ToF device: (a) Cut view of its electrode structure together with the simulated ions' trajectories (in red) for 500 ions performing 100 revolutions in the MR-ToF device and for potential combination 1. (b) Electric potential distribution along the central axis of the MR-ToF device for the two different sets of mirror potentials 1 and 2.

The ions' trajectories are simulated once more for potential combination 1 and the starting distribution with a rms emittance of 3π mm mrad to confirm that a potential combination selected from the simulation with a higher emittance also leads to good results for a smaller emittance (see table 5.3 and figure 5.4). Generally, ion-laser overlap and Doppler width are both better for the smaller transversal

rms emittance. However, there exist even better sets of mirror potentials for the smaller transversal rms emittance (see figure 5.4), especially when considering the Doppler width.

Table 5.3: CLS-relevant simulation results for the potential combination 1 once for a starting distribution of 3π mm mrad and once for a starting distribution of 6π mm mrad. In both cases $\sigma_y = 1$ mm.

starting distribution	ion-laser overlap	Doppler width σ_f
6π mm mrad	80.4	55
3π mm mrad	93.6	49.4

With the help of einzel lenses, quadrupole-focusing elements and other ion-optical devices before the MR-ToF device it is possible to in-/decrease the angular divergence by de-/increasing the spatial width of the beam while the transversal emittance of the beam keeps constant. The angular divergence is given by σ_{az} and the spatial width by σ_y. To investigate the effect of those different transformations of phase space for a constant rms emittance of either 3π mm mrad or 6π mm mrad on the CLS-relevant parameters, different starting distributions (so different σ_{az} and different σ_y for the constant emittance) of 500 ions each are simulated in the MR-ToF device, where once potential combination 1 and once potential combination 2 is applied to the mirror electrodes. Ion-laser overlap and Doppler width for the starting distribution can be seen in figures 5.6(b) and 5.6(d) with a constant transversal emittance of 6π mm mrad and 3π mm mrad, respectively. The starting distribution for the simulation of the ions' trajectories in the MR-ToF device is per construction unrelated to the MR-ToF device. Hence, its evaluation in terms of ion-laser overlap and Doppler width can be interpreted as how traditional CLS would perform based on such an ion distribution. In this regard, the ion-laser overlap for a small spatial width of the beam σ_y is close to 100% and decreases with increasing spatial width as expected. For small angular divergences σ_{az} the Doppler width is close to the natural linewidth of ~ 30 MHz and increases with increasing angular divergence. For comparison at COLLAPS, the maximal angle the ions can have, is given by two aperture sets with a distance of 1.5 m where the first aperture has an inner diameter of 6 mm and the second one of 10 mm. Ions with an angle larger than 0.3 degree therefore hit the apertures and do not make it into the ODR [9].
To see the effect of the reflections at the MR-ToF mirrors on the Doppler width and ion-laser overlap, 100 revolutions of the ions in the MR-ToF device are simulated for the different starting parameters, σ_y and σ_{az}. Once again, the ion distribution is recorded for each revolution when the ions pass the transversal middle plane in the direction of the laser-beam propagation. From this data, the Doppler width, the ion-laser overlap and the mass resolving power is calculated, see figure 5.6(a) for the potential combination 1 and a rms emittance of 6π mm mrad, figure 5.6(c) for the potential combination 1 and a rms emittance of 3π mm mrad and figure 5.6(e) for a rms emittance of 3π mm mrad and potential combination 2. For figures 5.6(c) and 5.6(e) the same starting distribution is used that can be seen in figure 5.6(d). Here, even for small spatial widths of the incoming ion beam the ion-laser overlap is not 100% for all the 100 revolutions in the MR-ToF device. This is a consequence of a redistribution of the ion cloud due to the reflections at the MR-ToF mirrors, e.g. the spatial width is increased whereas the angular divergence is decreased. Therefore the Doppler width when considering all 100 revolutions is smaller for lower values of σ_y compared to its evaluation of the ions' starting distribution.
For small values of σ_{az} the Doppler width would be close to the natural linewidth without any revolution in the MR-ToF device, but due to the reflections at the mirrors the angles are increased and lead to

a sizeable Doppler width even for a small initial angular divergence. Due to the constant transversal emittance the ion-laser overlap for small values of σ_{az} is better for all the 100 revolutions compared to its value of the starting distribution alone.
There exists a specific combination of angular divergence and spatial width leading to a maximum in ion-laser overlap and to a minimum in the Doppler width, slightly above the natural linewidth. Naturally given this particular emittance and mirror potentials, this is the preferred orientation in phase space as it should be sought in CLS operation. Fortunately, also the mass resolving power is over 10,000 for this specific transformation of phase space and 100 revolutions.

Potential combination 2 leads for the same starting distribution to a smaller Doppler width and to a factor of 2 better mass resolving power compared to potential combination 1 while maintaining a good ion-laser overlap (see figures 5.6(e) and 5.6(c)). However, for potential combination 1 the trapping efficiency for σ_y between 0.5 and 2.5 mm is 100%, whereas for potential combination 2 this is just the case for $\sigma_y = 1$ mm. For smaller or higher values of σ_y the trapping efficiency can even drop below 80% (see figure 5.6(f)).

These results show that a well controlled beam injection into the MR-ToF device is of utmost importance. Even for the same transversal emittance the Doppler width, ion-laser overlap and mass resolving power differ significantly for different transformations of the phase space. Hence, simulating the injection from MIRACLS' Paul trap into the MR-ToF device will be subject of future work.

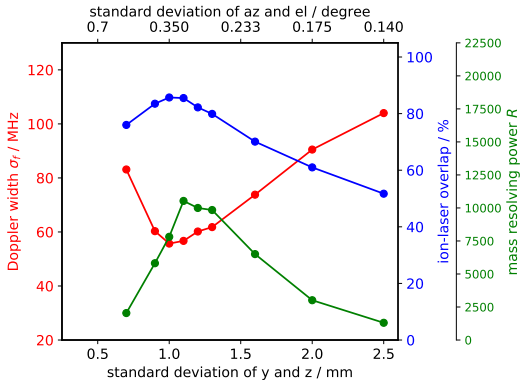

(a) Potential Combination 1, $\epsilon_{\mathrm{rms}} = 6\pi$ mm mrad, 100 revolutions

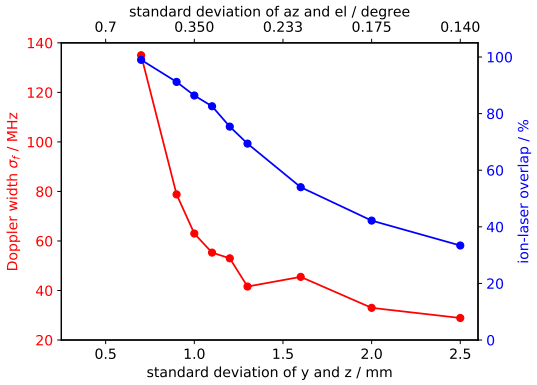

(b) $\epsilon_{\mathrm{rms}} = 6\pi$ mm mrad, starting distribution

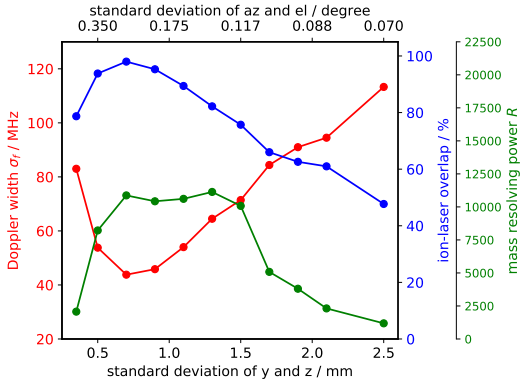

(c) Potential Combination 1, $\epsilon_{\mathrm{rms}} = 3\pi$ mm mrad, 100 revolutions

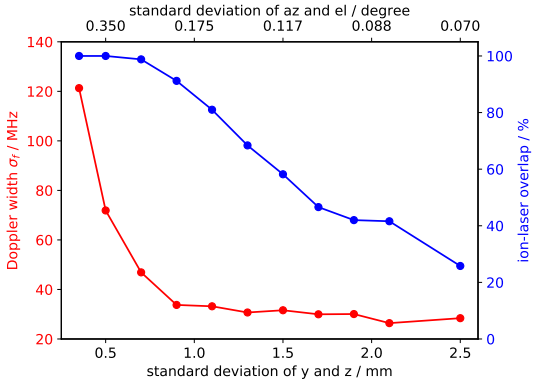

(d) $\epsilon_{\mathrm{rms}} = 3\pi$ mm mrad, starting distribution

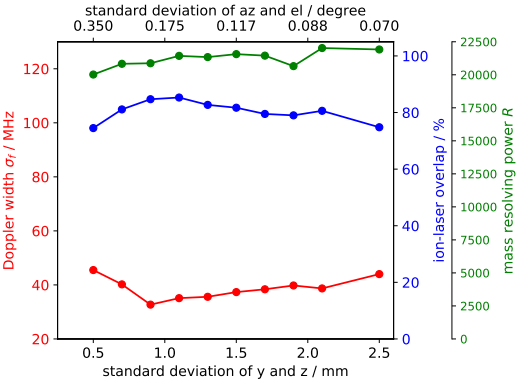

(e) Potential Combination 2, $\epsilon_{\mathrm{rms}} = 3\pi$ mm mrad, 100 revolutions

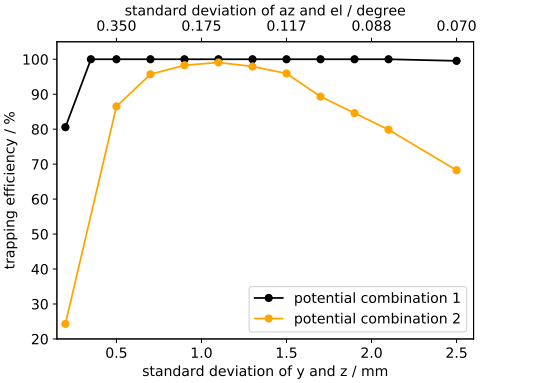

(f) trapping efficiency for potential combination 1 and 2, $\epsilon_{\mathrm{rms}} = 3\pi$ mm mrad, 100 revolutions

Figure 5.6: (a,c,e): Doppler width, ion-laser overlap and mass resolving power for different starting parameters (transformation of phase space with a constant rms emittance of 3 or 6 π mm mrad) for two different potential combinations 1 and 2 evaluated for 100 revolutions in the MR-ToF device. (b,d): Doppler width and ion-laser overlap for different starting parameters (transformation of phase space with a constant rms emittance of 3 or 6 π mm mrad) recorded directly at the start of the ions. This corresponds to the performance of conventional CLS for the respective ion distribution. (f): trapping efficiency for different starting parameters (transformation of phase space with a constant rms emittance of 3 π mm mrad) for two different potential combinations 1 and 2 evaluated for 100 revolutions in the MR-ToF device. A diameter of the laser beam of 4 mm is assumed, and the Doppler width is given for only the laser-excited ions, so for the ions which radial distances from the MR-ToF axis are less than 2 mm.

5.3.4 Comparison Between the Starting Distribution and the Ion Distribution Obtained for 200 Revolutions

For a further investigation of the influence of the ions' reflections at the MR-ToF mirrors on CLS-relevant parameters, the starting distribution leading to the highest ion-laser overlap and the smallest Doppler width ($\sigma_y = 0.7$ mm and $\sigma_{\mathrm{az}} = 0.25$ degree) is compared to the results obtained for 200 revolutions in the MR-ToF device with potential combination 1 in the following (see table 5.4). As mentioned before the results for the starting distribution are seen as the performance of traditional CLS. The phase space and the radial distances of the ions in y an z to the central axis x of the MR-ToF device are shown in figure 5.7. Here, in the left column the chosen starting distribution is shown and in the right column all 200 revolutions are taken into account. For both cases, a laser beam with a diameter of 4 mm can interact with 98% of the ions.

Exemplary for all simulated ions, sample ions are tracked for 2000 revolutions as they move in regular pattern through the MR-ToF device's transversal middle plane (see figure 5.8). In figure 5.8(a) the ion distribution in the sub space (y, y') of two ions with different starting parameters is shown and in figure 5.8(b) the corresponding radial distances from the MR-ToF axis for each of the two ions. Sample ion 1 can always be excited by a laser beam with 4-mm diameter, whereas sample ion 2 can for some revolution numbers be excited by the laser and for others not. The angles between flight trajectories and MR-ToF axis as well as the radial deviations from the MR-ToF axis show a periodic behaviour versus revolution number (see figures 5.8(c) and 5.8(d)). Most of the investigated ions show a similar behaviour as sample ion 1. Whereas for Paul traps there exists an analytical description of the ion's motion, such a description is still missing to our knowledge for a MR-ToF device. For CLS in a MR-ToF device, the periodic motion of an ion between the two electrostatic mirrors is quite beneficial because that means that the Doppler width and the centroid is fluctuating around an average value and not increasing with higher revolution numbers (see chapter 5.3.5). However, a redistribution between the angles α and radial distances from the MR-ToF axis takes place, meaning for one revolution number the angle is smaller and the radial distance is larger whereas for an other revolution number this is vice versa (see figures 5.8(c) and 5.8(d)).

A histogram of the energy, the angles between ion paths and MR-ToF axis and of the Doppler shifted frequencies f can be seen in figure 5.9, where the left column shows the results for the starting distribution and the right column the results for 200 revolutions in the MR-ToF device. Considering the simulated 500 ions and a laser-beam diameter of 4 mm, the Doppler width of the D2 transition of the $^{24}Mg^{+}$ ions summed over 200 revolutions is due to the energy spread of 1 eV and the angles between ions' trajectories and laser beam 43.9 MHz compared to the Doppler limit of 30.6 MHz. A non-vanishing angle between ions' trajectories and laser-beam axis will always shift the laser frequency observed in the ion's rest frame according to equation 4.4 in one direction, i.e to lower values for collinear laser spectroscopy. This results in an asymmetric line shape as well as in a shift of the average Doppler shifted frequency of ~ 40 MHz. However, by comparing figures 5.9(e) and 5.9(f) it is apparent that this shift and asymmetry is also present when exclusively considering the starting distribution. Note that such a 40-MHz shift in the absolute frequency of the centroid is not a cause for concern in CLS provided that all measured isotopes are shifted by the same amount, i.e. that this shift is (to first order) mass independent. Future simulations can study this in more detail. The red histogram shows the Doppler shifted frequencies f assuming the Doppler limit ($\alpha = 0$ degree) and the blue histogram takes the actual angular distribution of the ions into account. The blue and red dashed lines show a Gaussian line shape

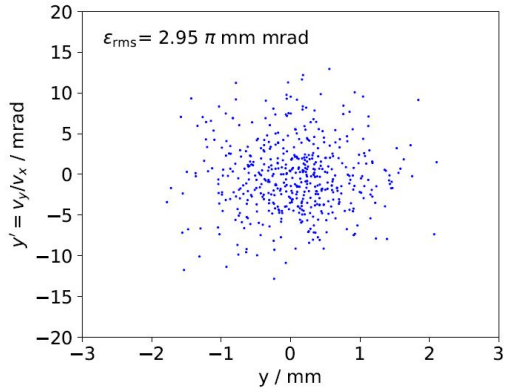

(a) start, transversal emittance in sub space (y, y')

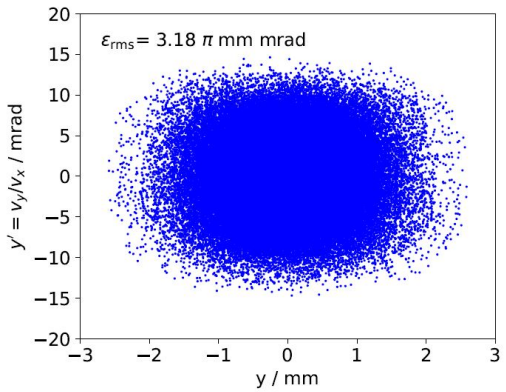

(b) 200 rev, transversal emittance in sub space (y, y')

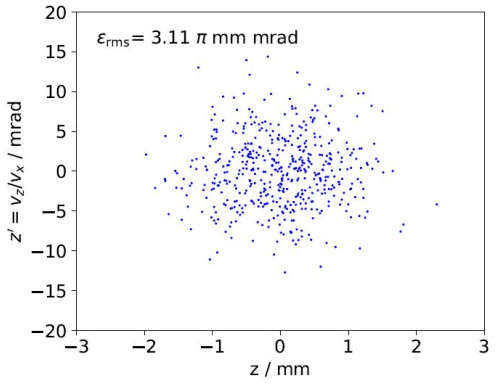

(c) start, transversal emittance in sub space (z, z')

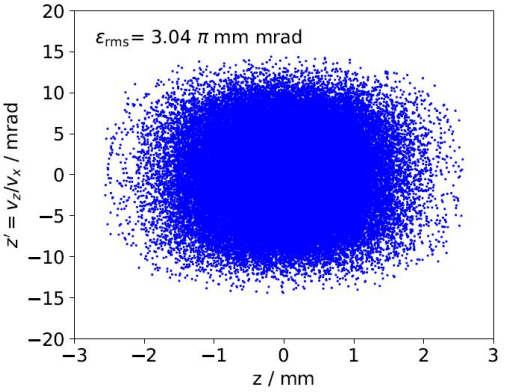

(d) 200 rev, transversal emittance in sub space (z, z')

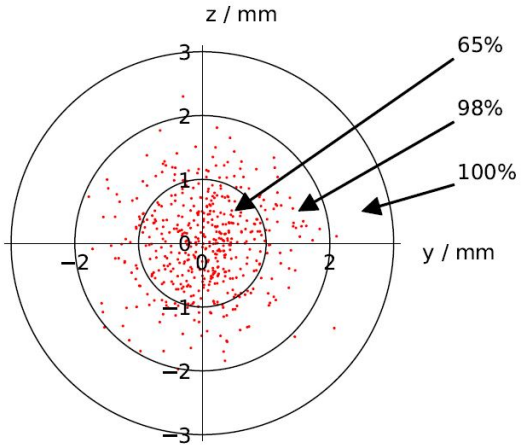

(e) start, ion-laser overlap

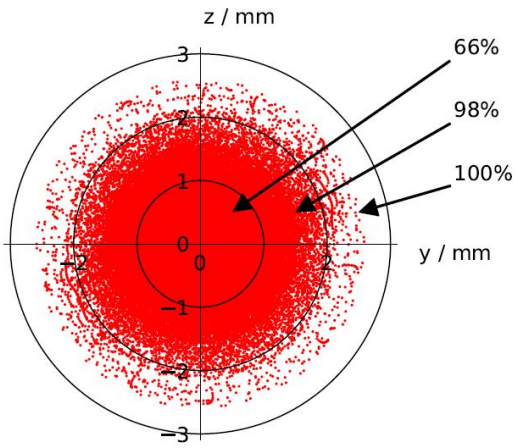

(f) 200 rev, ion-laser overlap

Figure 5.7: Comparison of the starting distribution of the ions in the middle plane of the MR-ToF device ($\sigma_y = 0.7$ mm, $\sigma_{\mathrm{az}} = 0.25$ degree and $\sigma_E = 1$ eV, left column) with the results of 200 revolutions in the MR-ToF device (right column). See text for details.

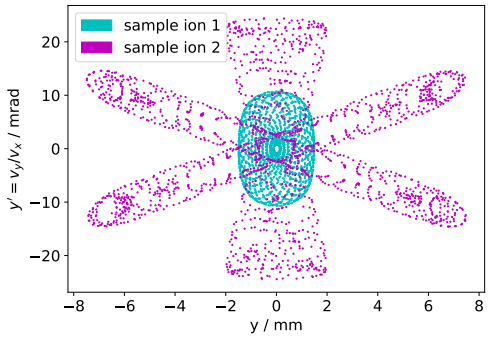

(a) sample ion 1 and 2

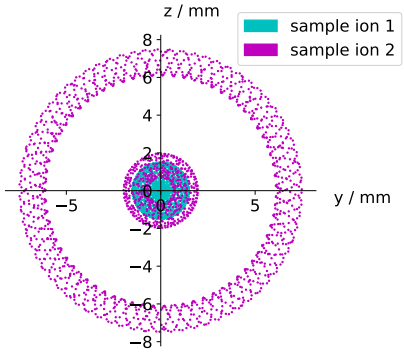

(b) sample ion 1 and 2

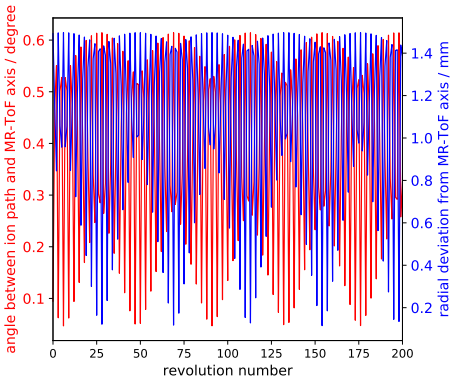

(c) sample ion 1

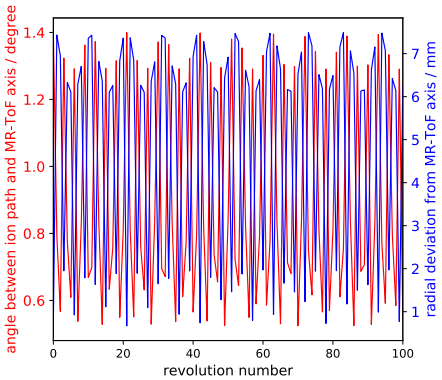

(d) sample ion 2

Figure 5.8: Ion distribution in the (y, y') subspace (a) and radial deviation from the MR-ToF axis (b) for two selected sample ions with different starting parameters for 2000 revolutions. (c,d) Radial deviation from the MR-ToF axis (blue) and angle between ion path and MR-ToF axis (red) for sample ion 1 (c) and sample ion 2 (d). Most of the ions that are investigated show a similar behaviour as sample ion 1.

with centroid and mean extracted from the data to illustrate the slight shape asymmetry of the line shape obtained when taking the angular distribution into account.

The time spread of the ions σ_t increases linearly with revolution number and is for 200 revolutions 20 ns (see figure 5.10). Note that in reality the initial time spread of the ion cloud is of course different from 0 as assumed here. Since the initial time spread is not yet known from MIRACLS' Paul trap simulation or experimental operation, the following discussion on σ_t is meant to indicate the consequences of its increase over storage time.
The revolution time for $^{24}Mg^+$ ions is around 4.9 μs. To keep a bunched structure of the beam in the MR-ToF device the time spread has to be smaller than half of the time for one revolution, so lower than ~ 2.4 μs. This is for a mass of 24 u the case for up to 24,000 revolutions, corresponding to a trapping time of ~ 118 ms. This compares favourably to the half-lives $T_{1/2}$ of the first science cases of MIRACLS ^{20}Mg ($T_{1/2} = 91$ ms) and ^{34}Mg ($T_{1/2} = 20$ ms) even when the trapping time leading to the highest improvement factor in sensitivity is 1.8 $T_{1/2}$ as discussed in chapter 3.4.2. Similar studies will be done for the case of $^{96}Cd^+$ in which the half life is 1 s and the time for one revolution is around 10 μs. Hence, the ions should be trapped for more than 180,000 revolutions to obtain the highest signal-to-noise ratio. Moreover, it has to be better understood why in the PoP experiment the slope of the experimental time spread is lower than the simulated one (see chapter 4.4.4.3). Furthermore, in the PoP experiment it has been shown that the dispersions per turn vary for different kinetic energies of the ion bunch as discussed in chapter 4.4.4.3. Consequently, it may be possible to minimize the increase in the temporal bunch width over revolution number in future studies for an optimized experimental sensitivity. Thus, the increase of the time spread over revolution number will not be a show-stopper for MIRACLS.

A summary of the CLS-relevant parameters for the starting distribution and for taking all the 200 revolutions into account is given in table 5.4. Apart from the increase of the time spread due to the dispersions per turn in the MR-ToF device, the CLS-relevant parameters for 200 revolutions in the MR-ToF device are quite the same as for the starting distribution, providing confidence that line shape distortions due to the MR-ToF characteristics are well under control if the mirror potentials and injection optics into the MR-ToF device are appropriately chosen.

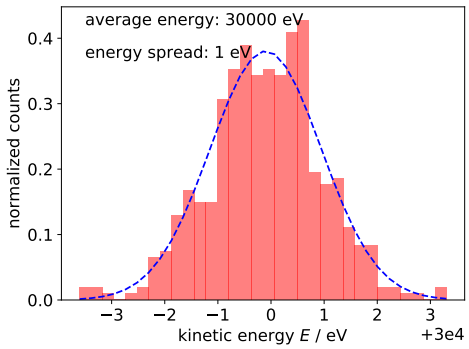

(a) start, kinetic energy

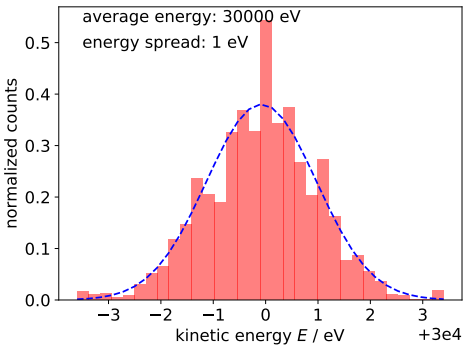

(b) 200 rev, kinetic energy

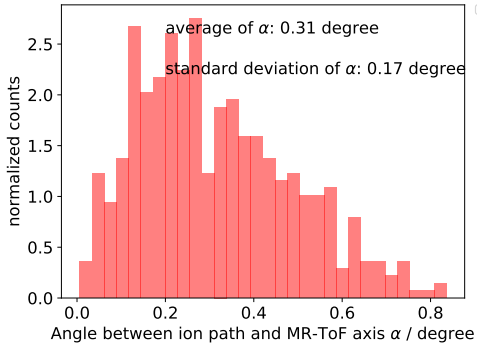

(c) start, angular distribution

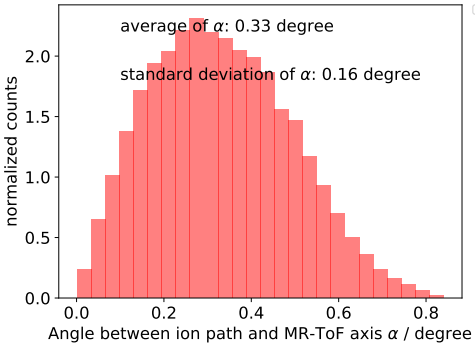

(d) 200 rev, angular distribution

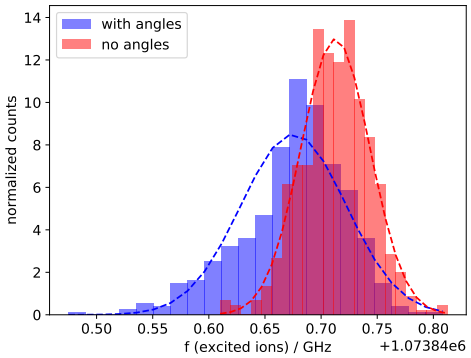

(e) start, Doppler shifted frequency f

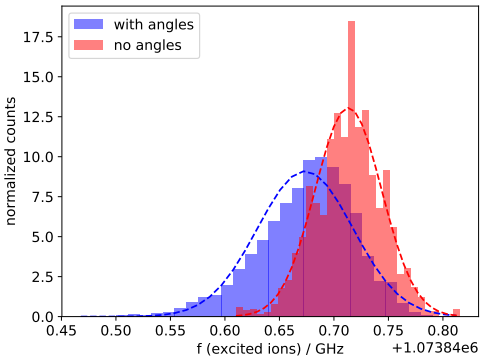

(f) 200 rev, Doppler shifted frequency f

Figure 5.9: Comparison of the starting distribution of the ions in the middle plane of the MR-ToF device ($\sigma_y = 0.7$ mm, $\sigma_{\mathrm{az}} = 0.25$ degree and $\sigma_E = 1$ eV, left column) with the results of all 200 revolutions in the MR-ToF device (right column). See text for details.

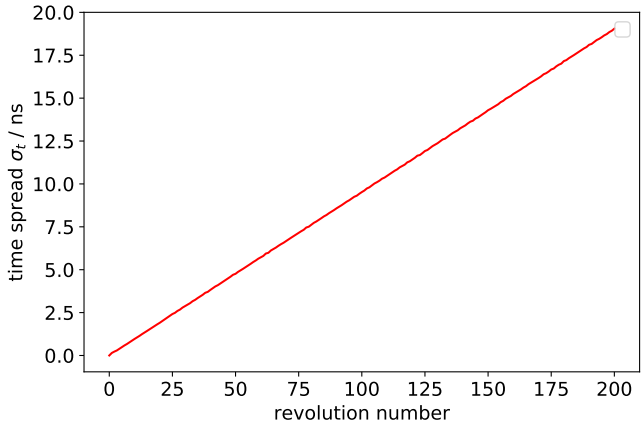

Figure 5.10: Time spread σ_t of the ion bunch's ToF distribution over revolution number.

Table 5.4: Comparison between the results obtained without a single revolution in the MR-ToF device (left column) and the results obtained for 200 revolutions (right column) for potential combination 1. A laser-beam size of 4-mm diameter is assumed and a starting distribution with $\sigma_y = 0.7$ mm, $\sigma_{\mathrm{az}} = 0.25$ degree and $\sigma_E = 1$ eV is chosen. Doppler width, time and energy spread are given in one standard deviation.

	starting values	200 revolutions
transversal rms emittance	3 π mm mrad	3 π mm mrad
trapping efficiency	/	100%
average angle α between ion path and laser axis	0.31 degree	0.33 degree
spread of α	0.17 degree	0.16 degree
ion-laser overlap	98%	98%
energy spread	1 eV	1 eV
time spread	0 ns	20 ns
spectral linewidth (all ions):		
Doppler limit	30.8 MHz	30.8 MHz
Doppler width	47.0 MHz	44.0 MHz
Spectral linewidth (excited ions):		
Doppler limit	30.8 MHz	30.6 MHz
Doppler width	47.0 MHz	43.9 MHz
Difference in average frequencies f		
$f(\alpha = 0) - f$ (all ions):	37.4 MHz	39.5 MHz
$f(\alpha = 0) - f$ (excited ions):	37.3 MHz	39.6 MHz

5.3.5 CLS Parameters Versus Revolution Number

The evolution of the ion-laser overlap, the Doppler width and the centroid over revolution number can be seen in figure 5.11 for potential combination 1 and the starting distribution for a transversal rms emittance of 3π mm mrad with $\sigma_y = 0.7$ mm, $\sigma_{\mathrm{az}} = 0.25$ degree and $\sigma_E = 1$ eV, $E = 30$ keV and 500 ions. Globally, the ion-laser overlap stays constant over revolution number but is fluctuating between 97% and 99% for a diameter of the laser beam of 4 mm and between 64% and 69% for a laser diameter of 2 mm. The Doppler width is staying constant over revolution number and fluctuating between 40 MHz and 47 MHz. The centroid is fluctuating ±3.5 MHz around the mean value. A constant centroid over revolution number is important for e.g. the measurement of the isotope shift (see chapter 4.3.2).

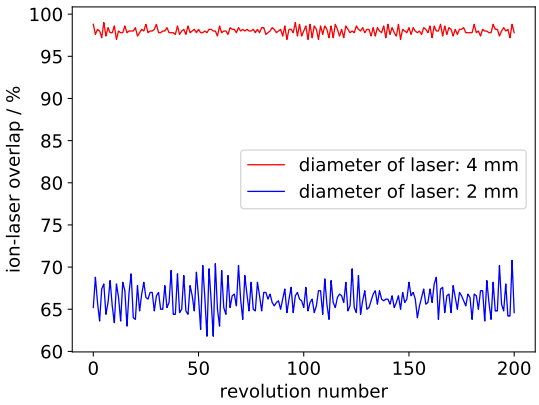

(a) ion-laser overlap

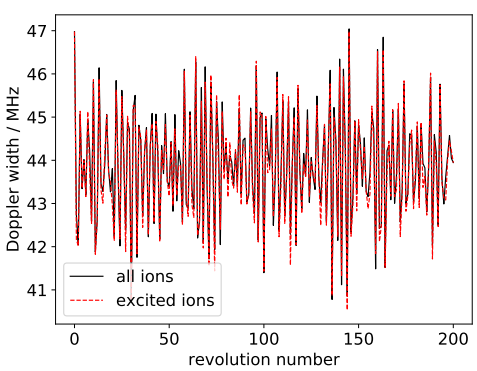

(b) Doppler width

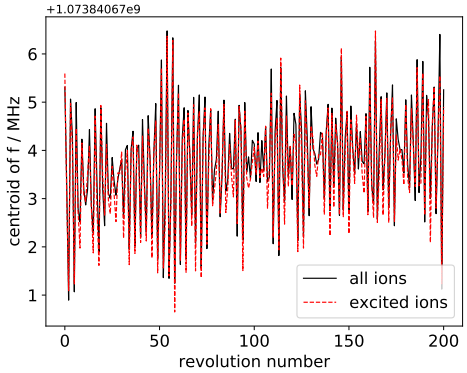

(c) centroid of Doppler shifted frequency

Figure 5.11: Ion-laser overlap (a), Doppler width (b) and centroid of Doppler shifted frequency (c) versus revolution number. For (b) and (c) a diameter of the laser beam of 4 mm is assumed.

5.3.6 CLS Parameters Along MR-ToF Axis

While all the CLS simulation results for the 30-keV MR-ToF discussed so far assumed ions to be in the middle transversal plane of the MR-ToF device, the ODR has an actual length of around ~ 60 cm, given by the three rows of PMTs, where each row needs a space of $\sim$ 20 cm. However, only in a completely field-free region the ion velocity is independent of its position in the ODR. In practice, remaining potential gradients result in slightly different velocities and hence different laser frequencies in the rest frame of the ions as already discussed in chapter 4.4. As shown in figure 5.12, the change in electric potential along the MR-ToF axis is less than 0.1 V in a region of 620 mm corresponding to a change of the Doppler shifted frequency of less than 4 MHz for an ion kinetic energy of 30 keV. Given the lifetime of around 3.8 ns [4] of the excited $3p\ ^2P_{1/2}$ and $3p\ ^2P_{3/2}$ states for the stable Mg^+ ions and the kinetic energy in the MR-ToF device of 30 keV an excited ion will typically move less than 2 mm until it decays back to the ground state. Hence, ions potentially excited outside the ODR at different velocities (and therefore other resonance frequencies in the lab frame) will not be detected.
Due to the field-free region within the ODR the ions are not experiencing any force and therefore their angles keep the same during one passage through the ODR. Hence, the spatial width of the ion bunch increases the further the ion bunch is away from the middle of the MR-ToF axis. To investigate the ion-laser overlap along the MR-ToF axis, the ion distribution is recorded at different transversal planes, that are 75, 150, 225 and 300 mm (corresponds to the end of the ODR) away from the middle plane of the MR-ToF device for a starting distribution with a transversal rms emittance of 3π mm mrad with $\sigma_y = 0.7$ mm and $\sigma_{az} = 0.25$ degree for potential combination 1. If a laser-beam diameter of 2 mm is chosen, the ion-laser overlap would decrease from 66.2% to 19.2% from the middle of the MR-ToF device to the end of the ODR (see table 5.5). If the laser-beam diameter is 4 mm the ion-laser overlap would decrease from 98% to 56.9%. When the ion bunch is further away from the middle plane of the MR-ToF axis, ions with higher angles are normally not laser-excited anymore. Hence, the Doppler width decreases from 43.8 MHz to 35.9 MHz from the middle of the MR-ToF device to the end of the ODR for the assumed laser diameter of 4 mm (see table 5.5).

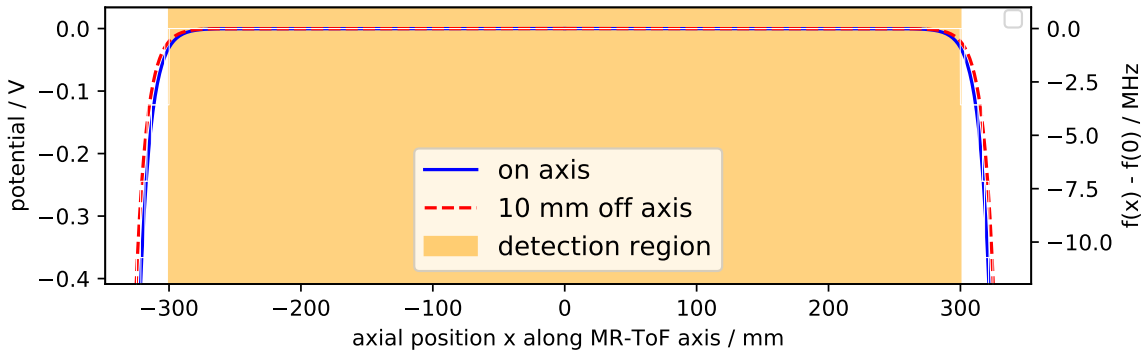

Figure 5.12: Electric potential and the change of the Doppler-shifted frequency $f(x) - f(0)$ for a kinetic energy of 30 keV, once for a $^{24}Mg^+$ ion flying along the central axis and once on a parallel line shifted 10 mm off axis. The length of the ODR is marked in orange. The central drift tube itself is reaching from -345 to 345 mm.

Table 5.5: Evaluation of ion-laser overlap and Doppler width along the MR-ToF axis

distance from middle of MR-ToF device mm	ion-laser overlap (2-mm diameter) %	ion-laser overlap (4-mm diameter) %	Doppler width (laser-exc. ions for 4-mm diameter) MHz
0	66.2	98.0	43.8
75	58.8	96.0	43.4
150	43.7	87.6	41.8
225	29.0	72.9	38.9
300	19.2	56.9	35.9

5.3.7 Stability Considerations

So far, all the simulations described here are carried out for ions with mass 24 u. However, it is also possible to trap ions with a mass from 14 to 200 u with potential combination 1. Ion-laser overlap, mass resolving power and trapping efficiency are farely the same, only the Doppler width is enlarged for smaller masses and reduced for higher masses, as expected when considering equation 4.4, e.g. the simulated Doppler width for the best transformation of phase space for an ion with mass 100 u is $\sim$ 25 MHz, lying above the Doppler limit of $\sim$ 15 MHz.
If the mean ions' kinetic energy is 29.97 keV or 30.07 keV there are no notable differences in the ion-laser overlap, the Doppler width or the mass resolving power compared to an energy of 30 keV.

If the energy spread is 10 eV the Doppler width is with $\sim$ 300 MHz much larger than for an energy spread of 1 eV. However, also the Doppler limit is $\sim$ 290 MHz for 10 eV energy spread and hence the resolution of CLS in a MR-ToF device is not worse than for traditional CLS. For the 10-eV energy spread the ion-laser overlap remains the same, but the mass resolving power is by a factor of around 3 reduced compared to an energy spread of 1 eV.
Due to the fact that the potentials applied to the mirror electrodes might be different in the actual experiment compared to the set values, it is tested what the differences in ion-laser overlap, Doppler width and mass resolving power are if all the mirror potential can differ $\pm$10 V from the set value for 7200 different potential combinations. The deviations in mass resolving power are less than 7%, and the deviations for ion-laser overlap and Doppler width less than 3% for potential combination 1. The trapping efficiency is always 100%. Testing the influence of mirror potentials varying over time or the influence of slightly asymmetric MR-ToF mirrors could be subject of future work.
Overall, the performance of the 30-keV MR-ToF device is fairly stable against inaccuracies in voltage sources, beam energies or energy spread.

Chapter 6

Conclusion

The Multi Ion Reflection Apparatus for Collinear Laser Spectroscopy (MIRACLS) represents a novel approach for highly sensitive and high-resolution laser spectroscopy of short-lived radionuclides. This is envisioned by combining the well-established method of collinear laser spectroscopy (CLS) with advanced ion-trap techniques such as Multi-Reflection Time-of-Flight (MR-ToF) devices. Here, ions are bouncing back and forth between two electrostatic mirrors. Consequently, a laser beam of appropriate wavelength can interact with the ions in an optical detection region during each revolution in the MR-ToF device. Therefore, the experimental sensitivity is enhanced significantly compared to conventional CLS with a single ion passage through the optical detection region.
In the present work, the MIRACLS' proof-of-principle experiment is successfully implemented which demonstrates the functionality of CLS in an existing, low-energy MR-ToF device. By combining a cw laser system with a MR-ToF device, which has been modified for the purpose of CLS, the first fluorescence photons emitted by stable laser-excited Mg^+ ions stored in the MR-ToF device are detected. The passage of the ions through the optical detection region for every revolution in the MR-ToF device is readily apparent in the spectra of the detected photon counts versus the time-of-flight of the ions. By counting the number of photons as a function of the scanned laser frequency the hyperfince structure of the selected optical transition is obtained. This allows the first isotope shift measurements (here $^{26}Mg^+$ vs $^{24}Mg^+$) based on the MIRACLS' approach and motivates further studies on systematic effects and uncertainties, both experimentally and via ion-optical simulations.
Simulations of the ion trajectories in the MIRACLS' proof-of-principle MR-ToF device are performed to investigate the CLS line shape broadening and the ion-laser overlap under varying MR-ToF operation modes. For sets of MR-ToF mirror potentials optimized for the requirements of CLS, the simulated spectral line shape is neither broadened nor significantly distorted by the combination of CLS and MR-ToF operation. The first experimental results of the proof-of-principle experiment are in line with the simulations and benchmark the validity of the simulation approach which then is applied to MIRACLS' future MR-ToF device. This apparatus will operate at ion beam energies of 30 keV to minimize the Doppler broadening such that the spectral linewidth is comparable to the natural linewidth. The 30-keV MR-ToF device will be worldwide the first one to confine an ion bunch with such high kinetic energies. Hence, it will also offer new opportunities for mass separation of rare isotopes. A first design of the novel MR-ToF device is made, where ions with a kinetic energy of 30 keV can be stored. It is shown via simulations that the stringent requirements of CLS can indeed be met.
The first experimental results of MIRACLS' proof-of-principle experiment as well as the simulation of CLS in the envisioned 30-keV MR-ToF apparatus demonstrate the feasibility of high-resolution CLS in a MR-ToF device and highlight the potential of the novel concept of MIRACLS. By trapping the ions between two electrostatic mirrors of the MR-ToF device, the sensitivity of traditional CLS will be enhanced by more than 1-2 orders of magnitude depending on mass and half-life of the studied nuclide. Hence, nuclides currently out of reach, will become experimentally accessible. The nuclear ground-state properties extracted from the measured hyperfine structure of the nuclides serve as an important benchmark of modern nuclear theory and help to understand the evolution of the nuclear shell structure

far away from stability. MIRACLS will open the path to study several key nuclides for nuclear research, that are out of reach for conventional CLS experiments.

Appendix A

Supporting Information for the Chapter: MIRACLS' Proof-of-Principle Experiment

A.1 Modifications on the Beam Line

A.1.1 First Version of the Proof-of-Principle Experiment

The first version of the PoP experiment took an existing MR-ToF apparatus from the university of Greifswald, which was used for mass measurements of clusters as well as for the investigation of space-charge effects [72, 71]. For performing CLS in a MR-ToF device a laser beam had to be sent through the MR-ToF device for the resonant optical excitation of the ions and an optical detection region (ODR) detecting the emitted fluorescence photons over time had to be integrated. The ODR consisting of a lens system and a photomultiplier tube was installed above the central drift tube between the two electrostatic mirrors [76]. Two quadrupole benders were added to facilitate the ion-laser overlap (a schematic is shown in figure A.1 and a photo in figure A.2). The ion beam formed in an offline ion source was bent by 90 degrees by a quadrupole bender (QPB 1) before the ions entered the buffer-gas filled Paul trap, where a bunched beam with low energy spread was obtained. After their release from the Paul trap the ions were accelerated and transported to the MR-ToF device, where they were trapped for several revolutions before the ion beam was bent by 90 degrees by the QPB 2 and the ions were detected on a multichannel plate (MCP).

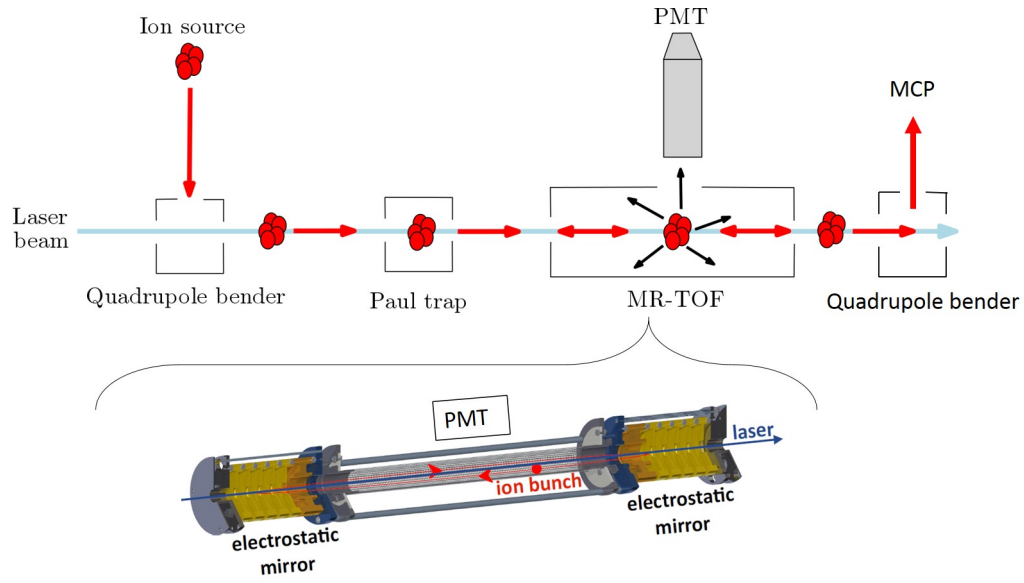

Figure A.1: Schematics of the existing MR-ToF setup from the university of Greifswald with the added optical detection region ODR and the two quadrupole benders QPB 1 and QPB 2. The path of the laser beam is shown in blue, the ion trajectories in red.

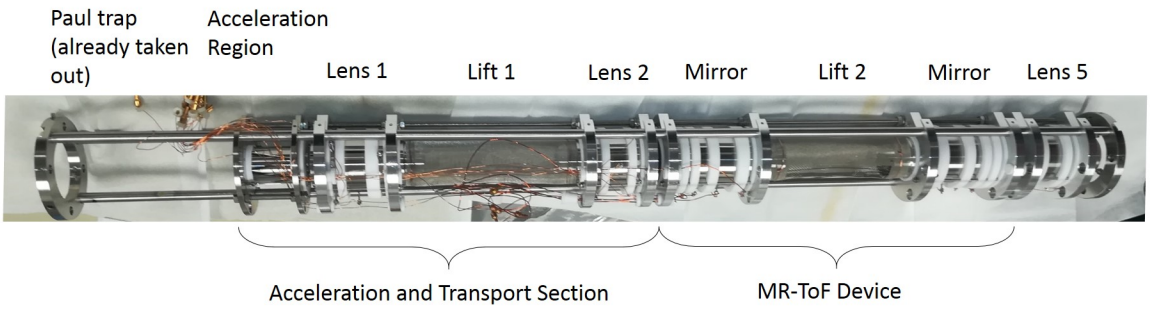

Figure A.2: Photo of the MR-ToF apparatus from the university of Greifswald.

A.1.2 Reduction of Laser-Stray Light by Improvement of the Alignment of the Setup

In the original PoP setup the laser beam had to pass through three small holes with a diameter of 2.5 mm located at the injection electrode of the Paul trap as well as at the entrance and exit endcaps of the Paul trap. These three holes were not lying on a straight line and a misalignment of approximately 0.5 mm in vertical and horizontal direction was discovered. Furthermore, the centre of the exit of the Paul trap was 4-5 mm above the MR-ToF axis defined by the entrance and exit electrode of the MR-ToF device [48]. Due to the fact that simulations (see chapter 4.4 and [48]) show that the laser beam diameter should be 2 mm for an overlap with more than 50% of the ions, this misalignment was interpreted as one explanation for the large amount of observed laser-stray light and likely would also had a very negative effect on the ion-laser overlap. The possible reason for this large misalignment was the shipment of the apparatus from Greifswald/Germany to CERN. Moreover the previous mounting construction used long rods (see figure A.2) which might have gotten sagged over time.

To resolve the misalignment, modifications of the beam line are necessary. The Paul trap, acceleration and transport section are taken out of the setup and put into a 90 degree rotated beamline as can be seen in figure 4.1 and in more detail in figure A.7. Two new electrostatic einzel lenses (lens 3 and lens 4) between QPB 1 and the MR-ToF device are necessary for an optimal focus of the ions into the MR-ToF device. A picture of lens 3 can be seen in figure A.4 and a picture of lens 4 in figure 4.5. In the modified setup the laser beam passes the quadrupole bender and the two lenses and goes straight into the MR-ToF device, where it excites the ions. Hence, the smallest hole that the laser beam with a diameter of $\sim$ 2 mm has to pass through has a diameter of 12 mm and the amount of remaining stray-light is largely reduced.

Furthermore, a new mounting system for the MR-ToF device and lenses 4 and 5 is installed (see figure 4.5). The rods of the new mounting system are less than half the length of the previous ones and therefore the risk that the rods bend is reduced. Hence, it is better assured that lens 4, all the mirror electrodes, the lift tube and lens 5 lie on the same axis. Between lens 4 and the first mirror electrode the mounting system is fixed to the flange of the outer vacuum cross hosting QPB 1 and on the side of lens 5 it is possible to change the position of the MR-ToF axis in respect to the vacuum beam line by three screws (see figure A.3). Changing the MR-ToF axis makes it easier to align the aperture tubes for the reduction of the laser-stray light (see chapter 4.2.7.3 and [48]) and to align the slits of the quadrupole bender to the MR-ToF axis. Lens 3 is mounted directly on one flange of the vacuum tube because the alignment of lens 3 is less crucial than the alignment of the MR-ToF device and the aperture tubes.

Additionally to the installation of a new mounting system for the MR-ToF device a new mounting system for the injection optics, the Paul trap, the acceleration and transport zone (including lens 1 and 2 and lift 1) is installed. On the side of the injection optics the mounting system is fixed to the flange of the vacuum cross, on the side of lens 2 the position of the mounting system can be changed in respect to the beam line via three screws such that the slits of the quadrupole bender are perfectly aligned to the Paul trap, the acceleration and transport section.

The alignment of the modified setup is checked with the help of a theodolite. The slits of QPB 2, the holes of the MR-ToF mirrors, the lift tube, lens 3, lens 4 and the two aperture tubes for the reduction of laser-stray light are all lying on a straight line, called MR-ToF axis. However, the QPB 1 is shifted

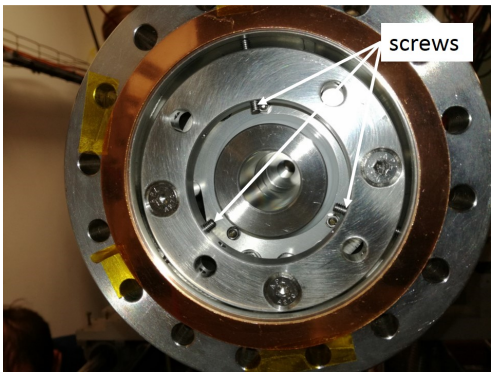

Figure A.3: Looking through lens 5 and the MR-ToF device against the flight direction of the ions. With the help of three screws after lens 5 it is possible to change the position of the MR-ToF axis in respect to the vacuum chamber.

4 mm in horizontal direction in respect to the MR-ToF axis. Unfortunately, there is no straight-forward way to change this. However, the effect of this misalignment on the observed laser-stray light is expected to be minimal, because there is still 4 mm distance between the edge of the plate of the QPB and the axis of the MR-ToF. (The maximal radius of the laser will be 2 mm, and the smallest aperture used for reduction of the laser-stray light has a radius of 3 mm.) Indeed there is no difference in the stray-light rate once measured with the QPB 1 and once measured without the QPB 1 installed in the setup. With the help of steerers and different potentials on the plates of the QPB 1 the ions can be directed onto the MCP. Therefore the misalignment of QPB 1 in respect to the MR-ToF axis has no severe practical consequences.

A.1.3 Increasing the Magnesium-Ion Yield by Improvement of the Ion Injection into the Paul Trap

Simulations of the existing MR-ToF setup from the university of Greifswald show that only 14% of the ions created in the ion source by electron-impact ionisation (further details in chapter 4.2) pass through the 8-mm hole of a collimator that is installed 43 cm after the ion source [48]. By adding a new, additional einzel lens (lens IS in figure A.7) placed between the ion source and the collimator the ion beam is focused into the hole of the collimator and 90% of the ions can pass the collimator according to simulations [48, 24]. Moreover, the collimator hole was increased from 8 mm to 10 mm and the distance between the two plates of the collimator is reduced, such that the ion beam can be easier focused through the collimator. After those modifications a significant increase of the ion yield is expected. Additionally, one stainless steel plate of the collimator is electrically isolated from ground potential in order to be able to read off the ion current before the Paul trap. A picture of the additional lens and the modified collimator can be seen in figure A.4.
By increasing the diameter of the entrance hole of the Paul trap from 2.5 to 4 mm the simulated injection efficiency into the Paul trap can be additionally increased by a factor of 2, and 74% of the ions get from the collimator into the middle of the Paul trap for the larger entrance hole [24]. A larger entrance hole could lead to a worse containment of the buffer gas atoms in the Paul trap. However, we did not observe any cooling problems in the Paul trap after enlarging of the entrance hole.

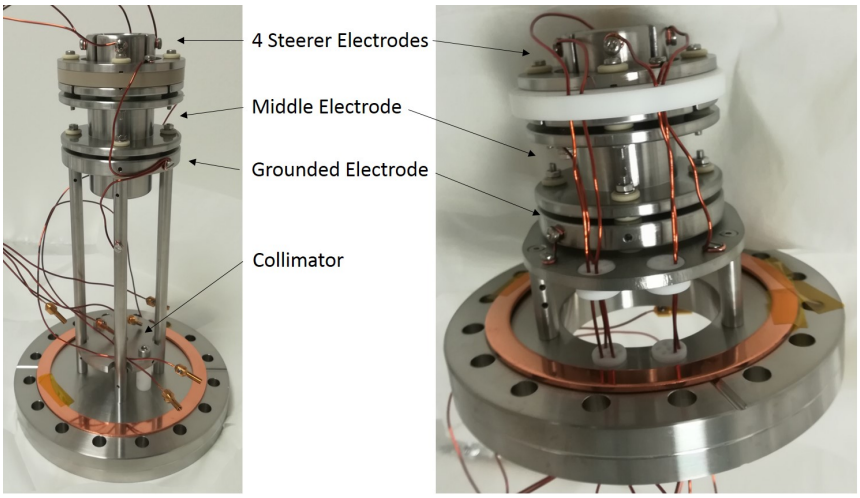

Figure A.4: Left: Additional lens IS and collimator installed between ion source and injection optics. Right: Lens 3 installed directly after the QPB 1.

A.1.4 Modifications of the Vacuum System

In the existing MR-ToF setup from the university of Greifswald it was observed that if the Helium pressure in the Paul trap is increased also the vacuum pressure in the entire setup becomes higher, since the helium can exit the Paul trap through the endcap holes. The vacuum in the MR-ToF region should be in the order of 10^{-8} mbar or better (compare figures 4.33 and 4.34) otherwise the ions might change their flight trajectories through collisions with the residual gas and consequently hit one of the electrodes and get lost. The ions might even get excited in a Mg^{+}-He collision and emit a fluorescence photon when decaying back to their ground state (collisional excitation). To ensure a good vacuum in the MR-ToF region additional turbo pumps are installed. A schematic of the new vacuum system can be seen in figure A.6. The new vacuum system is also necessary because of all the modifications of the beamline as described above. However, also in the modified setup an increase in the Helium pressure in the Paul trap region leads to a higher pressure in the MR-ToF region, as can be seen in figure A.5. This may be explained by the entrance hole of the Paul trap which is increased from 2.5 to 4 mm and more helium atoms can leave the Paul trap (see chapter A.1.3).

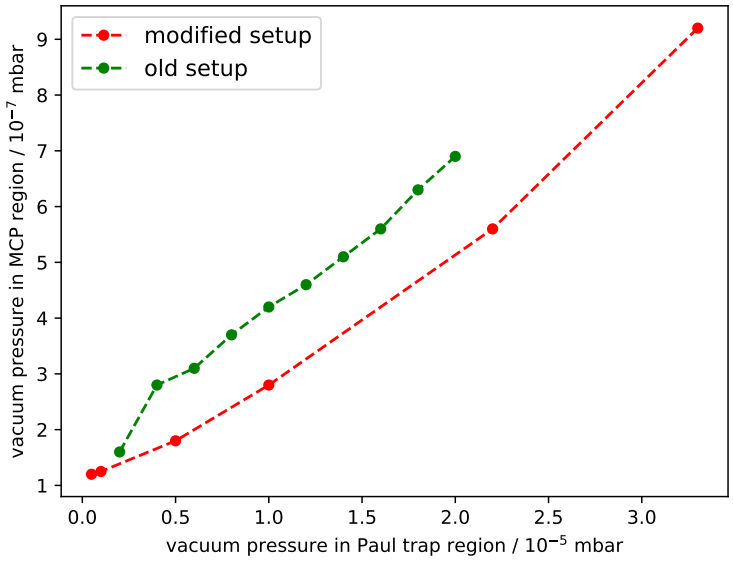

Figure A.5: Vacuum pressure in the MCP region as a function of the vacuum pressure in the Paul trap region (lines to guide the eye) for the modified PoP setup and for the old setup (data taken from [24]). The pressure readings are normalized to N_2 as residual gas and the used vacuum gauges are not calibrated. Therefore any given pressure values are only meant to illustrate the relative changes in the vacuum.

A.2 Schematical Drawings of the Proof-of-Principle Setup

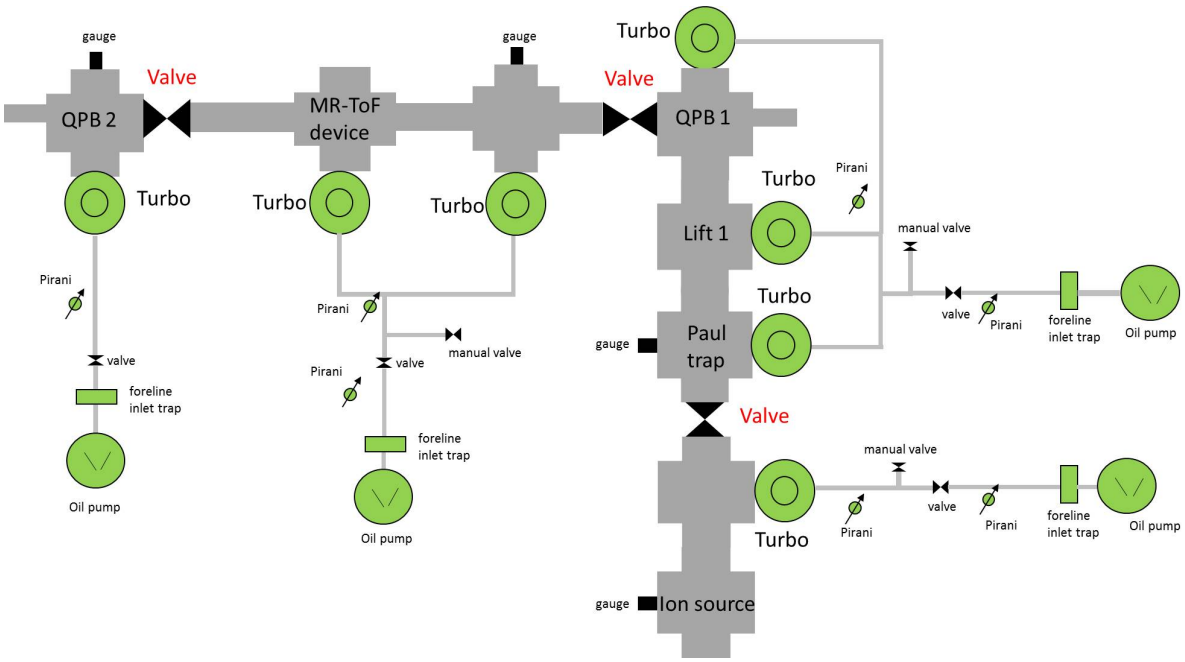

Figure A.6: Schematics of the vacuum system for the Proof-of-Principle Experiment. The vacuum system consists of several CF100 crosses, flanges and tubes hosting the whole setup, 4 oil pumps as prepumps and 6 big and 1 small turbo pump. The prepumps are connected to the turbo pumps through a prevacuum system. With the help of three valves it is possible to separate the high-vacuum volumes. The vacuum pressure can be read off by gauges and is in the order of 10^{-7} to 10^{-8} mbar. Venting of the vacuum chamber is possible by leaking in nitrogen N_2 through the manual valves. The Pirani gauges are used to read off the prevacuum that is in the order of 10^{-2} mbar. The foreline inlet traps are used to prevent the oil from the prepumps flowing into the vacuum chambers.

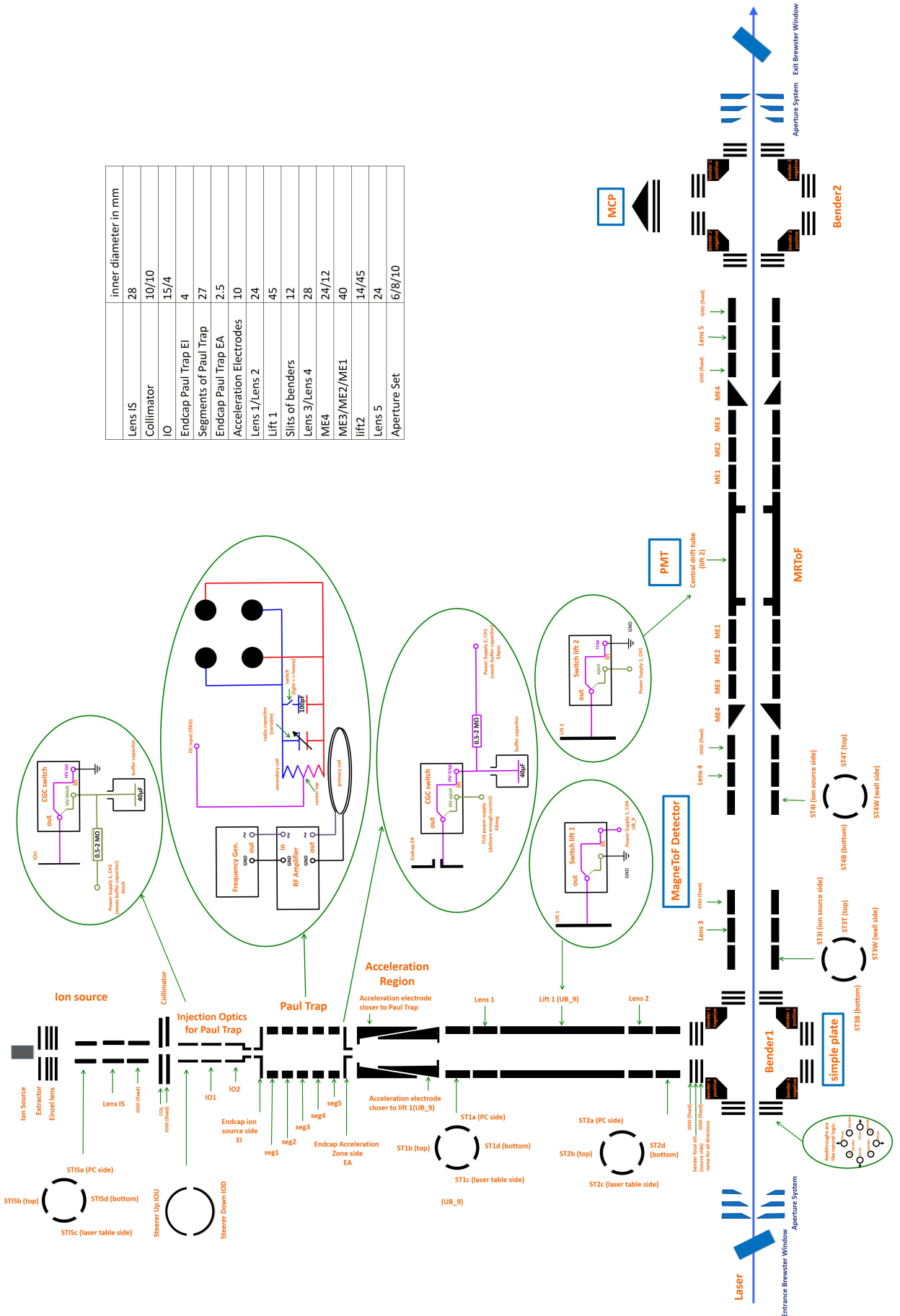

Figure A.7: Detailed schematic of the proof-of-principle setup. See text for details.

A.3 Effects of Black Color on Vacuum Quality

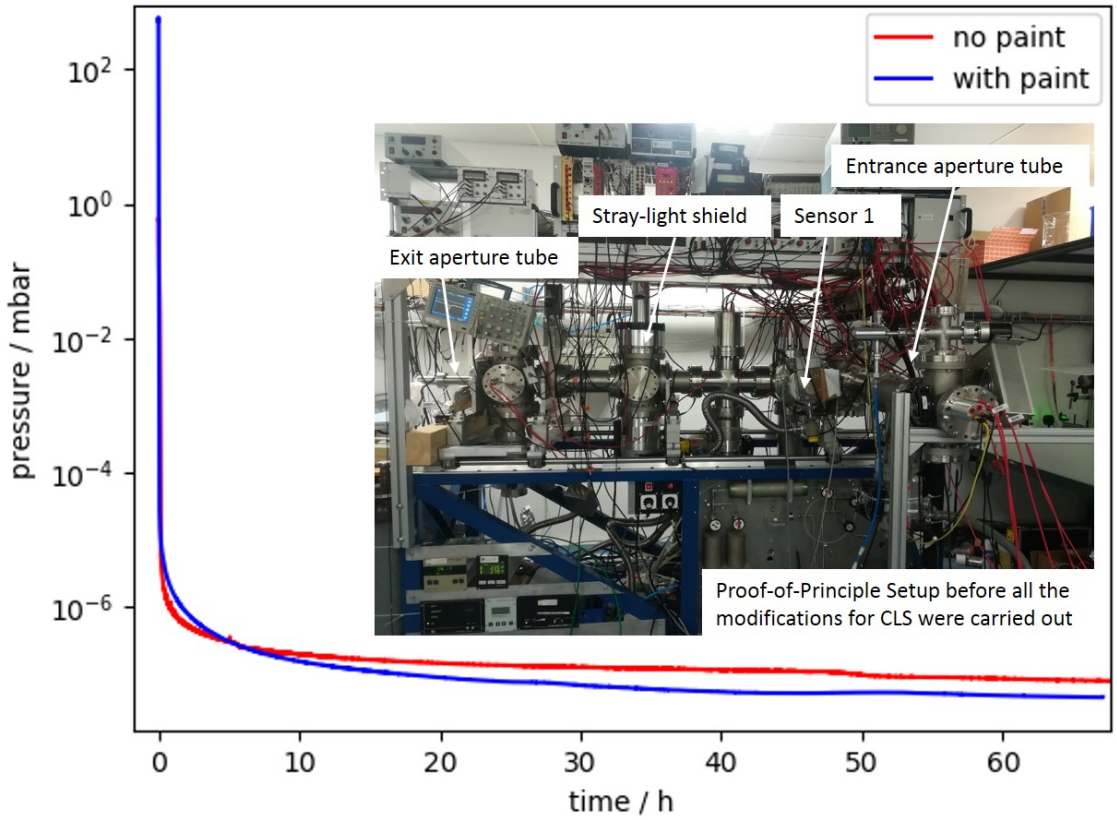

Figure A.8: Effects of black color on vacuum quality: In the insert a picture of the proof-of-principle setup at the time when the vacuum tests were carried out is shown. At this time hardly any CLS modifications on the beamline were carried out. The vacuum pressure was recorded with a Full Range Gauge, positioned at the middle of the beam line (marked with Sensor 1) once before the black-painted entrance and exit apertures and the black-painted stray-light shield were installed (red curve) and once after they were installed (blue curve). The vacuum measurement without the parts painted in black (red curve) was carried out before the vacuum measurement with the parts painted in black (blue curve). Due to the fact that the beamline was vented for a long time it took a longer time for reaching a reasonable vacuum for the first measurement without paint. One can conclude that painting the very localised regions in black with Tetenal Camera Spray did not lead to any reduction of the vacuum quality.

A.4 Potentials of the Electrodes Used in the Simulations

Table A.1: Potentials of the electrodes used for most of the simulations of the PoP setup

name of electrode	potential / V
Part of Injection Optics IO2	-250
endcap EI	-500
Segment 1	310
Segment 2	255.5
Segment 3	234.32
Segment 4	233
Segment 5	224
endcap EA	265 (trapping), 169 (ejection)
Acceleration electrode closer to Paul trap	142
Acceleration electrode closer to lift 1	-2080
Lens 1	-500
Lift 1	-2080
Lens 2	-2150
QPB 1	$\pm$1575
Lens 3	1240
Lens 4	-3700
Mirror ME1	-4814
Mirror ME2	1897
Mirror ME3	584.5
Mirror ME4 (outermost)	1706.3

Bibliography

[1] ISOLDE Logos, Layouts and Templates, 2018. http://isolde.web.cern.ch/isolde-logos-layouts-and-templates#.

[2] J. D. Alexander, C. R. Calvert, R. B. King, O. Kelly, W. A. Bryan, G. R. A. J. Nemeth, W. R. Newell, C. A. Froud, I. C. E. Turcu, E. Springate, P. A. Orr, J. Pedregosa-Gutierrez, C. W. Walter, R. A Williams, I. D. Williams, and J. B. Greenwood. Short pulse laser-induced dissociation of vibrationally cold, trapped molecular ions. *Journal of Physics B: Atomic, Molecular and Optical Physics*, 42(15):154027, 2009.

[3] I. Podadera Aliseda, T. Fritioff, T. Giles, A. Jokinen, M. Lindroos, and F. Wenander. Design of a second generation RFQ Ion Cooler and Buncher (RFQCB) for ISOLDE. *Nuclear Physics A*, 746:647 – 650, 2004. Proceedings of the Sixth International Conference on Radioactive Nuclear Beams (RNB6).

[4] W. Ansbacher, Y. Li, and E.H. Pinnington. Precision lifetime measurement for the 3p levels of Mg II using frequency-doubled laser radiation to excite a fast ion beam. *Physics Letters A*, 139(3):165 – 169, 1989.

[5] Lara Bartels. Increasing electron emission rates in an offline electron impact Mg^+ ion source for laser spectroscopy of radioactive ions. Bachelor's thesis, Georg-August-Universität Göttingen, 2018.

[6] V. Batteiger, S. Knünz, M. Herrmann, G. Saathoff, H. A. Schüssler, B. Bernhardt, T. Wilken, R. Holzwarth, T. W. Hänsch, and Th. Udem. Precision spectroscopy of the $3s-3p$ fine-structure doublet in Mg^+. *Phys. Rev. A*, 80:022503, Aug 2009.

[7] W. Henry Benner. A gated electrostatic ion trap to repetitiously measure the charge and m/z of large electrospray ions. *Anal. Chem.*, 69(20):4162–4168, October 1997.

[8] P.F. Bernath. *Spectra of Atoms and Molecules*. Oxford University Press, 2016.

[9] Mark Bissell. Personal communications (2018).

[10] H.K. Blaum and F. Herfurth. *Trapped Charged Particles and Fundamental Interactions*. Lecture Notes in Physics. Springer Berlin Heidelberg, 2008.

[11] Klaus Blaum, Jens Dilling, and Wilfried Nörtershäuser. Precision atomic physics techniques for nuclear physics with radioactive beams. *Physica Scripta*, 2013(T152):014017, 2013.

[12] Christian Breitenfeldt, Michael Wayne Froese, Klaus Blaum, Sebastian George, Manfred Grieser, Michael Lange, Sebastian Menk, Roland Repnow, Dirk Schwalm, Lutz Schweikhard, Robert von Hahn, and Andreas Wolf. Spreading times of ion-bunches in the cryogenic trap for fast ion beams. *International Journal of Mass Spectrometry*, 396:1 – 4, 2016.

[13] Brookhaven National Laboratory. National Nuclear Data Center, 2018. `http://www.nndc.bnl.gov/chart/`.

[14] P. Campbell, I.D. Moore, and M.R. Pearson. Laser spectroscopy for nuclear structure physics. *Progress in Particle and Nuclear Physics*, 86:127 – 180, 2016.

[15] T.E. Cocolios, H.H. Al Suradi, J. Billowes, I. Budinčević, R.P. de Groote, S. De Schepper, V.N. Fedosseev, K.T. Flanagan, S. Franchoo, R.F. Garcia Ruiz, H. Heylen, F. Le Blanc, K.M. Lynch, B.A. Marsh, P.J.R. Mason, G. Neyens, J. Papuga, T.J. Procter, M.M. Rajabali, R.E. Rossel, S. Rothe, G.S. Simpson, A.J. Smith, I. Strashnov, H.H. Stroke, D. Verney, P.M. Walker, K.D.A. Wendt, and R.T. Wood. The collinear resonance ionization spectroscopy (CRIS) experimental setup at CERN-ISOLDE. *Nuclear Instruments and Methods in Physics Research Section B: Beam Interactions with Materials and Atoms*, 317:565 – 569, 2013. XVIth International Conference on ElectroMagnetic Isotope Separators and Techniques Related to their Applications, December 2–7, 2012 at Matsue, Japan.

[16] Konstantin Zhernosekov Karl Johnston Cristina Mueller, Ulli Koester. A Unique Matched Quadruplet of Terbium Radioisotopes for PET and SPECT and for a- and b2-Radionuclide Therapy: An In Vivo Proof-of-Concept Study with a New Receptor-Targeted Folate Derivative. *Journal of Nuclear Medicine*, 2012.

[17] David A Dahl. SimIon for the personal computer in reflection. *International Journal of Mass Spectrometry*, 200(1):3 – 25, 2000. Volume 200: The state of the field as we move into a new millenium.

[18] T. Dickel, W.R. Plaß, A. Becker, U. Czok, H. Geissel, E. Haettner, C. Jesch, W. Kinsel, M. Petrick, C. Scheidenberger, A. Simon, and M.I. Yavor. A high-performance multiple-reflection time-of-flight mass spectrometer and isobar separator for the research with exotic nuclei. *Nuclear Instruments and Methods in Physics Research Section A: Accelerators, Spectrometers, Detectors and Associated Equipment*, 777:172 – 188, 2015.

[19] Timo Dickel, Mikhail I. Yavor, Johannes Lang, Wolfgang R. Plaß, Wayne Lippert, Hans Geissel, and Christoph Scheidenberger. Dynamical time focus shift in multiple-reflection time-of-flight mass spectrometers. *International Journal of Mass Spectrometry*, 412:1 – 7, 2017.

[20] Donald J. Douglas, Aaron J. Frank, and Dunmin Mao. Linear ion traps in mass spectrometry. *Mass Spectrometry Reviews*, 24(1):1–29, 2004.

[21] M. Drewsen and A. Brøner. Harmonic linear paul trap: Stability diagram and effective potentials. *Phys. Rev. A*, 62:045401, Sep 2000.

[22] I. Podadera M. Lindroos R. Catherall T. Giles H. Franberg J. Billowes F. Duval E. Mané, P. Delahaye and A. Jokinen. ISCOOL: cooled and bunched beams for ISOLDE. ISOLDE workshop and users meeting, 2007.

[23] D.A. Edwards and M.J. Syphers. *An Introduction to the Physics of High Energy Accelerators*. Wiley Series in Beam Physics and Accelerator Technology. Wiley, 2008.

[24] Laurin Fischer. Improvements of the beam intensity of stable Mg ions for the proof-of-principle experiment of collinear laser spectroscopy on short-lived nuclides in a multi ion reflection apparatus. Bachelor's thesis, CERN, 2018.

[25] Paul Fischer, Stefan Knauer, Gerrit Marx, and Lutz Schweikhard. In-depth study of in-trap high-resolution mass separation by transversal ion ejection from a multi-reflection time-of-flight device. *Review of Scientific Instruments*, 89(1):015114, 2018.

[26] Paul Fischer, Stefan Knauer, Gerrit Marx, and Lutz Schweikhard. Non-isobaric time-of-flight correction for isobar resolving in MR-ToF mass spectrometry. *International Journal of Mass Spectrometry*, 432:44 – 51, 2018.

[27] Kieran Flanagan. CRIS: a new sensitive device for laser spectroscopy of exotic nuclei. *Nuclear Physics News*, 23(2):24–26, 2013.

[28] Klaus Floettmann. Some basic features of the beam emittance. *Phys. Rev. ST Accel. Beams*, 6:034202, 2003.

[29] C.J. Foot and D.P.C.J. Foot. *Atomic Physics*. Oxford Master Series in Physics. OUP Oxford, 2005.

[30] H. Frånberg, P. Delahaye, J. Billowes, K. Blaum, R. Catherall, F. Duval, O. Gianfrancesco, T. Giles, A. Jokinen, M. Lindroos, D. Lunney, E. Mane, and I. Podadera. Off-line commissioning of the ISOLDE cooler. *Nuclear Instruments and Methods in Physics Research Section B: Beam Interactions with Materials and Atoms*, 266(19):4502 – 4504, 2008. Proceedings of the XVth International Conference on Electromagnetic Isotope Separators and Techniques Related to their Applications.

[31] A. T. Gallant, M. Brodeur, C. Andreoiu, A. Bader, A. Chaudhuri, U. Chowdhury, A. Grossheim, R. Klawitter, A. A. Kwiatkowski, K. G. Leach, A. Lennarz, T. D. Macdonald, B. E. Schultz, J. Lassen, H. Heggen, S. Raeder, A. Teigelhöfer, B. A. Brown, A. Magilligan, J. D. Holt, J. Menéndez, J. Simonis, A. Schwenk, and J. Dilling. Breakdown of the isobaric multiplet mass equation for the $a = 20$ and 21 multiplets. *Phys. Rev. Lett.*, 113:082501, Aug 2014.

[32] R. F. Garcia Ruiz, M. L. Bissell, K. Blaum, A. Ekström, N. Frömmgen, G. Hagen, M. Hammen, K. Hebeler, J. D. Holt, G. R. Jansen, M. Kowalska, K. Kreim, W. Nazarewicz, R. Neugart, G. Neyens, W. Nörtershäuser, T. Papenbrock, J. Papuga, A. Schwenk, J. Simonis, K. A. Wendt, and D. T. Yordanov. Unexpectedly large charge radii of neutron-rich calcium isotopes. *Nature Physics*, 12:594, February 2016.

[33] S. Giere, M. Kurrat, and U. Schumann. HV dielectric strength of shielding electrodes in vacuum circuit-breakers. *20th International Symposium on Discharges and Electrical Insulation in Vacuum*, pages 119–12, 2002.

[34] T.J. Giles, R. Catherall, V. Fedosseev, U. Georg, E. Kugler, J. Lettry, and M. Lindroos. The high resolution spectrometer at isolde. *Nuclear Instruments and Methods in Physics Research Section B: Beam Interactions with Materials and Atoms*, 204:497 – 501, 2003. 14th International Conference on Electromagnetic Isotope Separators and Techniques Related to their Applications.

[35] F Herfurth, J Dilling, A Kellerbauer, G Bollen, S Henry, H.-J Kluge, E Lamour, D Lunney, R.B Moore, C Scheidenberger, S Schwarz, G Sikler, and J Szerypo. A linear radiofrequency ion trap for accumulation, bunching, and emittance improvement of radioactive ion beams. *Nuclear Instruments and Methods in Physics Research Section A: Accelerators, Spectrometers, Detectors and Associated Equipment*, 469(2):254 – 275, 2001.

[36] H. Heylen. Unpublished: DAQ System for the MIRACLS Proof-of-Principle Setup. 2018.

[37] Tsviki Y. Hirsh, Nancy Paul, Mary Burkey, Ani Aprahamian, Fritz Buchinger, Shane Caldwell, Jason A. Clark, Anthony F. Levand, Lin Ling Ying, Scott T. Marley, Graeme E. Morgan, Andrew Nystrom, Rodney Orford, Adrian Pérez Galván, John Rohrer, Guy Savard, Kumar S. Sharma, and Kevin Siegl. First operation and mass separation with the CARIBU MR-TOF. *Nuclear Instruments and Methods in Physics Research Section B: Beam Interactions with Materials and Atoms*, 376:229 – 232, 2016. Proceedings of the XVIIth International Conference on Electromagnetic Isotope Separators and Related Topics (EMIS2015), Grand Rapids, MI, U.S.A., 11-15 May 2015.

[38] ISOLDE Yield Database, 2018. `https://isoyields2.web.cern.ch/`.

[39] A. Jokinen, M. Lindroos, E. Molin, and M. Petersson. RFQ-cooler for low-energy radioactive ions at ISOLDE. *Nuclear Instruments and Methods in Physics Research Section B: Beam Interactions with Materials and Atoms*, 204:86 – 89, 2003. 14th International Conference on Electromagnetic Isotope Separators and Techniques Related to their Applications.

[40] T. Kalvas. *CAS CERN Accelerator School: Ion Sources - Beam Extraction and Transport*. CERN (Series). CERN, 2013.

[41] Rituparna Kanungo. A new view of nuclear shells. *Physica Scripta*, 2013(T152):014002, 2013.

[42] S.L. Kaufman. High-resolution laser spectroscopy in fast beams. *Optics Communications*, 17(3):309 – 312, 1976.

[43] K. Kreim, M.L. Bissell, J. Papuga, K. Blaum, M. De Rydt, R.F. Garcia Ruiz, S. Goriely, H. Heylen, M. Kowalska, R. Neugart, G. Neyens, W. Nörtershäuser, M.M. Rajabali, R. Sánchez Alarcón, H.H. Stroke, and D.T. Yordanov. Nuclear charge radii of potassium isotopes beyond n=28. *Physics Letters B*, 731:97 – 102, 2014.

[44] L. Schweikhard et al. Isobar separation and precision mass spectrometry of short-lived nuclides with a multi-reflection time-of-flight analyzer. *Proceedings of Science*, 2014.

[45] M. Lange, M. Froese, S. Menk, J. Varju, R. Bastert, K. Blaum, J. R. Crespo López-Urrutia, F. Fellenberger, M. Grieser, R. von Hahn, O. Heber, K.-U. Kühnel, F. Laux, D. A. Orlov, M. L.

Rappaport, R. Repnow, C. D. Schröter, D. Schwalm, A. Shornikov, T. Sieber, Y. Toker, J. Ullrich, A. Wolf, and D. Zajfman. A cryogenic electrostatic trap for long-time storage of keV ion beams. *Review of Scientific Instruments*, 81(5):055105, 2010.

[46] R.V. Latham. *High Voltage Vacuum Insulation: Basic Concepts and Technological Practice*. Elsevier Science, 1995.

[47] S. Lechner. Unpublished: SimIon simulations for the new MIRACLS Cooler and Buncher. 2018.

[48] Franziska Maier. Laser spectroscopy of short-lived radionuclides in an ion trap: MIRACLS' proof-of-principle experiment. Technical report, CERN, 2017.

[49] F.G. Major, V.N. Gheorghe, and G. Werth. *Charged Particle Traps: Physics and Techniques of Charged Particle Field Confinement*. Springer Series on Atomic, Optical, and Plasma Physics. Springer Berlin Heidelberg, 2006.

[50] Stephan Malbrunot-Ettenauer. Personal communications (2018).

[51] Stephan Malbrunot-Ettenauer. Unpublished: Stray-Light Shield for the proof-of-principle setup. 2018.

[52] Stephan Malbrunot-Ettenauer and Hanne Heylen. Personal communications 2018.

[53] E. Mané, J. Billowes, K. Blaum, P. Campbell, B. Cheal, P. Delahaye, K. T. Flanagan, D. H. Forest, H. Franberg, C. Geppert, T. Giles, A. Jokinen, M. Kowalska, R. Neugart, G. Neyens, W. Nörtershäuser, I. Podadera, G. Tungate, P. Vingerhoets, and D. T. Yordanov. An ion cooler-buncher for high-sensitivity collinear laser spectroscopy at ISOLDE. *The European Physical Journal A*, 42(3):503–507, Dec 2009.

[54] B. A. Marsh. Resonance ionization laser ion sources for on-line isotope separators (invited). *Review of Scientific Instruments*, 85(2):02B923, 2014.

[55] R. B. Moore, A. M. Ghalambor Dezfuli, P. Varfalvy, H. Zhao, and The ISOLDE Collaboration. Production, transfer and injection of charged particles in traps and storage rings. *Physica Scripta*, 1995(T59):93, 1995.

[56] Frédéric Moynier and Toshiyuki Fujii. Theoretical isotopic fractionation of magnesium between chlorophylls. *Scientific Reports*, 7(1):6973, August 2017.

[57] M. Mukherjee, D.Beck, K. Blaum, G. Bollen, J. Dilling, S. George, F. Herfurth, A. Herlert andA. Kellerbauer, H.-J. Kluge, S. Schwarz, L. Schweikhard, and C. Yazidjian. ISOLTRAP: An on-line penning trap for mass spectrometry on short-lived nuclides. *Eur. Phys. J. A*, 2008.

[58] Cristina Müller, Christiaan Vermeulen, Karl Johnston, Ulli Köster, Raffaella Schmid, Andreas Türler, and Nicholas P. van der Meulen. Preclinical in vivo application of 152Tb-DOTANOC: a radiolanthanide for PET imaging. *EJNMMI Research*, 6(1):35, Apr 2016.

[59] T. Murböck, S. Schmidt, Z. Andelkovic, G. Birkl, W. Nörtershäuser, and M. Vogel. A compact source for bunches of singly charged atomic ions. *Review of Scientific Instruments*, 87(4):043302, 2016.

[60] R. Neugart, J. Billowes, M. L. Bissell, K. Blaum, B. Cheal, K. T. Flanagan, G. Neyens, W. Nörtershäuser, and D. T. Yordanov. Collinear laser spectroscopy at ISOLDE: new methods and highlights. *Journal of Physics G: Nuclear and Particle Physics*, 44(6):064002, 2017.

[61] Gerda Neyens. Nuclear magnetic and quadrupole moments for nuclear structure research on exotic nuclei. *Reports on Progress in Physics*, 66(4):633, 2003.

[62] NIST-National Institute of Standards and Technology. Atomic data for magnesium, 2018. `https://www.nist.gov/`.

[63] W. Nörtershäuser, D. Tiedemann, M. Žáková, Z. Andjelkovic, K. Blaum, M. L. Bissell, R. Cazan, G. W. F. Drake, Ch. Geppert, M. Kowalska, J. Krämer, A. Krieger, R. Neugart, R. Sánchez, F. Schmidt-Kaler, Z.-C. Yan, D. T. Yordanov, and C. Zimmermann. Nuclear charge radii of ^{7,9,10}Be and the one-neutron halo nucleus ^{11}Be. *Phys. Rev. Lett.*, 102:062503, Feb 2009.

[64] Wolfgang Paul. Electromagnetic traps for charged and neutral particles. *Rev. Mod. Phys.*, 62:531–540, Jul 1990.

[65] A. Piechaczek, V. Shchepunov, H.K. Carter, J.C. Batchelder, E.F. Zganjar, S.N. Liddick, H. Wollnik, Y. Hu, and B.O. Griffith. Development of a high resolution isobar separator for study of exotic decays. *Nuclear Instruments and Methods in Physics Research Section B: Beam Interactions with Materials and Atoms*, 266(19):4510 – 4514, 2008. Proceedings of the XVth International Conference on Electromagnetic Isotope Separators and Techniques Related to their Applications.

[66] Wolfgang R. Plaß, Timo Dickel, Ulrich Czok, Hans Geissel, Martin Petrick, Katrin Reinheimer, Christoph Scheidenberger, and Mikhail I.Yavor. Isobar separation by time-of-flight mass spectrometry for low-energy radioactive ion beam facilities. *Nuclear Instruments and Methods in Physics Research Section B: Beam Interactions with Materials and Atoms*, 266(19):4560 – 4564, 2008. Proceedings of the XVth International Conference on Electromagnetic Isotope Separators and Techniques Related to their Applications.

[67] I. Podadera, T. Fritioff, A. Jokinen, J. F. Kepinski, M. Lindroos, D. Lunney, and F. Wenander. Preparation of cooled and bunched ion beams at ISOLDE-CERN. *The European Physical Journal A - Hadrons and Nuclei*, 25(1):743–744, Sep 2005.

[68] M. Reiser. *Theory and Design of Charged Particle Beams*. Wiley Series in Beam Physics and Accelerator Technology. Wiley, 2008.

[69] Rheinmetall Air Defence AG (OPSQ-80C12-10-5, syntetic fused silica). Communications via mail, 2018.

[70] C. Heise J.R. Esmond R.L.Kurucz, P. Smith. Atomic spectral line database, 2018. `https://www.cfa.harvard.edu/amp/ampdata/kurucz23/sekur.html`.

[71] M. Rosenbusch, P. Chauveau, P. Delahaye, G. Marx, L. Schweikhard, F. Wienholtz, and R. N. Wolf. Delayed bunching for multi-reflection time-of-flight mass separation. *AIP Conference Proceedings*, 1668(1):050001, 2015.

[72] M. Rosenbusch, S. Kemnitz, R. Schneider, L. Schweikhard, R. Tschiersch, and R. N. Wolf. Towards systematic investigations of space-charge phenomena in multi-reflection ion traps. *AIP Conference Proceedings*, 1521(1):53–62, 2013.

[73] R.E. Rossel, V.N. Fedosseev, B.A. Marsh, D. Richter, S. Rothe, and K.D.A. Wendt. Data acquisition, remote control and equipment monitoring for ISOLDE RILIS. *Nuclear Instruments and Methods in Physics Research Section B: Beam Interactions with Materials and Atoms*, 317:557 – 560, 2013. XVIth International Conference on ElectroMagnetic Isotope Separators and Techniques Related to their Applications, December 2–7, 2012 at Matsue, Japan.

[74] D.J. Rowe and J.L. Wood. *Fundamentals of Nuclear Models: Foundational Models*. World Scientific, 2010.

[75] Lawrence Ruby. Applications of the mathieu equation. *American Journal of Physics*, 64(1):39–44, 1996.

[76] Stefan Sailer. Improvements of the optical detection setup for collinear laser spectroscopy of short-lived radioactive nuclides and spectroscopic studies on the hyperfine parameters of Bi. Master's thesis, CERN, 2016.

[77] P. Schury, K. Okada, S. Shchepunov, T. Sonoda, A. Takamine, M. Wada, H. Wollnick, and Y. Yamazaki. Multi-reflection time-of-flight mass spectrograph for short-lived radioactive ions. *Eur. Phys. J. A*, 2009.

[78] Jae C Schwartz, Michael W Senko, and John E.P Syka. A two-dimensional quadrupole ion trap mass spectrometer. *Journal of the American Society for Mass Spectrometry*, 13(6):659 – 669, 2002.

[79] S. Schwarz, G. Bollen, R. Ringle, J. Savory, and P. Schury. The LEBIT ion cooler and buncher. *Nuclear Instruments and Methods in Physics Research Section A: Accelerators, Spectrometers, Detectors and Associated Equipment*, 816:131 – 141, 2016.

[80] Stefan Schwarz. Ioncool—a versatile code to characterize gas-filled ion bunchers and coolers (not only) for nuclear physics applications. *Nuclear Instruments and Methods in Physics Research Section A: Accelerators, Spectrometers, Detectors and Associated Equipment*, 566(2):233 – 243, 2006.

[81] SimIon. SimIon 8.1.1.32 - The field and particle trajectory simulator, 2018. `https://simion.com/`.

[82] Sirah - Lasertechnik GmbH. Matisse 2 DS, 2018. `http://www.sirah.com/laser/cw-ring-lasers/matisse-ds`.

[83] O. Sorlin and M.-G. Porquet. Nuclear magic numbers: New features far from stability. *Progress in Particle and Nuclear Physics*, 61(2):602 – 673, 2008.

[84] T. Stora. Personal communications 2018.

[85] CERN Store. 44.88.60 - plates - polyethylene. CERN Stores Catalogue, 2018.

[86] Thorlabs, Inc. KT310 - Spatial Filter. Technical report, 2018. `https://www.thorlabs.com/newgrouppage9.cfm?objectgroup_id=10768`.

[87] Werner Tretner. An electrostatic mass spectroscope. *Vacuum*, 10(1):31 – 34, 1960.

[88] F. Wienholtz, D. Beck, K. Blaum, Ch. Borgmann, M. Breitenfeldt, R. B. Cakirli, S. George, F. Herfurth, J. D. Holt, M. Kowalska, S. Kreim, D. Lunney, V. Manea, J. MenÃ©ndez, D. Neidherr, M. Rosenbusch, L. Schweikhard, A. Schwenk, J. Simonis, J. Stanja, R. N. Wolf, and K. Zuber. Masses of exotic calcium isotopes pin down nuclear forces. *Nature*, 498:346–, June 2013.

[89] Frank Wienholtz. Personal communications 2018.

[90] R.N. Wolf, D. Beck, K. Blaum, Ch. Böhm, Ch. Borgmann, M. Breitenfeldt, F. Herfurth, A. Herlert, M. Kowalska, S. Kreim, D. Lunney, S. Naimi, D. Neidherr, M. Rosenbusch, L. Schweikhard, J. Stanja, F. Wienholtz, and K. Zuber. On-line separation of short-lived nuclei by a multi-reflection time-of-flight device. *Nuclear Instruments and Methods in Physics Research Section A: Accelerators, Spectrometers, Detectors and Associated Equipment*, 686:82 – 90, 2012.

[91] R.N. Wolf, F. Wienholtz, D. Atanasov, D. Beck, K. Blaum, Ch. Borgmann, F. Herfurth, M. Kowalska, S. Kreim, Yu. A. Litvinov, D. Lunney, V. Manea, D. Neidherr, M. Rosenbusch, L. Schweikhard, J. Stanja, and K. Zuber. ISOLTRAP's multi-reflection time-of-flight mass separator/spectrometer. *International Journal of Mass Spectrometry*, 349-350:123 – 133, 2013. 100 years of Mass Spectrometry.

[92] Robert N. Wolf, Gerrit Marx, Marco Rosenbusch, and Lutz Schweikhard. Static-mirror ion capture and time focusing for electrostatic ion-beam traps and multi-reflection time-of-flight mass analyzers by use of an in-trap potential lift. *International Journal of Mass Spectrometry*, 313:8 – 14, 2012.

[93] H. Wollnik and M. Przewloka. Time-of-flight mass spectrometers with multiply reflected ion trajectories. *International Journal of Mass Spectrometry and Ion Processes*, 96(3):267 – 274, 1990.

[94] Oh Kyu Yoon, Ignacio A. Zuleta, Matthew D. Robbins, Griffin K. Barbula, and Richard N. Zare. Simple template-based method to produce bradbury-nielsen gates. *Journal of the American Society for Mass Spectrometry*, 18(11):1901 – 1908, 2007.

[95] Deyan Todorov Yordanov. *From ^{27}Mg to ^{33}Mg: transition to the Island of inversion.* PhD thesis, University Leuven, 2007.

[96] D. Zajfman, O. Heber, L. Vejby-Christensen, I. Ben-Itzhak, M. Rappaport, R. Fishman, and M. Dahan. Electrostatic bottle for long-time storage of fast ion beams. *Phys. Rev. A*, 55:R1577–R1580, Mar 1997.